Master's thesis

NTNU
Norwegian University of Science and Technology
Faculty of Natural Sciences
Department of Physics

Marte Kåstad Høiskar

Dynamic contrast-enhanced MRI in head and neck cancer

A systematic comparison of different modelling approaches

Master's thesis in Physics and Mathematics
Supervisor: Kathrine Røe Redalen
Co-supervisor: René Winter
June 2022

NTNU
Norwegian University of
Science and Technology

Marte Kåstad Høiskar

Dynamic contrast-enhanced MRI in head and neck cancer

A systematic comparison of different modelling approaches

Master's thesis in Physics and Mathematics
Supervisor: Kathrine Røe Redalen
Co-supervisor: René Winter
June 2022

Norwegian University of Science and Technology
Faculty of Natural Sciences
Department of Physics

NTNU
Norwegian University of
Science and Technology

Abstract

Background Tumours are characterised by disorganised vasculature due to increased angiogenesis, i.e. formation of blood vessels. This results in regions with low oxygen, also called hypoxia, within the tumour. Tumour hypoxia is associated with a poor prognosis for head and neck cancer. Dynamic contrast-enhanced magnetic resonance imaging (DCE-MRI) is a promising quantitative imaging modality for describing the microvasculature of the tumour. Thus, DCE-MRI has the potential to become a prognostic and predictive tool for head and neck cancer treatment. DCE-MR images can be analysed both semi-quantitatively and quantitatively. Three of the most common pharmacokinetic models used in the quantitative analysis are the Tofts model, the extended Tofts model and the Brix model. The Tofts and extended Tofts model require an arterial input function (AIF). The AIF is usually obtained for each patient. It is not always possible to obtain an individual AIF and thus a population AIF, based on the AIFs of other patients, is used. The main objectives of this study were to investigate the accuracy and robustness of the population AIF and to compare the three different quantitative models. The pharmacokinetic parameters found by the models were also compared to semi-quantitative parameters.

Methods DCE-MRI was performed on 20 head and neck cancer patients. Some of the patients had malignant lymph nodes in addition to the primary tumour. Six different population AIFs were calculated. The DCE-MR images of the lymph nodes were analysed using the Tofts model together with the population AIFs and with the individual AIF for each patient. The concordance correlation coefficients (CCC) comparing the pharmacokinetic parameters obtained with the population AIFs and the corresponding parameters found with the individual AIF were calculated. The DCE-MR images were also analysed using the extended Tofts model with the individual AIF and the Brix model. Further, the semi-quantitative parameters called the areas under the curve (AUCs) were also calculated from the DCE-MR images. The analyses were performed voxel-by-voxel, meaning the pharmacokinetic parameters from the models and the AUCs were calculated for each voxel in the lymph node. Further, the median pharmacokinetic parameters and AUCs over the voxels were calculated for each lymph node. In addition, a mean ROI analysis was performed, i.e. the mean enhancement pattern over all voxels in the lymph node was used to calculate pharmacokinetic and semi-quantitative parameters which resulted in a single set of parameters for each lymph node. The Pearson correlation coefficients (CC) comparing the median and the mean ROI parameters from the quantitative and semi-quantitative analysis were calculated.

Results The population AIF was robust. However, the pharmacokinetic parameters found with the Tofts model using the population AIFs differed substantially from the corresponding parameters found using the individual AIF. Thus, the population AIFs did not result in accurate pharmacokinetic parameters. The median K^{trans} and median v_e from the Tofts model correlated with the corresponding parameters from the extended Tofts model with a CCC of 0.99 and 1.00, respectively. In addition, the median K^{trans} correlated with the median v_e from the Tofts model with a Pearson CC of 0.71 and 0.83, respectively. The Pearson CC between A and K_{ep} from the Brix model were 0.96 and 0.93 for the mean ROI and median values, respectively. The most significant correlation between parameters from different models was the correlation between K_{el} from the Brix model and K_{ep} from the extended Tofts model. They correlated with a Pearson CC of 0.77 and 0.70 when using the mean ROI and median values, respectively. In contrast, the pharmacokinetic parameters did not correlate with the AUCs which was unexpected.

Conclusion The results presented in this thesis showed that the individual AIF is preferred over the population AIFs. The Tofts and extended Tofts models gave similar K^{trans} and v_e values. Whether this occurred due to weakly vascularised tissue is not clear, but an analysis of lymph node vasculature using immunohistochemistry of resected lymph node samples would be useful and should be done in the future. The model fitting did sometimes result in invalid values which can be associated with necrosis, which also should be investigated furher. The K_{el} from the Brix model correlated with the K_{ep} from the Tofts models. The correlation analysis was based on mean ROI and median values, future work should also investigate the correlation between the parameters on a voxel-by-voxel basis. Last, the parameters' prognostic and predictive value should be investigated when the long-term patient outcome is available.

Sammendrag

Bakgrunn Kreftsvulster er karakterisert av uorganisert blodkarnettverk på grunn av økt angiogenese, som vil si formasjon av blodårer. Dette resulterer i at svulsten får områder med lavt oksygennivå, kalt hypoksi. Hypoksi i svulster er assosiert med dårlig prognose for hode- og halskreft. Dynamisk kontrastforsterket magnetisk resonans avbildning (DCE-MRI) er en lovende kvantitativ bildemodalitet for å beskrive mikrovaskulaturen til svulster. Dermed har DCE-MRI potensialet til å bli et prognostisk og prediktivt verktøy for behandling av hode- og halskreft. DCE-MR bilder kan bli analysert både semi-kvantitativt og kvantitativt. Tre av de mest vanlige farmakokinetiske modellene brukt i kvantitativ analyse er Tofts, utvidet Tofts og Brix modellene. Tofts og utvidet Tofts modellene trenger en arteriell inputfunksjon (AIF). AIF bestemmes oftes for hver pasient. Det er ikke alltid det er mulig å beregne en slik individuell AIF, og derfor blir en populasjon AIF som er basert på flere pasienters AIF brukt istedenfor. Hovedmålet med dette studiet var å undersøke presisjonen og robustheten til populasjon AIF-en og å sammenligne de tre ulike kvantitative modellene. De farmakokinetiske parameterne beregnet av modellene ble også sammenlignet med semi-kvantitative parametere.

Metode DCE-MRI ble gjennomført for 20 hode- og halskreftpasienter. Noen av pasientene hadde ondartete lymfeknuter i tillegg til primærsvulsten. Seks ulike populasjon AIF-er ble beregnet. DCE-MR bilder av lymfeknutene ble analysert med Tofts modellen sammen med populasjon AIF-ene og med individuell AIF for hver pasient. Samsvarskorrelasjonskoeffisientene, på engelsk kjent som concordance correlation coefficient (CCC), som sammenligner de farmakokinetiske parameterne beregnet med populasjon AIF-ene med de tilhørende parameterne beregnet med individuell AIF ble beregnet. DCE-MR bildene ble også analysert med den utvidete Tofts modellen ved å bruke individuell AIF og med Brix modellen. Semi-kvantitative parametere kalt arealet under kurven (AUC) ble også beregnet fra DCE-MRI bildene. Analysene ble utført voxel-for-voxel, som betyr at farmakokinetiske parametere fra modellene og AUC-ene ble beregnet for hver voxel i lymfeknutene. Medianene over alle voxelene ble beregnet for de farmakokinetiske parameterne for hver lymfeknute. I tillegg ble en gjennomsnittlig ROI analyse utført, det vil si lymfeknutens gjennomsnittlige kontrastforløpet ble brukt til å beregne de farmakokinetiske og semi-kvantitative parameterne, som resulterte i ett sett med parametere for hver lymfeknute. Pearsons korrelasjonskoeffisienter (CC) mellom medianverdien til både de ulike farmakokinetiske og semi-kvantitative parameterne ble beregnet. Korrelasjonskoeffisientene mellom de ulike parameterne ble også beregnet ved bruk av de gjennomsnittlige ROI-verdiene.

Resultater Populasjon AIF-ene var robuste, men de farmakokinetiske parameterne fra Tofts modellen brukt sammen med populasjon AIF-ene var betydelig ulike de tilhørende parameterne beregnet med individuell AIF. Derfor gav ikke populasjon AIF-ene korrekte farmakokinetiske parametere. Median K^{trans} og median v_e fra Tofts modellen korrelerte med de tilhørende parameterne fra den utvidete Tofts modellen med en CCC på henholdsvis 0.99 og 1.00. I tillegg korrelerte median K^{trans} med median v_e fra Tofts modellen med en Pearson CC på henholdsvis 0.71 og 0.83. Pearson CC-en mellom A og K_{ep} fra Brix modellen var 0.96 og 0.93 for henholdsvis gjennomsnittlig ROI verdier og medianverdier. Den sterkest korrelasjonen mellom parameterne fra ulike modeller ble funnet mellom k_{el} fra Brix modellen og K_{ep} fra den utvidete Tofts modellen. De korrelerte med en Pearson CC på 0.77 og 0.70 for henholdsvis gjennomsnittlige ROI verdier og medianverdier. De farmakokinetiske parameterne korrelerte derimot ikke med AUC-ene, noe som var uventet.

Konklusjon Resultatene i denne oppgaven viste at individuell AIF burde brukes fremfor populasjon AIF. Tofts og utvidet Tofts modellene ga lignende K^{trans}-og v_e-verdier. Det er uklart om dette skjedde fordi vevet var svakt vaskularisert, men immunhistokjemi av resekterte lymeknuter hadde vært nyttig for å analysere vaskulaturen i lymfeknutene og bør utføres i senere studier. Noen ganger resulterte modelltilpasningen i ugyldige verdier, som kan være på grunn av nekrose. Dette burde undersøkes grundigere senere. K_{el} fra Brix modellen korrelerte med K_{ep} fra Tofts modellene. Korrelasjonsanalysen var basert på gjennomsnittlig ROI verdier og medianverdier. Fremtidige studier burde også undersøke korrelasjonen mellom parameterne voxel-for-voxel. Til slutt burde parameternes prognostiske og prediktive verdi undersøkes når langtids oppfølgingsdata av pasientene er tilgjengelige.

Preface

This thesis is part of my MSc degree in Biophysics and Medical Technology at the Norwegian University of Science and Technology (NTNU). The project was carried out at NTNU in the spring of 2022.

First of all, special thanks go to my supervisor Kathrine for allowing me to work on this exciting project. Thanks for sharing your knowledge and guiding me throughout the project. Your feedback, help with writing and finding ideas for further work have been invaluable. I would also like to thank my co-supervisor René for helping me out and providing valuable insights into the discussions of the project. Further, I would like to thank Sigrun for all the help obtaining patient data from St. Olavs Hospital. I am looking forward to continuing working with you all in the future.

At last but not least, I would like to thank my family and friends for all your help and support throughout my studies.

Contents

Abbreviations

DCE-MRI - Dynamic contrast-enhanced magnetic resonance imaging

AIF - Arterial input function

CCC - Concordance correlation coefficient

AUC - Area under the curve

CC - Correlation coefficient

NTNU - Norwegian University of Science and Technology

CA - Contrast agent

HPV - Human papillomavirus

RF - Radiofrequency

FID - Free induction decay

TE - Echo time

TR - Repetition time

Gd - Gadolinium

EES - Extracellular extravascular space

VFA - Variable flip angle

ROI - Region of interest

TCC - Time-concentration curve

TIC - Time-intensity curve

CI - Contrast index

2CXM - Two-compartment exchange model

1 Introduction

Worldwide, approximately 900 000 patients are diagnosed with head and neck cancer annually and for 400 000 of them, the disease results in death [1]. Despite the advances in cancer treatment techniques, the 5-year survival has stayed around 60 % for some time [2]. Lately, many researchers have focused on individualising the treatment using quantitative imaging to improve patient outcomes.

Dynamic contrast-enhanced magnetic resonance imaging (DCE-MRI) is a promising quantitative imaging modality for assessing the microvasculature, i.e. the perfusion and permeability of blood vessels, within tissues. The use of DCE-MRI to study perfusion was first introduced in the 1990s [3]. One of the hallmarks of cancer is angiogenesis, i.e. formation of blood vessels, because the increased cell proliferation demands a high level of oxygen supply through the blood vessels [4]. However, the increased blood vessel formation causes the microvasculature within tumour tissue to become disorganised, resulting in hypoxic regions, i.e. regions with low oxygen concentration. Tumour hypoxia is associated with a poor prognosis for head and neck cancer patients. Thus, obtaining information about the microvasculature and detecting hypoxia using DCE-MRI can potentially improve cancer treatment by increasing the radiation dose to hypoxic regions within the tumour [5].

In DCE-MRI, a contrast agent (CA) is injected intravenously into the patient and the MRI signal is enhanced in its presence. The signal in the tissue of interest is measured over time before, during and after the injection of the CA, resulting in a signal enhancement curve. Pharmacokinetic parameters that describe the microvasculature of the tissue can be obtained by fitting suitable models to the signal enhancement curve. The three most common models are the Tofts model, the extended Tofts model and the Brix model which were proposed in the 1990s [6, 7].

The Tofts and extended Tofts models require an arterial input function (AIF) which is the signal enhancement curve of a region within an artery. DCE-MR images often contain distortions caused by unsaturated blood flow in the artery and in some cases the field of view does not even contain an artery [8]. Thus, it is not always possible to obtain a reliable AIF for the patient. As an alternative to the individual AIF, Parker et al proposed to use a population AIF which is the average of the AIFs of several patients [9]. However, the AIF of individual patients differ due to the interpatient variability in factors such as kidney function and heart rate and this is not accounted for in the population AIF. The population AIF will not be the true AIF for individual patients. Thus, the pharmacokinetic parameters that are calculated with the population AIF will to some extent deviate from the true values produced with the individual AIF. It is therefore important to study the replicability of the pharmacokinetic parameters to ensure that the use of the population AIF is valid if needed.

Most studies apply only one model to obtain pharmacokinetic parameters. The model may vary and thus makes it more difficult to compare the results from different studies [10]. Therefore, it would be of interest to better understand the relationship between the pharmacokinetic parameters obtained by different models. Although there are studies that compare the Tofts model and the Brix model for cervical carcinoma and rectal cancer, there are to my knowledge no such studies for head and neck cancer [11, 12]. A better understanding of the correlation between the parameters would also facilitate the interpretation of multicenter clinical trials that apply different pharmacokinetic models.

One of the main objectives of this study was to compare the pharmacokinetic parameters

that were produced when applying the individual AIF to the corresponding parameters obtained using the population AIF to investigate the reliability of the population AIF. Variations of the population AIF were implemented and the resulting parameters were analysed, facilitating the examination of the robustness of the population AIF. In addition, three different pharmacokinetic models were applied to head and neck cancer patients and the correlations between the resulting pharmacokinetic parameters were studied.

In this report, the main concepts of MRI and DCE-MRI will be explained, as well as the three pharmacokinetic models that have been used in this study. The methodology will be described followed by a presentation and discussion of the results. At last, some conclusions will be drawn.

2 Cancer

Cancer is a group of diseases that are characterised by abnormal cell growth. Any of the different cell types in the body can undergo abnormal proliferation, and thus there are a hundred distinct types of cancer with different biological behaviour and response to treatment [13]. Cancer can be classified as benign or malignant tumours. Benign tumours do not invade surrounding tissue and spread to distant parts of the body, and thus are confined to their original localization. They can usually be removed surgically and therefore are less of a threat. Malignant tumours, on the other hand, invade surrounding tissue and spread via the circulatory or lymphatic system to other body parts [13]. Therefore, malignant tumours can resist localized treatment which makes them dangerous.

2.1 Head and neck cancer

Cancer can also be classified based on the tissue of origin, e.g. lung cancer, head and neck cancer and breast cancer. Head and neck cancer was the seventh most common cancer in the world in 2018 [14]. It includes cancer in the oral cavity, the pharynx, the larynx and the nasal cavity [15]. Head and neck tumours tend to metastasise to lymph nodes in the neck. The presence and number of metastasis is an important prognostic factor that influences the choice of treatment. The treatment choice is also dependent on the anatomical location of the tumour and the specifics of the patient [15]. Another important prognostic factor is the human papillomavirus (HPV) infection. Head and neck cancer patients that have an HPV infection have a higher survival rate than patients with HPV-negative cancer. A study, done by Ang *et. al.*, showed that the 3-year overall survival rate for patients with HPV-positive advanced oropharyngeal cancer was 82.4% vs 57.1% for patients with HPV-negative cancer [16]. The same trend was found by Fakhry *et. al.* who found that the 2-year overall survival rate was 94% and 58% for patients with HPV-positive and HPV-negative cancer, respectively [17].

2.2 Tumour vascularisation

The uncontrolled cell growth that results in cancer occurs because the physiology and thus the microenvironment of the cells is altered. One of the hallmarks of cancer cells is sustained angiogenesis [4]. All cells require oxygen and nutrition to grow, which diffuse into the cells from the vascular system. The vasculature of healthy tissue is orderly structured,

as seen in Figure 1, and regulated by the balance of pro-and anti-angiogenic molecular factors to ensure even distribution of blood supply to all cells [18]. If a tumour grows beyond 100 μm in diameter, then some of the cells will be too far away for the oxygen to reach the cells through diffusion [19]. Thus, hypoxic regions, i.e. regions with low oxygen concentration are produced in the tumour. In addition, if the oxygen and nutrition supply is insufficient to support further cell growth, the tumour over-expresses proangiogenic factors to induce angiogenesis, i.e. formation of new blood vessels from pre-existing vessels [18]. As seen in Figure 1, the resulting tumour vasculature is not hierarchically organized and the density of the vessels varies greatly compared to normal vasculature. The vessels differ in diameter and the larger vessels can prevent the blood from flowing through the smaller vessels, resulting in hypoxic regions. Hypoxia refers to the insufficient oxygen supply to the cells which can result in resistance to radiotherapy [20].

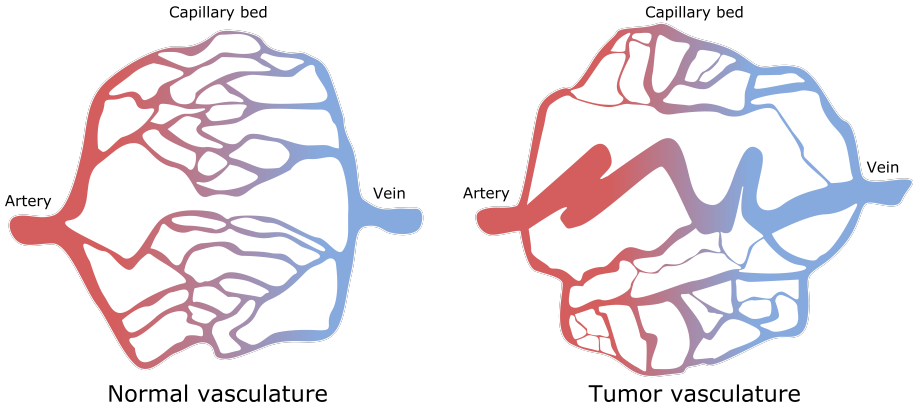

Figure 1: The vascular network of normal and cancerous tissue.

The fragile blood vessels in tumour vasculature are highly permeable compared to normal vasculature [21]. However, the permeability varies amongst tumour types, as well as between tumours of the same type. The increased perfusion in tumours can potentially be detected by DCE-MRI, which detects the exchange of CA between vasculature and tissue. The knowledge of the vasculature of tumours by DCE-MRI can help to predict and evaluate the patient's response to treatments. It can also be a useful tool to stratify patients for individualised treatment.

3 Magnetic resonance imaging

MRI is an imaging technique used to obtain anatomical and functional information about the human body. This chapter will explain the basic principles of MRI and is based on *MRI in practice* by Westbrook C. and Talbot J. [22] unless anything else is specified.

3.1 Fundamental principles in spin-physics

In MRI, the signal is the observations of nuclear spins, most commonly ^{1}H (protons). Nuclear spin is an intrinsic quantum mechanical property of nuclei. It is often thought of as a rotational motion about an axis that produces spin angular moment, though, in reality, it is not a physical rotation. Spin also causes spin magnetic moment, similar to classical magnetic moment caused by the orbital motion of charged particles. The relation

between spin $\vec{I}$ and spin magnetic moment $\vec{\mu}$ is:

$$\vec{\mu} = g\frac{e}{2m_p}\vec{I} = \gamma\vec{I} \tag{1}$$

where $\gamma \equiv gq/2m$ is the gyromagnetic ratio, g is called the g-factor, q is the charge and m is the mass of the particle. The magnetic moment and spin vector are always aligned and differ only by a constant. Therefore, the terms are equivalent and interchangeable, and in MRI we measure the magnetic moment but often talk about spin.

Nuclear spins are quantized properties that take on specific values when they are measured:

$$I_{x,y,z} = m\hbar, \quad m = -I, -I+1, ..., 0, ..., I-1, I \tag{2}$$

Protons have a spin value |m| of 1/2 and are therefore in a superposition of the two possible spin eigenstates: spin-up (m=+1/2) and spin-down (m=-1/2). However, when the spin is measured the wave function collapses and the proton is either in spin-down or spin-up eigenstate. The two eigenstates have initially the same energy, resulting in an equal distribution of spins in the two eigenstates. The energy level of the eigenstates can however be separated if an external magnetic field $\vec{B_0}$ is applied due to Zeeman interaction, as illustrated in Figure 2.

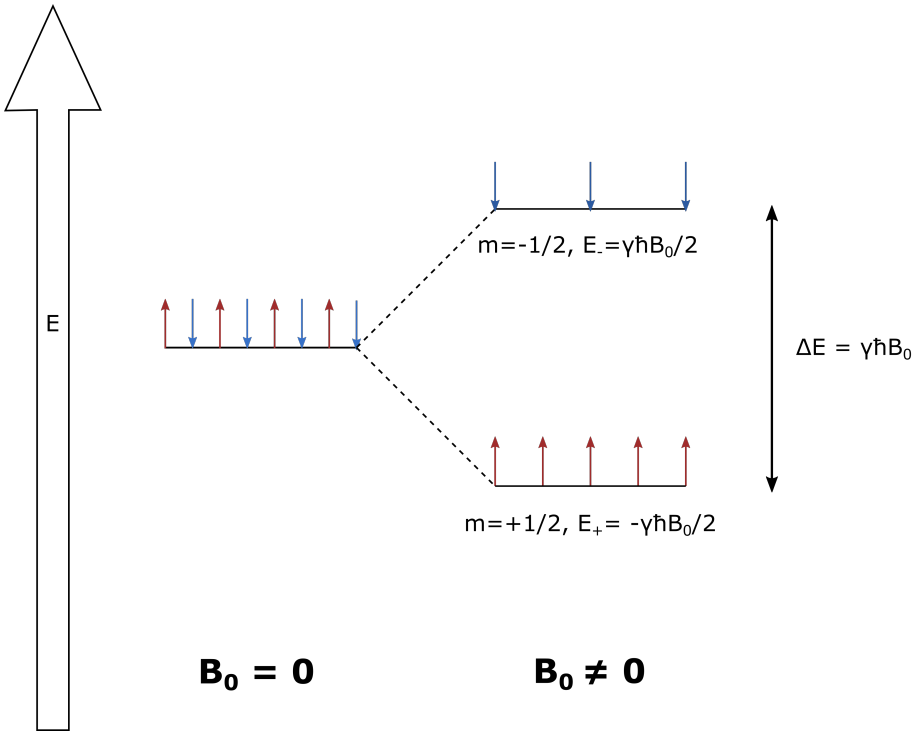

Figure 2: This figure illustrates the Zeeman splitting. The spins in both eigenstates have the same energy when the magnetic field, B_0 is zero. When a magnetic field is applied, the spins with the spin value m=+1/2 (spin-up) and the spins with a spin value m=-1/2 (spin-down) are divided into two different energy states: $E_+ = -\hbar\gamma B_0/2$ and $E_- = \hbar\gamma B_0/2$, respectively. This results in an energy difference $\Delta E = \gamma\hbar B_0$ where γ is the gyromagnetic ratio, $\hbar$ is the reduced Planck constant.

The energy of the spins in an applied magnetic field is:

$$E = -\vec{\mu} \cdot \vec{B_0} = -m\hbar\gamma B_0 \tag{3}$$

where $\hbar$ is the reduced Planck constant. The nuclear magnetic moment mimics the behaviour of a bar magnet: aligning itself with the magnetic field. The protons in the spin-up (+) state will align their magnetic moment with B_0, resulting in E_+=-$\hbar\gamma B_0/2$. On the other hand, the energy of protons in the spin-down (-) state will be $E_- = \hbar\gamma B_0/2$, corresponding to the magnetic moment aligning antiparallel to B_0. Thus, the energy difference between the two states is $\hbar\gamma B_0 = \hbar\omega_0$ where ω_0 is called the Larmor frequency or the precession frequency.

The number of nuclei in the spin-up state, n_+ and spin-down state n_- is determined by the Boltzmann distribution:

$$\frac{n_+}{n_-} = e^{-\Delta E/k_B T} \tag{4}$$

where ΔE is the energy difference between the two states, k_B is the Boltzmann constant and T is the temperature. Because there is a slight preference for lower energy states, i.e. spin-up states as shown in Figure 2, an ensemble of protons produces a net magnetisation vector $\vec{M}$ that is aligned with the applied field. The strength of the MR signal depends on the amplitude of the magnetization vector which increases with the energy difference and the density of spins. Thus, a strong magnetic field and a high gyromagnetic ratio will produce a strong MR signal. Protons have a high gyromagnetic ratio compared to other elements which is one of the reasons why it is common to observe the spins of protons in MRI. The other reason is that the human body consists of a lot of water, resulting in an abundance of protons that produce a large magnetization vector, i.e. large MR signal.

The magnetic moment of the protons does not align completely with the magnetic field but precess around B_0 with a speed determined by the precession frequency ω_0, as illustrated in Figure 3a. The rotational motion of the nuclei follows the precession path. As the protons align with B_0, they will not begin at the same place on the precession path. Thus, the protons are out of phase with each other, i.e they are incoherent, and the magnetization vector is completely aligned with B_0, as shown in Figure 3b.

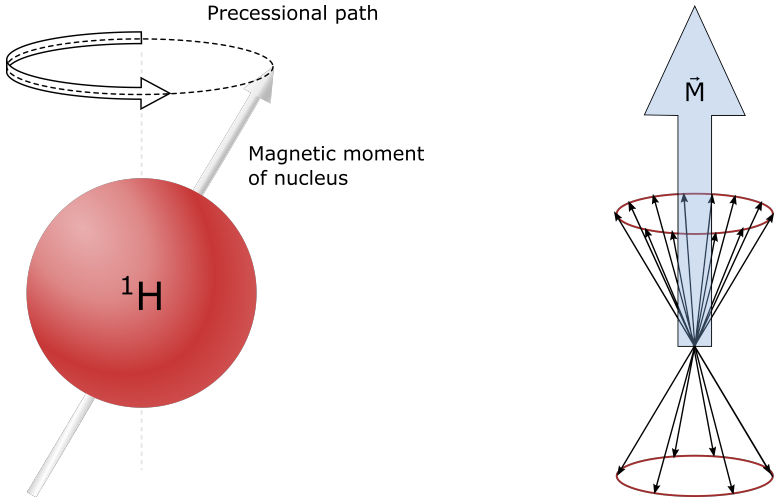

(a) (b)

Figure 3: a) Precession of the magnetic moment of hydrogen nuclei. b) Precession of an ensamble of spins, resulting in a net magnetization $\vec{M}$ aligned with B_0.

3.2 Signal generation and detection

Initially, the magnetic moments of the hydrogen nuclei are randomly oriented and no magnetic effect is produced. By applying an external magnetic field B_0 along the z-axis, the majority of the spins will align themself parallel and precess around B_0, producing a net magnetization vector $\vec{M}$ parallel to B_0. However, $\vec{M}$ is measured by a pair of receiver coils that lie in the XY plane, and thus the direction of $\vec{M}$ must be altered to obtain a signal.

The receiver coils, as shown in Figure 4, measure the magnetization as it precesses in the transverse plane. Faraday's law of induction states that a change of magnetic flux through a closed circuit induces an electromotive force, also called voltage, in the circuit. The rotating magnetization produces a time-varying magnetic field which induces a voltage, i.e. signal, in the coils that can be measured. The signal will have a sinusoidal shape with amplitude and frequency. Due to the receiver coils being in the XY-plane, the amplitude and frequency of the signal depend on the amplitude and frequency of the magnetization vector in the transversal plane, noted $M_\perp$.

As mentioned, $\vec{M}$ is aligned with B_0 at equilibrium, resulting in no transversal magnetization and no signal. To generate a signal, the magnetization must be tipped away from its equilibrium position along the z-axis by transmitting a radio frequency (RF) pulse called an RF excitation pulse, as illustrated in Figure 4b. An RF pulse is electromagnetic radiation with frequency in the radiofrequency band of the electromagnetic spectrum. The excitation pulse produces an oscillating magnetic field called B_1. The B_1 field has a range of frequencies centred around the Larmor frequency of the precessing magnetization vector and is applied at 90° to B_0.

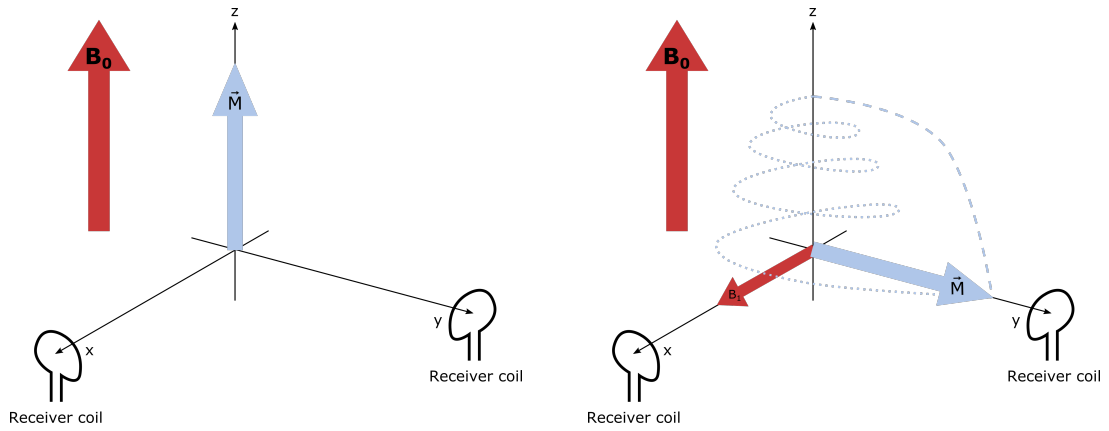

(a) Equilibrium (b) RF-pulse

Figure 4: a) The magnetic resonance system at equilibrium before b) a radiofrequency (RF) pulse B_1 turn the magnetization vector $\vec{M}$ down into the transverse plane.

From a quantum mechanical perspective, the protons absorb energy from the RF excitation pulse. Because the RF pulse has the same frequency as the Larmor frequency, it delivers quantized energy packets of $\hbar\omega_0$ that correspond to the energy difference between the spin-up and spin-down state. Therefore, protons in the low-energy spin-up state are excited to the spin-down state, while protons in the spin-down state are stimulated to deexcite to the spin-up state. This phenomenon is called resonance. There are more low-energy spins, thus the net effect is energy absorption. The longitudinal magnetization $M_\parallel$, i.e. magnetization along the B_0 field, will grow shorter and even become negative if the RF

pulse last for a long time.

From a classical view, the B_1 field produces a torque that is applied to the magnetization vector in synchrony with the precession of $\vec{M}$, keeping the reorientation of the torque at the same frequency as the Larmor frequency. This concept is similar to how torque is applied to a spinning wheel to change its orientation. The applied B_1 field results in the magnetization spiralling downward toward the transversal plane, as illustrated in Figure 4. The RF excitation pulse also moves all the magnetic moments to the same position on the precession path. Thus, the magnetic moments are in phase and the magnetization vector will precess around the z-axis after the RF pulse has been applied. The precessional transverse magnetization can then be measured by the receiver coils, resulting in an MR signal.

To simplify the visualisation of the motion of $\vec{M}$, the rotating frame of reference is often used instead of the stationary frame. In the rotating frame, the observer rotates about the z-axis. If the frequency of the rotating frame is the same as the Larmor frequency, then the magnetization vector that is precessing around B_0 will appear to be standing still. However, magnetization with faster or slower precession frequency will appear to be rotating clockwise or anticlockwise respectively. Onward, the magnetization vector will be discussed in the rotating frame of reference, unless anything else is specified. The spiralling motion of $\vec{M}$ due to the B_1 field, will be seen as a rotation about B_1 as it moves down toward the transversal plane, as illustrated in Figure 4b. After the RF excitation pulse, the magnetization vector will be at an angle to the z-axis. The angle is called the flip angle and depends on the duration of the RF pulse. It is common for the excitation pulse to be a 90° pulse, resulting in $\vec{M}$ lying in the transversal plane which produces the highest MR signal.

3.3 Relaxation of $\vec{M}$

The RF excitation pulse causes the magnetization vector to tip away from its equilibrium position along B_0. Assume the excitation pulse is a 90° pulse and $\vec{M}$ lies in the transversal plane with no longitudinal component. When the B_1 field is removed, two relaxation mechanisms occur simultaneously: longitudinal and transversal relaxation.

3.3.1 Longitudinal relaxation

The RF excitation pulse excites low-energy spins in the spin-up state to the spin-down state. These spins release energy to their surroundings and go back to the low-energy state when the B_1 field is removed to reach thermal equilibrium. This mechanism is called longitudinal relaxation, spin-lattice relaxation or T_1 relaxation. As the spins return to their thermal equilibrium state, the longitudinal magnetization is recovered and can be expressed by:

$$M_{\parallel}(t) = M_0 \left(1 - e^{-t/T_1}\right) \tag{5}$$

where M_0 is the magnetization at equilibrium and T_1 is the T_1 recovery time, i.e. the time it takes for $M_{\parallel}$ to increase by a factor of e. The general shape of the T_1 recovery curve can be seen in Figure 5.

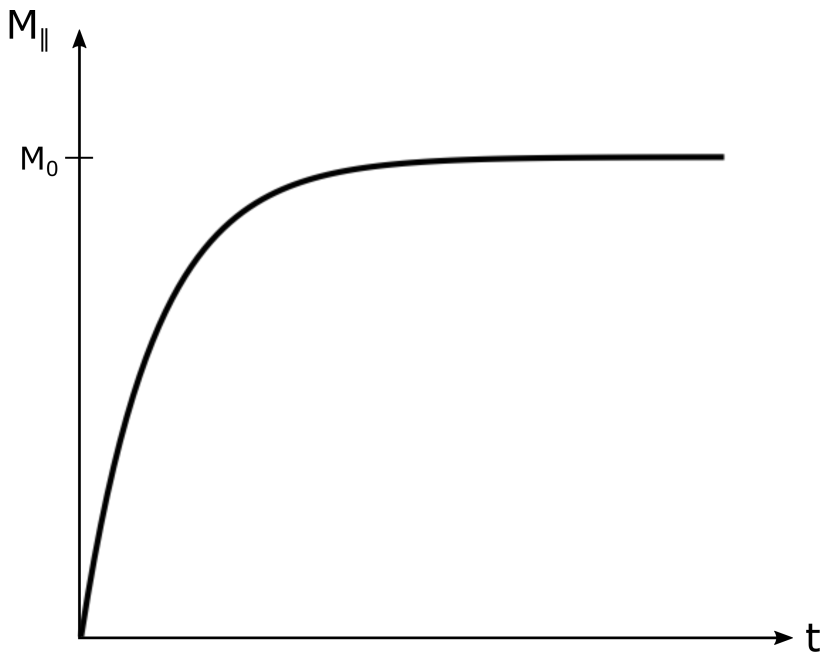

Figure 5: The longitudinal magnetization $M_{\parallel}$ as a function of time after a 90° radiofrequency pulse was applied. After some time $M_{\parallel}$ reaches the equilibrium state M_0.

3.3.2 Transverse relaxation

Simultaneously to the recovery of the longitudinal magnetization, the transversal magnetization decays towards zero after the B_1 field is removed:

$$M_{\perp}(t) = M_{\perp}(0)e^{-t/T_2^*} \tag{6}$$

Here, $M_{\perp}(0)$ is the transverse magnetization right after the RF excitation pulse was applied and T_2^* is the time it takes for the transverse magnetization to be reduced by a factor of e. The magnetic field in the tissue is heterogenic and thus the protons will experience slightly different magnetic fields and precess at frequencies different from the Larmor frequency. In the rotating frame with a frequency equal to the Larmor frequency, the magnetization vector will appear to "fan out" in the transverse plane, as illustrated in Figure 6. The vector sum of the transverse magnetization will therefore decrease to zero as the magnetization dephases, resulting in loss of MR signal as seen in Figure 6.

The mechanisms that cause the spins to experience different magnetic fields can be divided into two categories: those that are fixed in time and those that vary with time. Inhomogeneities of the magnetic field that are fixed in time can be due to the imperfections in the design of the magnets that produce the B_0 field, among other factors. Even if the magnets produce a perfect uniform field, the insertion of a body in the MR scanner will induce inhomogeneities in the magnetic field. Tissue can be both paramagnetic and diamagnetic, causing the magnetic field to increase or reduce respectively. These small variations in the magnetic field are static in space and will cause dephasing at a constant rate. The decay of the transverse magnetization due to static inhomogeneities is characterized by the relaxation time $T_2^{'}$ and decay in a similar manner as the curve in Figure 6, except the decay constant is $T_2^{'}$.

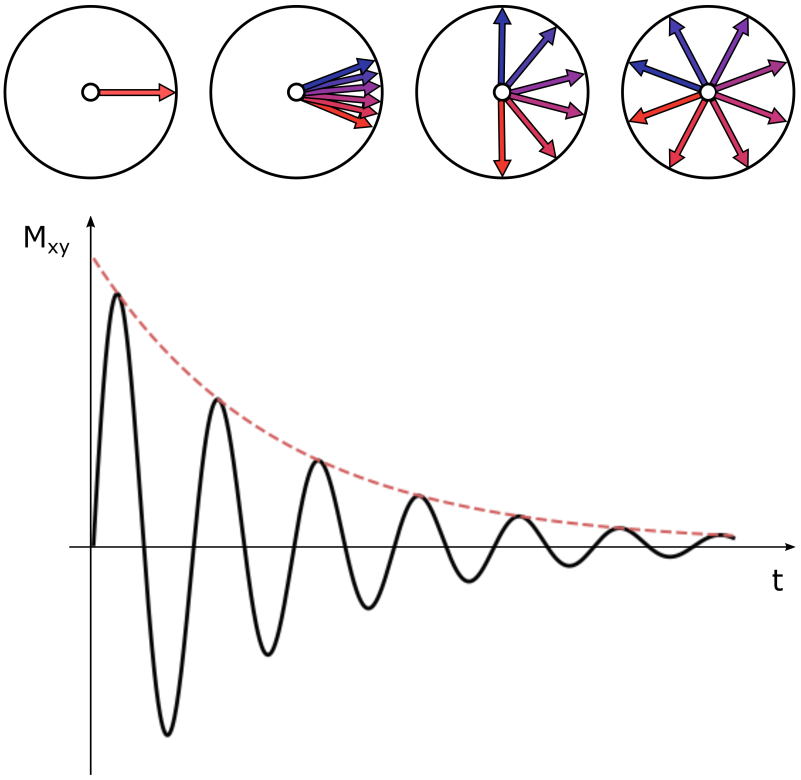

Figure 6: Illustration of the dephasing of the transversal magnetization M_{xy} due to the inhomogeneities in the magnetic field. The resulting MR signal is called the free induction decay (FID) and the exponential decay is determined by the T_2^*.

The inhomogeneities of the magnetic field can also vary slowly with time because neighbouring protons interact with each other. Protons themselves are magnetic and increase or decrease the magnetic field surrounding neighbouring protons. Due to the rotation and translation of protons in tissue, the change in the magnetic field because of the magnetic properties of protons will vary with time. The time-varying magnetic field results in dephasing of the magnetization and decay of signal determined by the relaxation time T_2. The total decay of the signal is determined by the relaxation time T_2^* in Equation (6). The relation between the relaxation times is:

$$\frac{1}{T_2^*} = \frac{1}{T_2'} + \frac{1}{T_2} \tag{7}$$

Relaxation times are important parameters that influence the contrast in MR images and can be used to detect various pathologies.

3.4 Imaging sequences

After the B_0 field is removed, the dephasing of the transversal magnetization causes the signal to decay with a decay rate determined by T_2^*. The resulting signal is called the free induction decay (FID) and is illustrated in Figure 6. The FID decays within 10 ms, which is too fast for image formation as will be explained later. However, there are pulse sequences that rephase the magnetization at a later point in time, making image formation possible. The rephasing of the transverse magnetization produces a signal called

an echo. There exist two methods that create an echo by rephasing the magnetic moments of hydrogen nuclei: spin-echo and gradient-echo pulse sequence.

3.4.1 Spin-echo pulse sequence

All spin-echo pulse sequences contain RF rephasing which produces a spin-echo signal. Commonly, spin-echo pulse sequences use a 90° excitation pulse to flip the magnetization into the transverse plane. After the RF pulse is turned off, T_2^* dephasing of the magnetization occurs creating an FID signal. Another RF pulse is used after a time τ to rephase the magnetic moment of the protons. The second RF pulse is a 180° pulse and is called the RF rephasing or refocusing pulse. The principle behind the RF refocusing pulse is illustrated in Figure 7. The T_2^* dephasing causes the magnetic moments of protons to "fan out" in the transverse plane. The protons that experienced a weaker magnetic field had their precessional motion slowed down. These protons are blue in Figure 7 and constitute the trailing edge of the fan. Other protons precess faster because they experience a stronger magnetic field, and form the leading edge of the fan depicted in red in Figure 7. The 180° RF rephasing pulse is applied which flips the magnetization vector 180°. Now, the magnetic moments that formed the leading edge form the trailing edge, while those that formed the trailing edge form the leading edge of the fan, as shown in Figure 7. Because the direction of the precession remains the same, the trailing edge catches up to the leading edge. At a specific time called echo time (TE), the magnetic moments of the protons are in phase momentarily which produces a maximum signal called spin-echo as illustrated in Figure 7. Several sequences are needed to form an image and the time between each sequence is called the repetition time (TR).

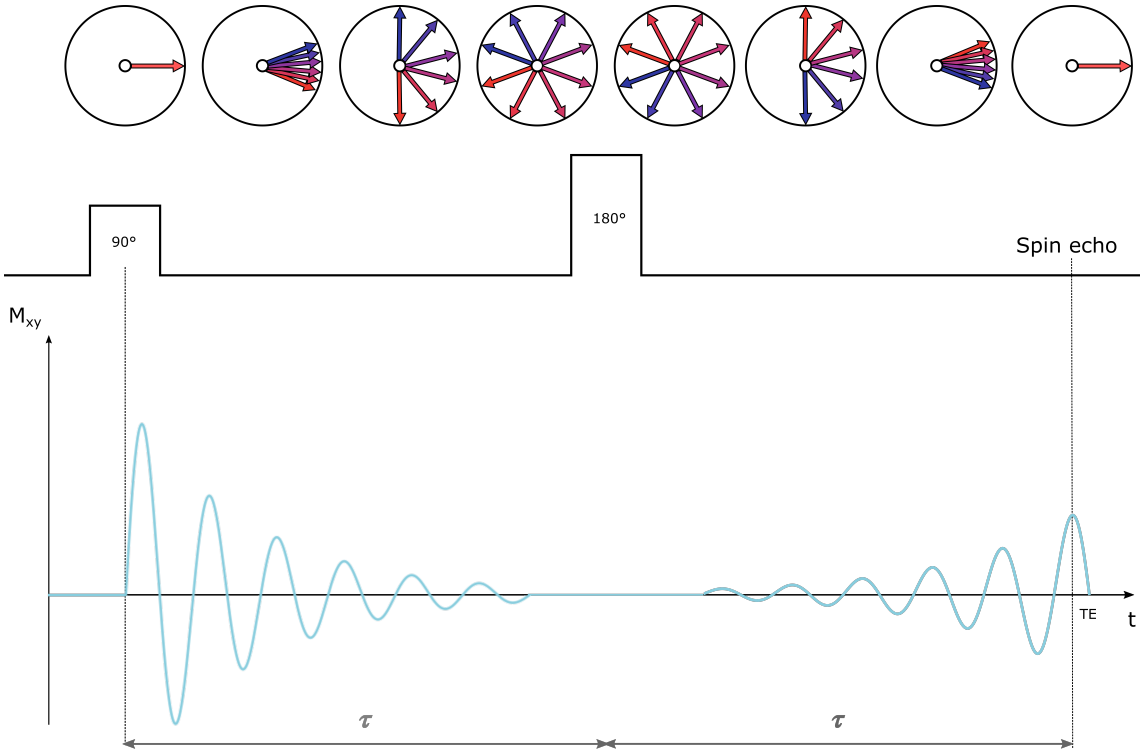

Figure 7: Illustration of the dephasing and rephasing of the magnetic moments throughout a spin echo pulse sequence, together with the resulting magnetic resonance signal.

Spin-echo pulse sequences only eliminate the T_2' dephasing which is caused by inhomogeneities in the magnetic field that are fixed in time. The RF rephasing pulse does not affect the T_2 decay because it is due to interactions between spins which vary with time. Therefore, the spin-echo peak is modulated by the T_2 decay, resulting in a lower amplitude than the FID, as seen in Figure 7.

3.4.2 Gradient-echo pulse sequence

In addition to the spin-echo pulse sequences, an echo can also be produced by gradient-echo pulse sequences using gradients to rephase the magnetic moments of the spins instead of the RF rephasing pulses. Gradients are magnetic fields that increase or decrease, often linearly, along an axis and are largely used for spatial encoding of MR signal which will be explained in more detail in Section 3.5. Here, it will be explained how gradients are used to create an echo.

Without a gradient present, the protons will experience the same external applied magnetic field B_0 and thus precess with the same frequency (in reality this is not true because of the inhomogeneities in the magnetic field, but these changes are small in comparison to those produced by gradients). Once the gradients are applied, some protons will experience a stronger magnetic field while others experience a lower field strength, which will speed up or slow down their precession respectively, creating a "fan". In Figure 8, the gradient increases from left (blue) to right (red) with zero gradient at the centre. Therefore, the magnetic moments of the protons in the blue regions are slowed down and constitute the trailing edge of the fan. At the same time, the protons in the red region speed up and form the leading edge of the fan, as shown in Figure 8. This results in dephasing of the magnetization vector and loss in signal.

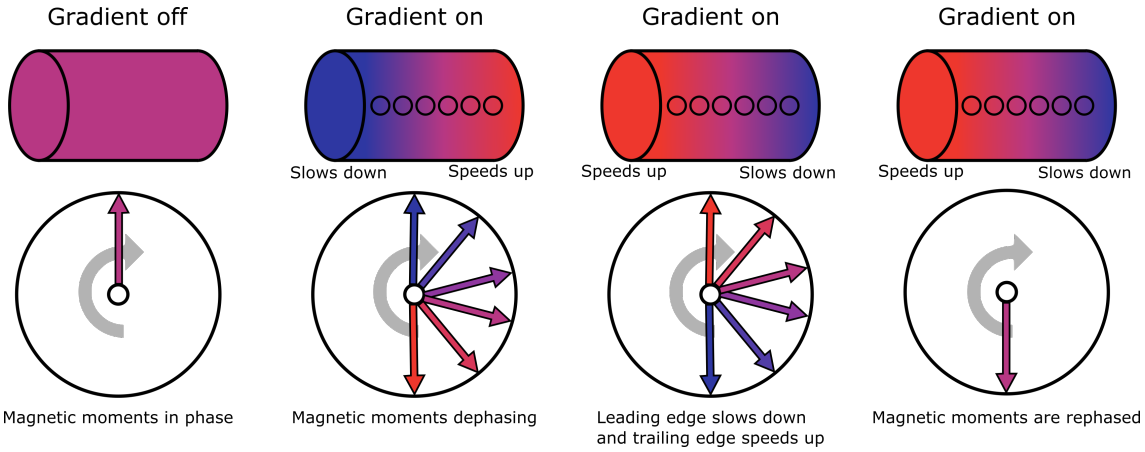

Figure 8: Illustration of rephasing the magnetic moments of protons using gradients. The magnetic moments are in phase when the gradient is off. Once the gradient is turned on, the magnetic moments dephase. As a gradient with opposite polarity is applied afterwards, the leading and trailing edge slows down and speeds up, respectively. Thus, the magnetic moments end up in phase again.

The incoherent magnetization can be rephased if another gradient is applied. The second gradient is often of the same magnitude as the first gradient, though with the opposite polarity. Instead of increasing the magnetic field from left to right, the second gradient increases the field from right to left as illustrated in Figure 8. Now, the precession of the protons in the trailing and the leading edge of the fan is sped up and slowed down,

respectively. Thus, the trailing edge catches up with the leading edge of the fan and the magnetization vector is rephased. Figure 9 shows that the rephasing of $M_\perp$ happens at time TE where the area under the rephasing gradient curve is equal to the area under the dephasing gradient. A maximum signal is induced in the receiver coils at time TE and is called a gradient-echo, as illustrated in Figure 9. Gradient-echo pulse sequences do not compensate for magnetic field inhomogeneities. Therefore, the amplitude of the gradient echo is modulated by the T_2^* decay envelope, contrary to the spin-echo which is modulated by the T_2 decay envelope.

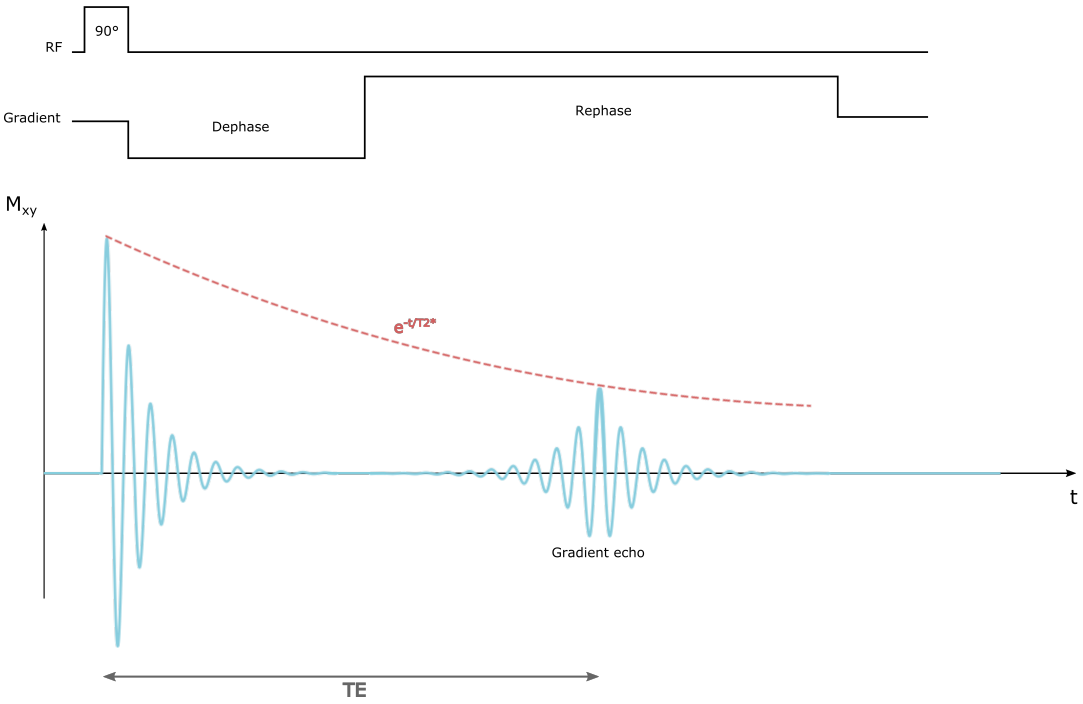

Figure 9: Schematic illustration of the gradient echo pulse sequence and the resulting magnetic resonance signal.

3.4.3 T_1- and T_2-weighted images

All medical images, including MR images, must contain contrast to differentiate between anatomical features and a range of pathologies. One of the main advantages of MRI is its excellent soft tissue discrimination. There are many variables, both intrinsic and extrinsic, that influence the contrast in the MR images. T_1 and T_2 relaxation times are two important intrinsic properties of tissues that contribute to contrast. Through proper choices of MR pulse sequence parameters, such as TR and TE, the images can become T_1- or T_2-weighted.

Different tissues exhibit different T_1 properties, resulting in different decay curves as shown in Figure 10a. At time TR, the longitudinal magnetization of some tissues will have recovered less than others. Thus, when the longitudinal magnetization is flipped into the transverse plane again, the signal will be lower for some tissues which results in contrast. The same principle applies to the T_2 properties of tissues. Figure 10b depicts T_2 decay

curves for two different tissues. The reduction of the transverse magnetization at TE when the signal is measured depends on the T_2 property of the tissue. Tissues with a high T_2 will decay slower and thus produce a larger signal compared to tissues with a low T_2. This contributes to the contrast in MR images.

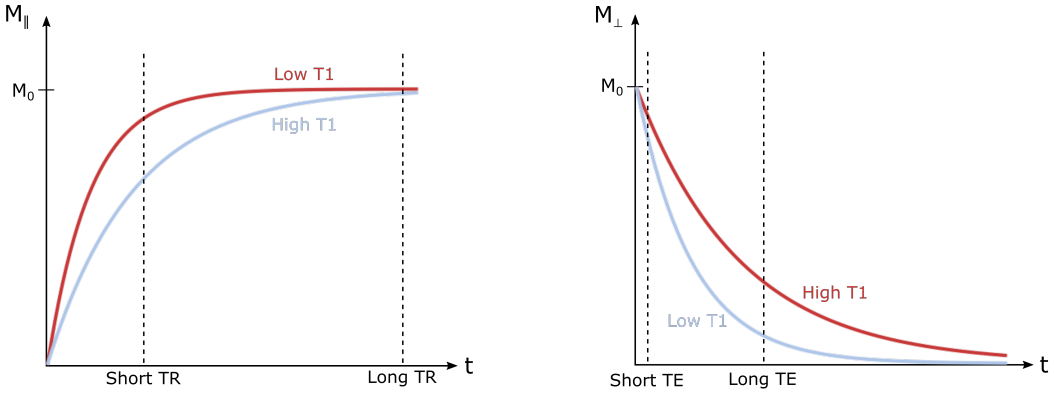

(a) (b)

Figure 10: a) The recovery of the longitudinal magnetization, $M_{\parallel}$, and the b) decay of the transverse magnetization, $M_{\perp}$, for two different tissues with different relaxation times T_1 and T_2. Here, M_0 is the magnetization at equilibrium. There will be a larger difference between the longitudinal magnetization of the two tissues at short repetition time (TR) than at long TR. The largest difference between the transversal magnetization of the two tissues occur at long echo time (TE).

It is also possible to change the contrast in MR images using different TR and TE values. The TR determines how the longitudinal magnetization recovers before the next RF excitation pulse flips it into the transverse plane again. At the same time, the TE controls the amount of decay of the transverse magnetization that occurs before the signal is measured. If the TR is too long, then the longitudinal magnetization of most of the tissues will have recovered fully and reached equilibrium, as illustrated in Figure 10a. Thus, contrast due to the T_1 properties of tissues will not be demonstrated in the image. However, if the TR is short then the $M_{\parallel}$ of most tissues will not have reached equilibrium and the amount of recovery will depend on the tissue, resulting in T_1 contrast being present in the image.

The contrast will also depend on the TE parameter. If TE is short then the transverse magnetization has had too little time to decay and the difference between the tissues' $M_{\perp}$ will be small and not present in the MR image. On the other hand, a long TE will let the transverse magnetization in different tissues decay to different degrees, resulting in T_2 contrast in the image. To obtain a T_2-weighted image, where the contrast due to the difference in T_2 between tissues dominates, both the TR and TE must be long. An image where the contrast predominantly depends on the difference in the T_1 properties of the tissues, i.e. a T_1-weighted image, can be achieved by choosing a short TR and TE. It is also possible to obtain an image without T_1- and T_2-weighting called a proton-weighted image. A proton-weighted image is achieved with a sequence with a long TR and short TE. The long TR and short TE ensure full recovery and limited decay of $M_{\parallel}$ and $M_{\perp}$ respectively, producing the largest possible signal. Because the amplitude of the magnetization vector depends on the number of protons, the difference in signal strength between tissues will be determined by their difference in proton density. Thus, images obtained from sequences with long TR and short TE are called proton-weighted images. A summary of the effect of the TR and TE parameters on the image contrast is illustrated in Figure 11.

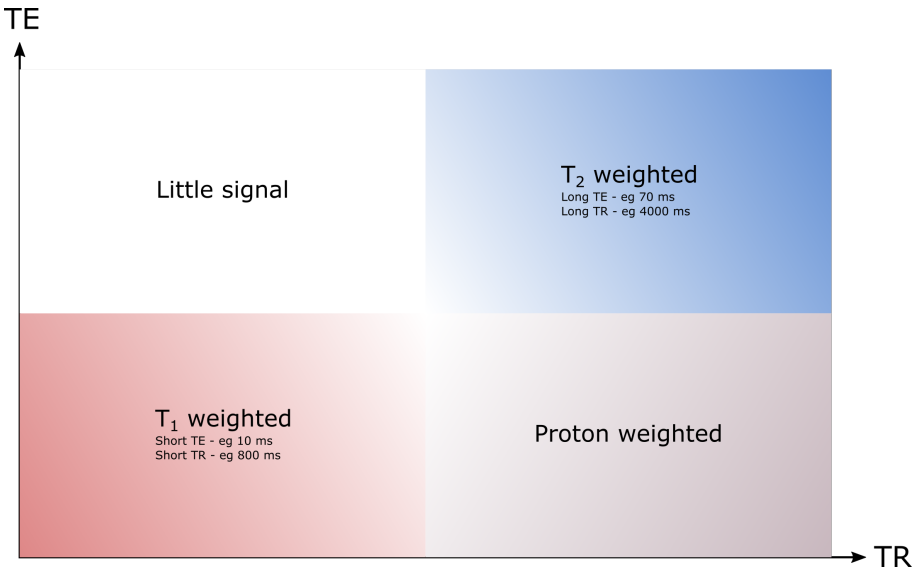

Figure 11: The effects of the repetition time (TR) and echo time (TE) choices on the image contrast is illustrated.

3.5 Image formation

The RF excitation pulse causes the nuclei to resonate, producing a transverse magnetization. The transverse magnetization induces a voltage or signal in the receiver coils. In contrast to other imaging modalities, the signal originates from the whole object instead of a single point within the object. Therefore, an encoding scheme is needed to locate the signal and obtain an image. The key to signal encoding in MRI is magnetic field gradients which causes the protons to precess at different frequencies depending on their position. One gradient is applied along each axis to encode the protons' position along that axis. Thus, three gradients in total are used in the encoding scheme, one for each step: slice selection, frequency encoding and phase encoding. The three gradients and their timing in a spin-echo pulse sequence are shown in Figure 12.

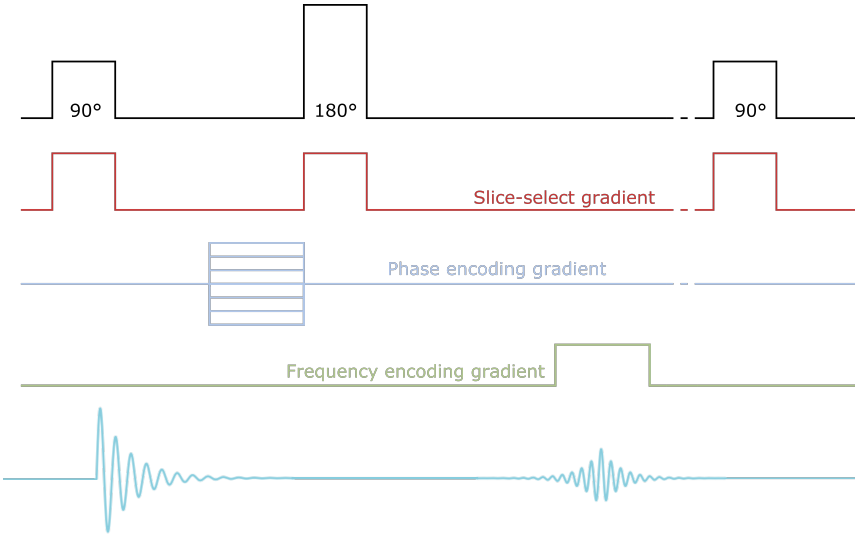

Figure 12: Schematic illustration of when the gradients are applied during a spin-echo pulse sequence to encode the position of the protons.

3.5.1 Slice selection

The first step in spatial encoding is slice selection. A gradient is applied along B_0 or the z-axis, as illustrated in Figure 13a. The precession frequency is proportional to the magnetic field strength, thus the gradient causes the protons to precess at different frequencies depending on their position, as shown by Figure 13b. At the same time as the gradient is turned on, the RF excitation pulse is applied, as shown in Figure 12. The excitation pulse will only excite the protons with the same frequency as the B_1 field of the RF pulse. Thus, a slice is selectively excited by an RF pulse that oscillates with the same frequency as the precession frequency of the protons in the slice. The transverse magnetization created by the excitation pulse will be the result of the magnetization of the protons in the slice. Therefore, the signal will originate from the protons in the selected slice only.

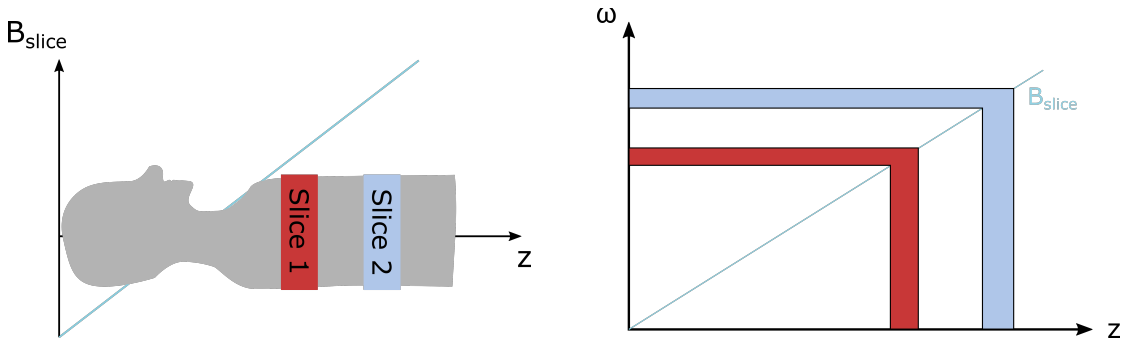

(a) (b)

Figure 13: A slice gradient, B_{slice} represented by the turquoise line is applied in the z-direction. a) Slice 1 in patient will experience a different magnetic field compared to slice 2. The precession frequency ω is linearly related to the magnetic field. Therefore, b) the spins in slice 1 and 2 will precess at different frequencies, ω.

3.5.2 Frequency encoding

After a slice is selected, the position of the signal along both axes of the image is encoded. Usually, the position along the long axis of the anatomy is found through frequency encoding. A linear gradient, called frequency gradient, is applied while the signal is measured, as shown in Figure 12. The gradient alters the magnetic field strength, and thus alters the precession frequency of the protons along an axis linearly and predictably. The protons located at the low end of the gradient will experience a lower magnetic field strength and precess slower than the protons at the high end of the gradient.

The measured signal originates from all the excited protons in the selected slice and is a linear combination of sinusoidal signals. It is stored in a matrix called k-space. Figure 14 shows a k-space where each horizontal line is the signal as a function of time acquired from a single measurement. The frequency of the sinusoidal signals that make up the total signal depends on the position of the protons that give rise to each sinusoidal signal. Thus, the frequency obtained by applying the Fourier transform can be used to encode the position along the frequency encoding direction.

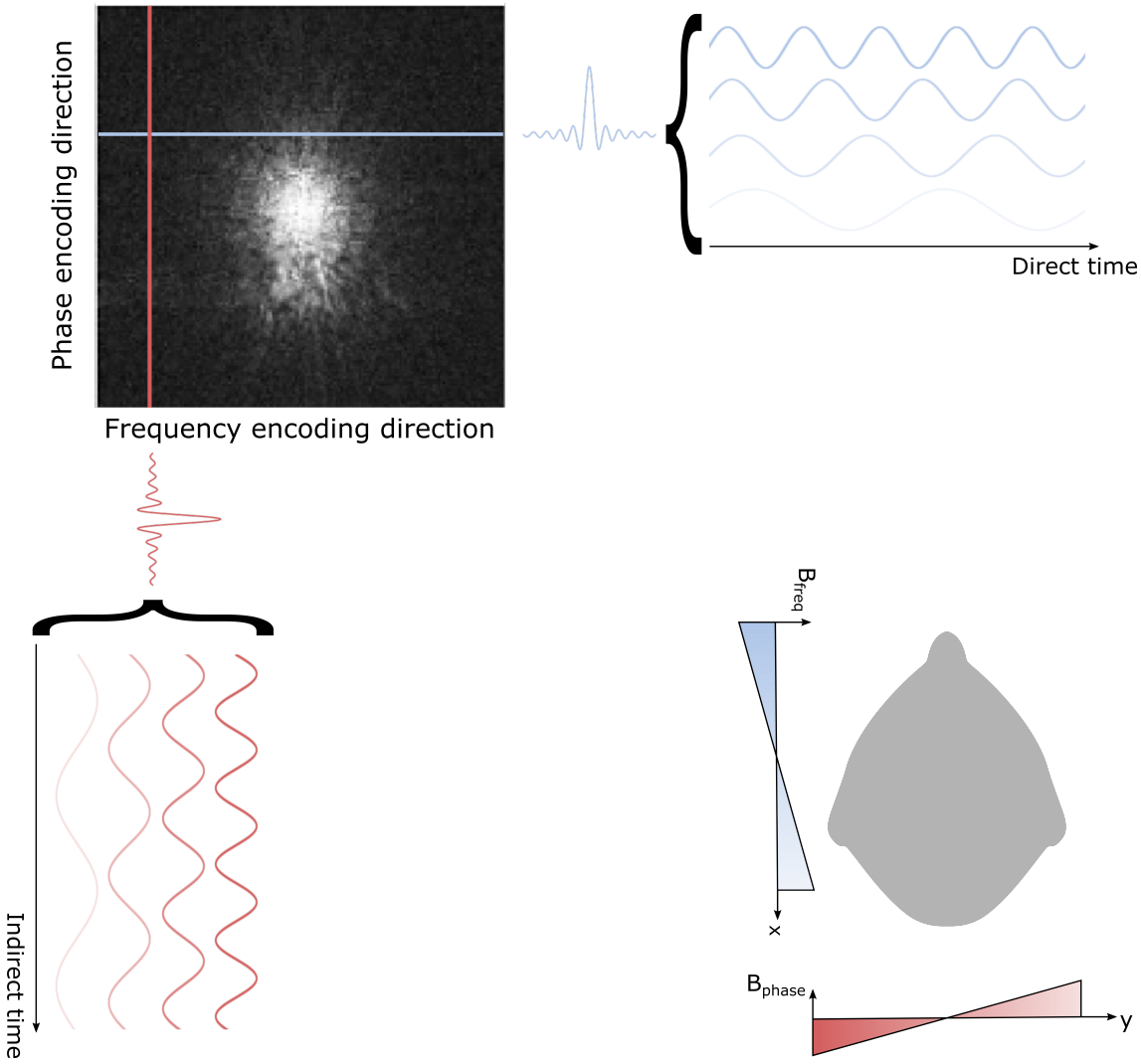

Figure 14: An example of k-space is shown in the upper left corner. Each horizontal line stores the signal from one measurement as a function of time. The signal is a superposition of sinusoidal functions with different frequencies depending on the position of the protons they originate from. The protons have different frequencies due to the frequency gradient, shown in the figure in the lower right corner, that was applied during the measurement. Along the phase encoding direction, the signal as a function of "indirect time" is stored and is composed of sinusoidal functions with different indirect frequencies depending on the position of the protons from which they originate.

3.5.3 Phase encoding

The position along the short axis of the anatomy in the selected slice is found with phase encoding. Before the signal is measured, a linear gradient called phase gradient is turned on for a short time, as seen in Figure 12. The precession frequency of the protons is changed by the gradient and depends on the protons' position. Thus, the amount of accumulated phase along the protons' precession path will depend on their localization. Protons that are located at the high end of the gradient will precess at a higher speed and accumulate more phase than the protons at the low end of the gradient.

The sequence, or measurement, is repeated and with each repetition, the magnitude of the phase gradient is increased. In Figure 12, this is represented by the ladder of phase

gradients. Therefore, each measurement and thus horizontal line in k-space will exhibit a different initial phase shift. Along the y-axis, also called the phase encoding direction, in k-space the phase changes over "indirect time". Because the frequency is a change of phase with time, then the phase change over "indirect time" can be thought of as a frequency in "indirect time" called indirect frequency. The signal from the protons will exhibit different indirect frequencies depending on the location of the protons along the phase encoding direction.

3.5.4 Fourier transform

An example of k-space obtained from an MR acquisition is shown in Figure 14, where each point is the signal from all spins in the selected slice. Here, each horizontal line is the total signal measured over real-time and thus contains the direct frequencies from all the spins in the ensemble. While the vertical lines are signals measured in "indirect time" from the entire spin ensemble and are composed of sinusoidal waves with different indirect frequencies. The direct and indirect frequencies of the sinusoidal waves associated with the protons are related to their location.

To form an image, a 2D Fourier transform is performed where a Fourier transform is applied to the acquired k-space in both the frequency and phase encoding directions. The Fourier transform decomposes an MR signal into a sum of sinusoidal waves with different frequencies, phases and amplitudes. Because the Fourier transform is performed in both directions, both the direct and indirect frequencies are obtained together with their corresponding amplitude. The amplitude of each pair of frequencies represents the intensity of each pixel and will depend on the proton density, as well as the T_1 and T_2 properties of the tissue at the location determined by the indirect and direct frequencies.

3.6 Dynamic contrast-enhanced MRI

Many MRI techniques are valuable in cancer treatment, and one of them is DCE-MRI. It is used to extract functional information regarding the microvasculature of the tissue by analysing its temporal enhancement pattern following an injection of a paramagnetic CA [3].

The CA used for imaging cancer usually contains Gadolinium (Gd) which is a paramagnetic element due to its large number of unpaired electrons [23]. The strong magnetic moment from the Gd can induce relaxation in nearby spins, which reduces the relaxation times of the tissue. The increased magnetic field due to the presence of Gd forces the spins to return to equilibrium faster, and thus the T_1 is shortened. The CA also reduces T_2 because additional variation in the magnetic field causes the spins to dephase faster. In DCE-MRI, the images are T_1-weighted. Thus, the signal in proximity to the CA will increase because the CA enhances the longitudinal magnetization before it is flipped into the transverse plane and measured. Therefore, the introduction of Gd increases the intensity in the regions where the CA is present in the DCE-MRI T_1-weighted images, as illustrated by Figure 15. Figure 15a shows a DCE-MR image before CA is administered and Figure 15b shows the same image after the CA was injected. Some areas show an increased signal intensity, e.g. the tumour which is indicated by the arrow.

To obtain the temporal enhancement pattern, images without CA, called baseline images,

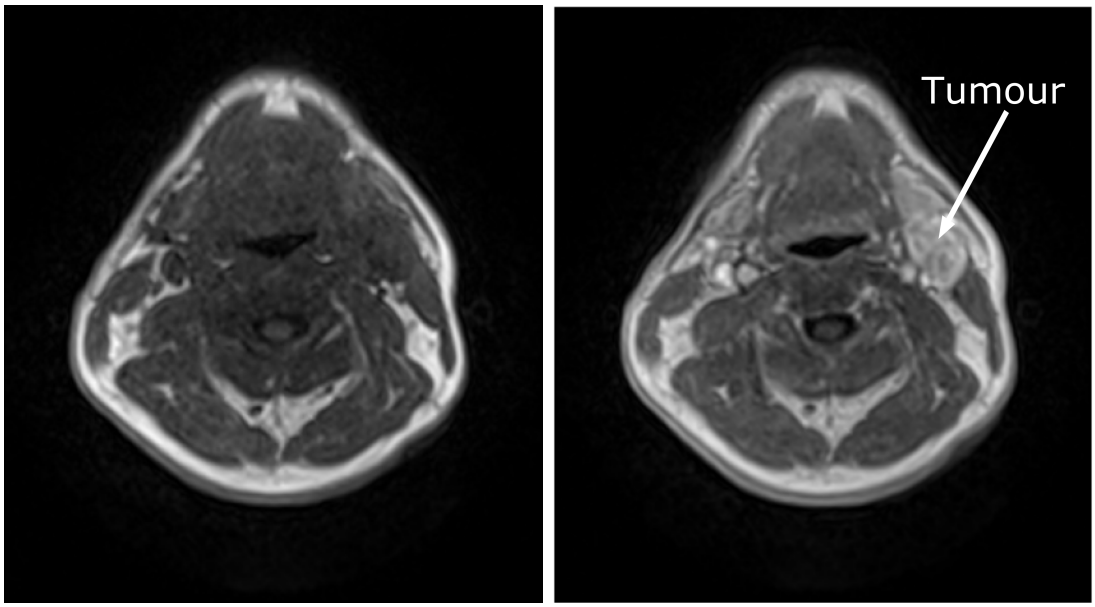

(a) (b)

Figure 15: A dynamic contrast-enhanced magnetic resonance image of a head and neck cancer patient a) before and b) after contrast agent was injected. The arrow indicates the location of the patient's tumour.

are first acquired [10]. Then a bolus of CA is injected intravenously into the patient before a series of images are acquired during and after the CA arrives in the tissue of interest. Figure 16a shows an example of how the signal in a voxel evolves over time. The data points before the sharp increase in signal constitute the baseline signal, i.e. the signal obtained from the tissue without CA. The time from the beginning of the acquisition to the peak of enhancement is called the time to peak (TTP). The enhancement of the signal occurs when the CA arrives in the tissue. The time between the onset of the contrast inflow and the peak of the enhancement is called the wash-in, and the wash-in rate is the maximum slope during that time. As the CA leaves the tissue, the signal reduces with a maximum slope named wash-out rate.

The shape of the time-intensity curve (TIC) is determined by the microvasculature of the tissue [10]. Angiogenesis is one of the hallmarks of cancer and is necessary for tumours to grow rapidly [4]. It leads to highly disorganized vasculature and the formed vessels are of poor quality, resulting in inefficient perfusion. The poor quality of the vessels leads to leakage of CA into the extracellular space [24]. Thus, it takes longer for the CA to leave cancerous tissue which results in a low wash-out rate, as illustrated in Figure 16b. In contrast, the TIC of a large artery will have a high wash-out rate because of the effective perfusion, resulting in a narrow peak, as illustrated by Figure 16b. The wash-in and wash-out rates are two semi-quantitative parameters used in the analysis of DCE-MRI data. It is also common to calculate the area under the enhancement curve (AUC) [3]. The AUC is thought to reflect the tumour perfusion and permeability and has thus been used to predict the patient outcome and evaluate treatment response. Semi-quantitative analysis has the advantage of being easy to implement and some of the parameters are fairly independent of injection protocols. However, the semi-quantitative parameters do not have a clear physiological meaning.

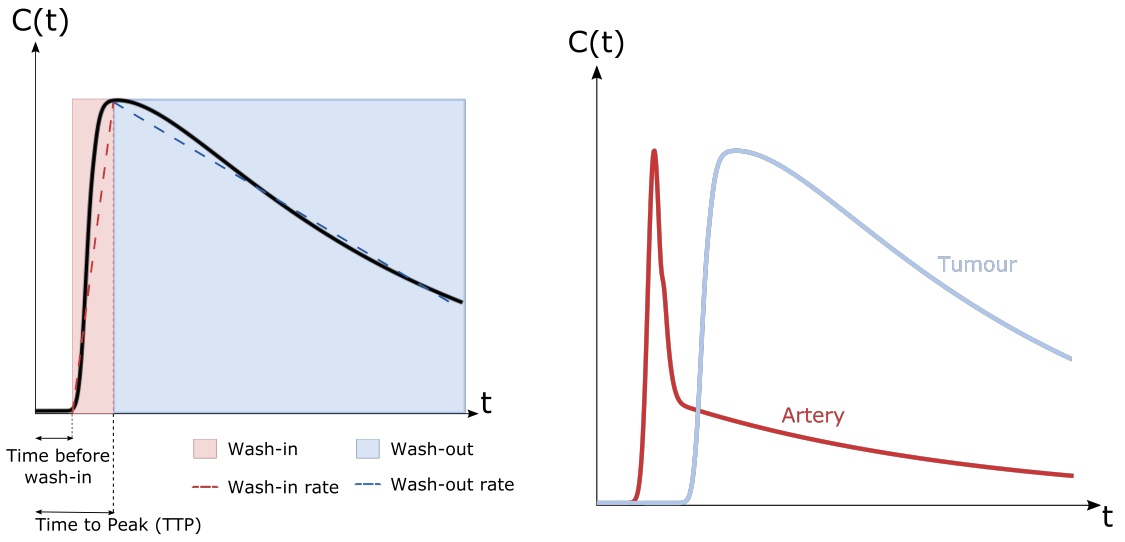

(a) (b)

Figure 16: a) Illustration of a signal enhancement pattern and its properties. b) Example of the signal enhancement pattern obtained from an artery and a tumour.

4 Quantitative mapping with DCE-MRI

The induced TICs in DCE-MRI depend on microvascular parameters, e.g. permeability, surface area of the vessels and blood flow [10]. Appropriate mathematical models can be used to extract these parameters from the TICs to obtain parametric maps [6, 7]. One of the most common models is the two-compartment pharmacokinetic model called the Tofts model [6]. A more advanced Tofts model was later developed, called the extended Tofts model. At the same time as the Tofts model was proposed, another two-compartment model was developed by Brix *et. al.* [7]. This chapter will present the method of acquiring quantitative tissue maps with the Tofts model, the extended Tofts model and the Brix model.

4.1 Tofts and extended Tofts model

The Tofts model is a two-compartment tracer model that describes the transport of CA between the plasma space and extravascular extracellular space (EES), depicted in Figure 17 [6]. It is assumed that the concentration of CA is uniform throughout the compartments. The concentration of CA in the plasma compartment and EES is noted as C_p and C_e, respectively. The EES is the space that leaked CA can reach and it is assumed that the CA leaks from nearby capillaries. The model may be invalid if the CA diffuses into the EES from distant capillaries.

Further, the model assumes linear intercompartment flux, i.e. the flux of CA between two compartments is proportional to the concentration gradient ΔC between the two compartments [6]. This assumption, together with the diffusion theory of molecular transport across a capillary wall, defines the permeability constant P as the flux per unit concentration difference and unit area of permeable membrane:

$$\text{flow of CA} = PSM_t\Delta C \tag{8}$$

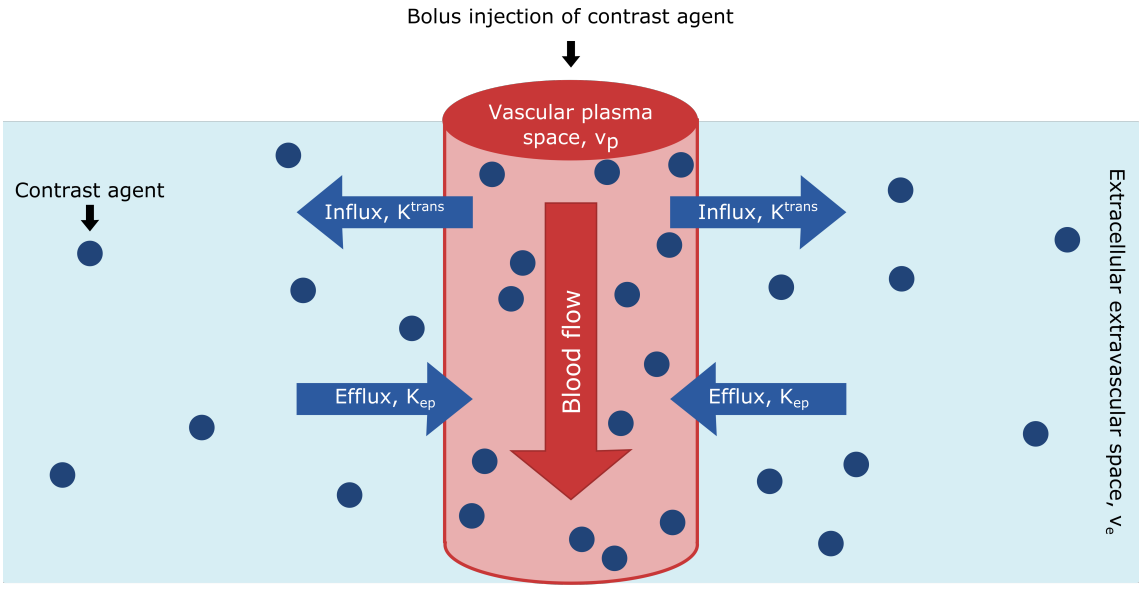

Figure 17: Schematic illustration of the Tofts model. It consists of two compartments: the vascular plasma space and extracellular extravascular space (EES) with fractional volumes v_p and v_e, respectively. Contrast agent is injected in the bloodstream. K^{trans} is the volume transfer constant from the plasma to EES and K_{ep} is the rate constant from EES to the plasma.

Here, S is the area of membrane per unit mass of tissue, M_t is the mass of the tissue of concern and thus SM_t is the unit area of the permeable membrane. Thus, the flux of CA into the EES from the plasma can be expressed using Equation (8):

$$v_e V_T \frac{dC_e}{dt} = (P_{\text{in}} C_p - P_{\text{out}} C_e) S M_t \tag{9}$$

Here, v_e is the volume of EES per unit volume of tissue, and P_{in} and P_{out} are the permeability constants for the flux of CA in and out of EES respectively. Although there may be active transport mechanisms present or a difference in diffusion, viscosity or pressure on each side of the membrane resulting in different permeability constants for the flux of CA in and out of EES, Tofts models assume that $P_{\text{in}} = P_{\text{out}}$ [6]. Thus, Equation (9) can be rewritten to

$$\frac{dC_e}{dt} = \frac{K^{\text{trans}}}{v_e}(C_p - C_e) \tag{10}$$

where $K^{\text{trans}} = P_{\text{out}} S M_t / V_t$ is noted as the volume transfer constant. The CA rate constant from the EES back to the plasma, illustrated in Figure 17, is given by $K_{\text{ep}} = K^{\text{trans}}/v_e$. The differential equation expressed by Equation (10) can be solved with the Laplace transform. By taking the Laplace transform and using the relation $\mathcal{L}\{df(t)/dt\}(s) = s\mathcal{L}\{f(t)\}(s) - f(0)$ we find

$$s\mathcal{L}\{C_e\}(s) - C_e(0) = \frac{K^{\text{trans}}}{v_e}(\mathcal{L}\{C_p\} - \mathcal{L}\{C_e\}) \tag{11}$$

It is reasonable to assume that $C_e(0)$=0. Equation (11) can then be rearranged to

$$\mathcal{L}\{C_e\}(s) = \frac{K^{\text{trans}}/v_e}{1 - K^{\text{trans}}/v_e}\mathcal{L}\{C_p\} \tag{12}$$

Using the convolution theorem, i.e. $\mathcal{L}\{f(t)g(t)\} = f(t)*g(t)$ and that $\mathcal{L}\{e^{-\alpha t}\} = 1/(s+\alpha)$, the CA concentration in the EES can be expressed as

$$C_e(t) = \frac{K^{\text{trans}}}{v_e} \int_0^t C_p(\tau) e^{-\frac{K^{\text{trans}}}{v_e}(t-\tau)} d\tau \tag{13}$$

The total CA concentration C_t in the tissue is a sum of the concentration of CA in the plasma and EES:

$$C_t = v_e C_e + v_p C_p \tag{14}$$

The Tofts model assumes that the plasma volume is negligible ($v_p \approx 0$), while the extended Tofts model takes the plasma volume into account [25]. Thus, the tissue concentration can be expressed as

$$C_t(t) = K^{\text{trans}} \int_0^t C_p(\tau) e^{-\frac{K^{\text{trans}}}{v_e}(t-\tau)} d\tau \tag{15}$$

and

$$C_t(t) = K^{\text{trans}} \int_0^t C_p(\tau) e^{-\frac{K^{\text{trans}}}{v_e}(t-\tau)} d\tau + v_p C_p(t) \tag{16}$$

by the Tofts and extended Tofts model, respectively.

4.2 Brix model

The Brix model is another popular two-compartment model applied in DCE-MRI [7]. The main advantage of this model compared to the Tofts and extended Tofts model is that an AIF and T_1 maps are not required to calculate the pharmacokinetic parameters [25]. Similar to the Tofts and extended Tofts model, the Brix model contains two compartments: the plasma and EES. There is a linear exchange of CA between the two compartments in both directions [7]. Thus, the flux of CA can be expressed by the following differential equations:

$$\frac{dM_p}{dt} = K_{\text{in}} - (K_{\text{pe}} + K_{\text{el}})M_p + K_{\text{ep}} M_e \tag{17a}$$

$$\frac{dM_e}{dt} = K_{\text{pe}} M_p - K_{\text{ep}} M_e \tag{17b}$$

where K_{in} is the infusion rate of CA, K_{el} is the rate constant for elimination of CA from the plasma compartment, K_{pe} is the rate constant for transfer of CA from the plasma to the EES and K_{ep} is the rate constant in the opposite direction. The compartment model and its rate constants are visualised in Figure 18.

Brix *et. al.* assumed there were no CA accumulated in the tumour [7]. Therefore, the volume of CA in the EES V_e is insignificant compared to the CA volume in the plasma V_p and $K_{\text{el}}M_p$ and $K_{\text{ep}}M_e$ terms can be neglected in Equation (17). The concentrations of CA in the plasma and EES can be expressed by $C_p = M_p/V_p$ and $C_e = M_e/V_e$, respectively, resulting in Equation (17) being rearranged to:

$$\frac{dC_p}{dt} = \frac{K_{\text{in}}}{V_p} - K_{\text{el}} M_p \tag{18a}$$

$$\frac{dC_e}{dt} = \frac{V_p}{V_e} K_{\text{pe}} C_p - K_{\text{ep}} C_e \tag{18b}$$

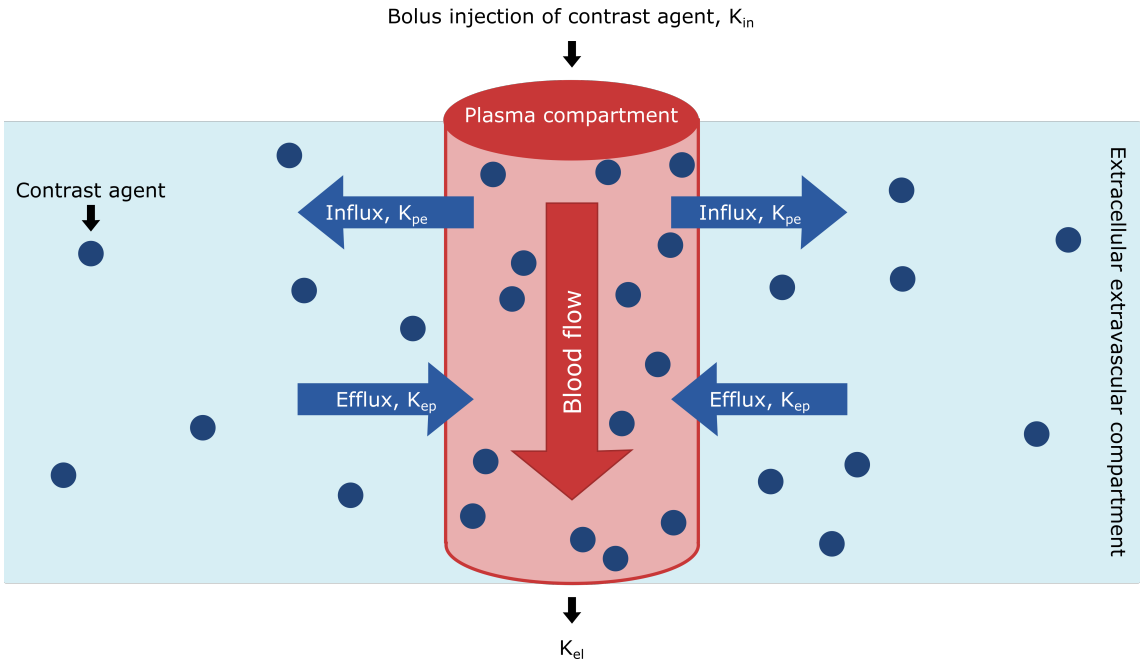

Figure 18: Illustration of the Brix model. It consists of two compartments: the vascular plasma space and extracellular extravascular space (EES). Contrast agent (CA) is injected into the bloodstream with an infusion rate of K^{in}. The rate at which the CA is eliminated from the plasma space is given by K_{el}. K_{pe} and K_{ep} is the rate constant for transfer of CA from the plasma to the EES and vice versa, respectively.

The differential equations expressed by Equations (18)a,b can be solved. Using the initial conditions $C_p(0) = 0$ and $C_e(0) = 0$, the concentrations can be expressed by

$$C_p(t) = \frac{K_{\text{in}}}{V_p K_{el}} \left(e^{K_{\text{el}} t'} - 1\right) e^{-K_{\text{el}} t} \tag{19a}$$

$$C_e(t) = \frac{K_{\text{in}} K_{pe}}{V_e} \left(v \left(e^{K_{\text{el}} t'} - 1\right) e^{-K_{\text{el}} t} - u \left(e^{K_{\text{ep}} t'} - 1\right) e^{-K_{\text{ep}} t}\right) \tag{19b}$$

with $v = \{K_{\text{el}}(K_{\text{ep}} - K_{\text{el}})\}^{-1}$ and $u = \{K_{\text{ep}}(K_{\text{ep}} - K_{\text{el}})\}^{-1}$. Before all the CA has been injected, t'=t in Equations (19)a and (19)b, while after CA has been injected t' equals the time at which injection of CA is finished.

The signal enhancement was assumed to be proportional to the concentration of CA in the tissue. Thus, the enhanced signal S(t) in the EES as a function of time can be described by:

$$\frac{S(t)}{S(0)} = 1 + \frac{A}{K_{\text{ep}} - K_{\text{el}}} \left(\frac{\left(e^{K_{el} t'} - 1\right) e^{-K_{\text{el}} t}}{K_{\text{el}}} - \frac{\left(e^{K_{\text{ep}} t'} - 1\right) e^{-K_{\text{ep}} t}}{K_{\text{ep}}} \right) \tag{20}$$

Here, S(0) is the signal from the EES in the absence of CA and A is a scalar constant.

4.3 Image acquisition

The Tofts model requires several measurements to calculate the microvascular parameters [3]:

(i) A map of the T_1 values (T_{10} map) before injection of CA needs to be acquired to calculate the concentration of CA in the tissue.

(ii) Acquisition of T_1-weighted images before, during and after CA injection to obtain the TICs. High temporal resolution is important to calculate accurate pharmacokinetic parameters.

(iii) The AIF, i.e. the concentration of CA in the blood plasma of a feeding artery as a function of time, is essential to calculate the parametric maps.

The T_{10} map can be obtained through different methods, the most common is the so-called Look-Locker and variable flip angle (VFA) techniques [26].

4.4 Arterial input function

A key component of the Tofts models is the AIF [6]. The AIF is the concentration of CA in a supplying artery as a function of time and can be obtained by different methods [3]. The accuracy of the AIF significantly affects the accuracy of the pharmacokinetic parameters obtained with the Tofts model because it serves as an input to the model [27]. Therefore, it is important to generate an accurate and patient-specific AIF. It is common to divide the methods into two groups: individual AIF and population AIF.

4.4.1 Individual and population AIF

A region of interest (ROI) within an artery, usually the coronary artery, is chosen with a fully manual, semi-automated or fully automated approach [27]. The manual approach has significant variability associated with it due to flow artefacts in the major arteries. If the arterial ROI is manually selected, it is thus advisable to choose the image slice that contains the central portion of the artery, as well as selecting the high-intensity pixels, to minimize the partial volume effects [28]. It may be better to select the ROI with a semi-automatic tool, such as those proposed by Li X *et al.* [29] and Ashton E *et al.* [30], to reduce the inter-operator variability in the resulting AIF. There are also some fully automated selection tools, e.g. a conventional tool proposed by Chen J. *et al.* [27] and a deep-learning-based tool proposed by Nalepa *et al.* [31]. They are often organ- and sequence-specific and may need to be modified.

After choosing an ROI, the arterial TIC is calculated by averaging over the cross-section of the arterial ROI [28]. The intensity is then converted to concentration, resulting in the AIF. Figure 19 shows an example of a delineated artery and the resulting AIF. Most of the semi-automatic and fully automatic tools not only determine the ROI but also calculate the resulting AIF [27, 29, 31]

However, in some cases, there are no arteries in the proximity of the organs of interest. Therefore, an individual AIF can not be obtained and a population AIF is used instead, e.g. population-averaged AIF described by Parker *et al.* [9] or population AIF derived from data reported by Fritz-Hansen [32]. The individual AIFs are patient-specific, and thus in general lead to more accurate pharmacokinetic parameters than population AIFs [9].

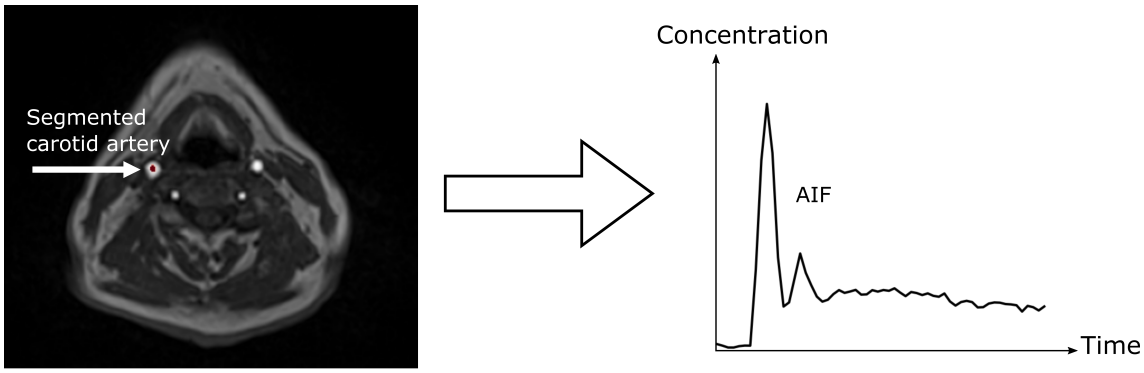

Figure 19: An example of a delineated artery and the resulting arterial input function.

4.4.2 Population AIF by Parker *et al.*

Parker *et al.* proposed that the AIF is a mixture of two Gaussians in addition to an exponential modulated by a sigmoid function [9]:

$$C_p(t) = \sum_{n=1}^{2} \frac{A_n}{\sigma_n \sqrt{2\pi}} e^{-(t-T_n)^2/2\sigma_n^2} + \alpha \frac{e^{-\beta t}}{1 + e^{-s(t-\tau)}}. \tag{21}$$

Here, A_n, T_n and σ_n are the scaling constants, centers and widths of the n^{th} Gaussian; α and β are the amplitude and decay constant of the exponential; and s and τ are the width and center of the sigmoid that modulates the exponential, respectively. The population AIF can be found by fitting Equation (21) to the mean AIF measurement of several patients [9].

4.5 Concentration calculation

The Tofts model requires the concentration of CA as a function of time to calculate the pharmacokinetic parameters. The CA concentration in homogeneous tissue can be expressed as a function of post-contrast longitudinal relaxation time T_1 [6]:

$$C(t) = \frac{1}{r_1}\left(\frac{1}{T_1} - \frac{1}{T_{10}}\right) \tag{22}$$

Here, r_1 is the specific relaxivity of the CA and T_{10} is the pre-contrast relaxation time. Equation 22 is derived under the assumption of contant specific relaxivity. It is also assumed that there is fast exchange of all mobile protons within the tissue, i.e. Gd is evenly distributed, and thus the tissue relaxation can be described by a single T_1 value [6]. This assumption appears to hold for exchange of protons between the cellular and extracellular spaces. However, the exchange between vascular and extravascular spaces is slow leading to errors when modelling the concentration of Gd-DTPA in the plasma.

It is common to use a fast, low-angle shot (FLASH) sequence for pharmacokinetic analysis. The signal equation of the FLASH sequence is

$$S(t) = M_0 \sin\alpha \frac{1 - e^{TR/T_1}}{1 - \cos\alpha e^{-TR/T_1}} \tag{23}$$

where TR is the repetition time, α is the flip angle and M_0 is the thermal equilibrium magnetization. Defining the pre-contrast signal intensity as S_0=S(0), the signal enhancement can be expressed as

$$\frac{S(t)}{S_0} = \frac{\frac{1-e^{-TR/T_1}}{1-\cos\alpha e^{-TR/T_1}}}{\frac{1-e^{-TR/T_{10}}}{1-\cos\alpha e^{-TR/T_{10}}}} \tag{24}$$

by using Equation (23). Equation (24) can be rewritten to express the postcontrast relaxation time as

$$\frac{1}{T_1} = -\frac{1}{TR}\ln\left(\frac{1-B\frac{S(t)}{S_0}}{1-B\cos\alpha\frac{S(t)}{S_0}}\right) \text{ where } B = \frac{1-e^{-TR/T_{10}}}{1-\cos\alpha e^{-TR/T_{10}}}. \tag{25}$$

The concentration can be obtained by calculating $1/T_1$ using Equation (25) and inserting the values into Equation (22), together with the values from a T_{10} map.

5 Methods

5.1 Patient population and treatment

In this study, 20 patients from the EMINENCE study were included. The patients had untreated head and neck cancer which was histologically confirmed as squamous cell carcinoma. The head and neck region includes the pharynx, larynx, oral cavity and sinonasal area. Some of the patients had lymph node metastasis, in addition to the primary tumour. The patients were treated with radiotherapy or surgery at St. Olavs Hospital with curative intent. Some patients also got concomitant chemotherapy. Each patient gave their written consent to be part of the study and the investigation was approved by the Regional Committee for Medical Research Ethics in Central Norway (approval number 2019/64744).

5.2 DCE-MRI data acquisition

MRI was performed on a 1.5T MRI scanner (Magnetom Avanto, Siemens) with a head and neck coil prior to the treatment as part of the diagnostic work-up. A VFA measurement was acquired to calculate the T_1 map and was followed by a B1 mapping acquisition. The VFA measurement was conducted using a T_1-weighted spoiled gradient-echo sequence for five flip angles: 2, 10, 15, 20 and 25 degrees with the specifications listed in Table 1. The B1 map was acquired with a proton-weighted spoiled gradient-echo sequence with the imaging parameters that are listed in Table 1. The T_1 map was corrected for inhomogeneities in the magnetic field using the B1 map.

DCE-MRI was performed after obtaining the T_1 and B1 maps. The DCE-MRI consisted of 60 consecutively acquired axial volumes with a temporal resolution of 3.735 s. Similar to the VFA measurement, the DCE-MRI sequence was a T_1-weighted spoiled gradient-echo sequence with the specifications listed in Table 1. Four pre-contrast images were

Table 1: Spesifications of the sequences that were performed to obtain maps of T_1 and B1, and the DCE-MR images.

Measurement	TR (ms)	TE (ms)	Flip angle	Matrix size	Slices	Voxel size (mm^3)	Averages
T_1 map	4.76	1.95	2°, 10°, 15°, 20°, 25°	154 × 192	48	1.68 ×1.35×4	1
B1 map	3800	1.88	79.99	52 × 64	16	5.92×5.94×8	1
DCE-MRI	3.04	1.11	12	288×320	22	0.78×0.78×4	1

acquired, and thus the first four time frames of the signal enhancement curves constitute the baseline. The CA, gadoterate meglumine (Clariscan), was injected automatically in a bolus dose of 2 ml/kg of body weight with an injection rate of 3 ml/s. The injection was followed by a 20 ml saline flush with an injection speed of 3 ml/s. The same imaging and CA administration protocols were followed for all the patients in the study to ensure uniform data collection.

5.3 DCE-MRI data processing and analysis

The T_1 map and the DCE-MRI data were exported as DICOM files and converted to nifti files. Before the conversion, the T_1 map was reconstructed to exhibit the same matrix size as the DCE-MR images. The data was then processed and analysed using an in-house Python script which can be accessed from the GitHub repository `https://github.com/martehoiskar/DCE-MRI`. Part of the code required to use the Tofts models for model fitting was taken from the GitHub repository `https://github.com/welcheb/pydcemri/blob/master/dcemri.py`, though some modifications were made.

5.3.1 Extraction of the AIF

The voxels for the AIF were manually selected from the left carotid artery for each patient. The CA arrives in the arteries first, and thus the arteries were found by observing where the signal enhancement occurred first. The time frame with maximum signal enhancement was used to delineate the artery. The image slice with the central portion of the artery was selected to minimize partial volume effects. Only the voxels in the centre of the artery were included in the segmentation to ensure that all the voxels were inside the artery. Delineation was performed in 3D Slicer with the Segmentation Editor by a single observer and an example of the segmentation of an artery is seen in Figure 20.

The individual AIF, denoted AIF_{ind}, was calculated using the same approach for each patient. The patient's arterial TIC was obtained from the DCE MR images by averaging over the TIC from each voxel in the arterial ROI of the patient, as illustrated in Figure 21. The arterial TIC was converted to tracer concentration using Equation (22) with a specific relaxivity of 3.1 $(s\ mM)^{-1}$ [33], a constant T_{10} of 1550 s as found in literature [34] and defining S_0 as the average over the first four time frames arterial TIC. The resulting time-concentration curve (TCC) gave rise to the AIF_{ind}, as shown by Figure 21.

Six different population AIFs were obtained and the names of the AIFs were given the subscript pop. The arterial TICs from 20 different patients were either not aligned, aligned using the peaks or aligned using the time of wash-in of the arterial TICs. The average of the patients' TTP and the average of the time of wash-in were used as the new TTP and the new time of wash-in for the population AIF composed of arterial TICs with aligned peaks

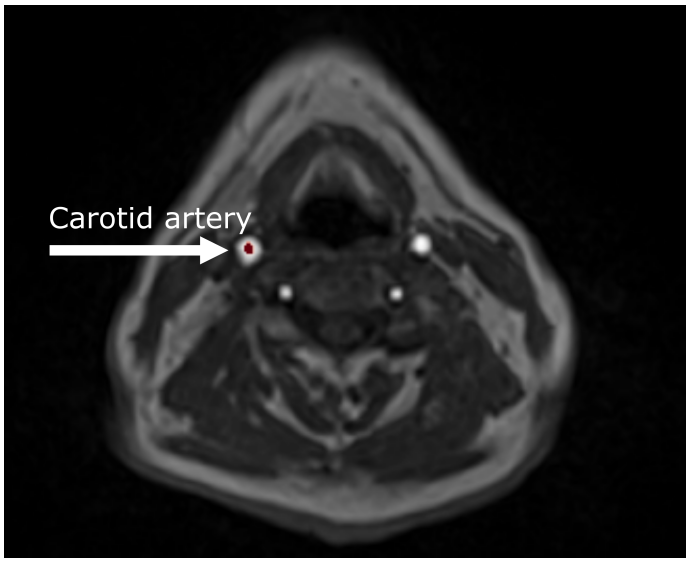

Figure 20: An example of the delineation of the arterial region of interest used to calculate the individual arterial input function for one of the patients. Here, the delineation is depicted on a post-contrast T_1-weighted image where the signal in the arteries was at its strongest.

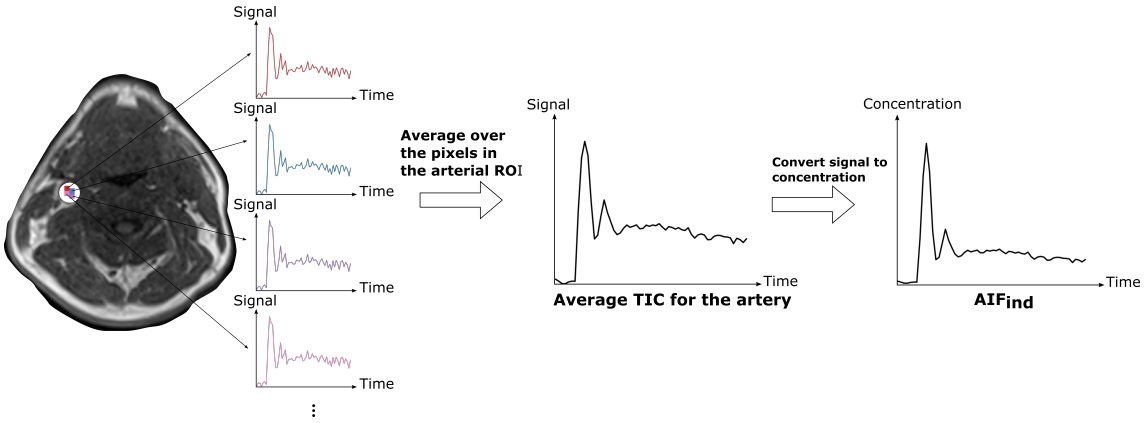

Figure 21: Flowchart of the calculation of the individual arterial input function, $\mathrm{AIF_{ind}}$. The arterial region of interest (ROI) was delineated and here it is represented by the white circle. The time-intensity curve (TIC) was found for each voxel inside the arterial ROI. Here, four of the voxels in the arterial ROI are drawn in different colours. Then the mean of the TICs over the voxels in the arterial ROI was calculated, resulting in a mean TIC for the artery. Then, the mean TIC was converted to concentration which lead to a time-concentration curve (TCC), also called the $\mathrm{AIF_{ind}}$.

and the population AIF with aligned times of wash-in, respectively. Further, for each type of alignment (including the no alignment) the baseline was either included or removed. The baseline refers to the first four time frames of the patients' arterial TICs. Then, the average of the arterial TICs from the patients was calculated and then converted to a TCC in the same manner as the arterial TICs, resulting in six TCCs that represented the population AIFs: $\mathrm{AIF_{pop,\,bl}}$, $\mathrm{AIF_{pop}}$, $\mathrm{AIF_{pop,\,pa,\,bl}}$, $\mathrm{AIF_{pop,\,pa}}$, $\mathrm{AIF_{pop,\,wia}}$, $\mathrm{AIF_{pop,\,wia,\,bl}}$. Here, the subscripts pa, wia and bl stand for peak alignment, wash-in alignment and baseline included, respectively. This process is also illustrated by the flowchart in Figure 22. Equation (21) was fitted to each of the six population AIFs, using Python's *curve_fit* function from the *scipy.optimize* package, to obtain the functional form of the population

AIFs.

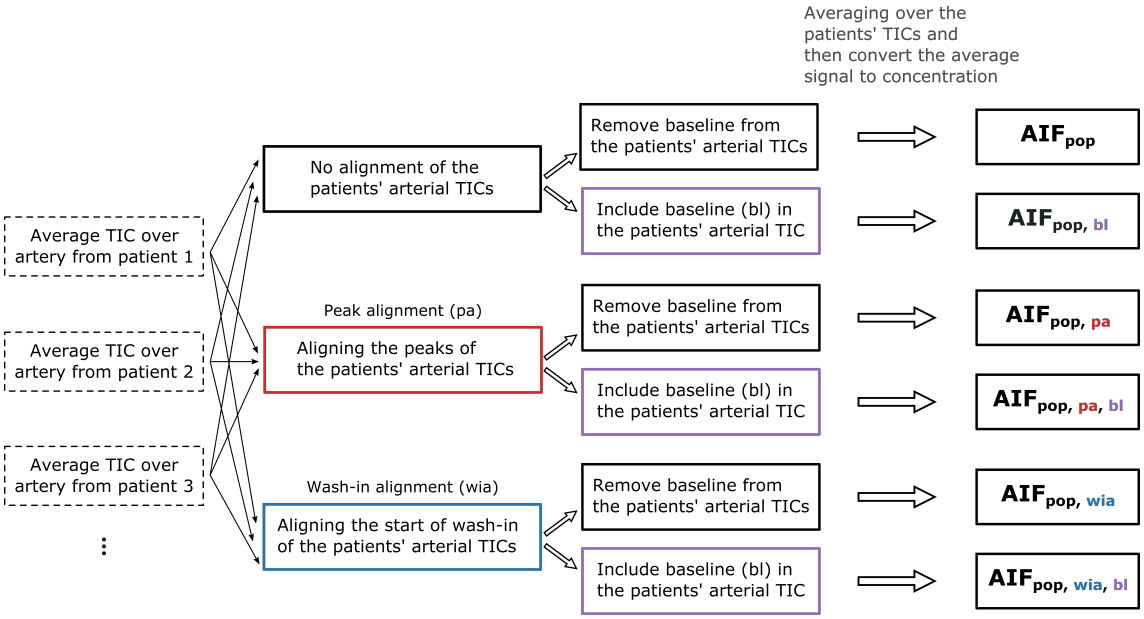

Figure 22: Flowchart of the calculation of the population arterial input functions. The arterial time-intensity curves (TICs) from 20 patients were either not aligned, aligned using the peaks or aligned using the time of the wash-in of the time-intensity curves. The baseline was either included or removed from the time-intensity curves. Then the average of the patients' time-intensity curves were taken before being converted to time-concentration curves (TCCs), resulting in six different population arterial input functions: $\mathrm{AIF}_{\mathrm{pop,\ bl}}$, $\mathrm{AIF}_{\mathrm{pop}}$, $\mathrm{AIF}_{\mathrm{pop,\ pa,\ bl}}$, $\mathrm{AIF}_{\mathrm{pop,\ pa}}$, $\mathrm{AIF}_{\mathrm{pop,\ wia}}$, $\mathrm{AIF}_{\mathrm{pop,\ wia,\ bl}}$.

5.3.2 Tracer kinetic modeling

Malignant lymph nodes were manually delineated by physicians at St. Olavs Hospital on CT images. The delineations on CT images were used as guidance to discern the lymph nodes in the DCE-MR images. The lymph nodes were manually drawn in DCE-MR images in 2D in the 20th time frame on each image slice that contained a part of the lymph node. The T_2-weighted images were also used to provide additional information on the position and extent of the lymph node. The delineation was performed in 3D Slicer using the Segmentation Editor. The MultiVolumeExplorer in 3D Slicer was also used to examine the TICs of the voxels. Voxels with TICs that had abnormal shapes for malignant lymph nodes were discarded. Here, abnormal TICs refer to TICs without the characteristic shape shown in Figure 16 and that look like noise instead. In total, 17 cancerous lymph nodes were delineated.

Figure 23 shows a flowchart of the calculation of the pharmacokinetic parameters and the AUCs. The calculation of the parameters was divided into two steps: calculating enhancement curves and model fitting or AUC calculation. The parameters were calculated both on a voxel-by-voxel basis and on an ROI basis. Calculations on a voxel-by-voxel basis mean that the model fitting or integration over the enhancement curve was done for the enhancement curve of each voxel in the delineated lymph node. This results in parametric 3D maps of the lymph node for each of the pharmacokinetic parameters and AUCs, as illustrated in Figure 24a. While calculations on a mean ROI basis mean that the mean enhancement curves of all voxels in the lymph node ROI were calculated and then the

model fitting or AUC calculation was conducted, resulting in a single set of parameters for each lymph node ROI, as shown by Figure 24b

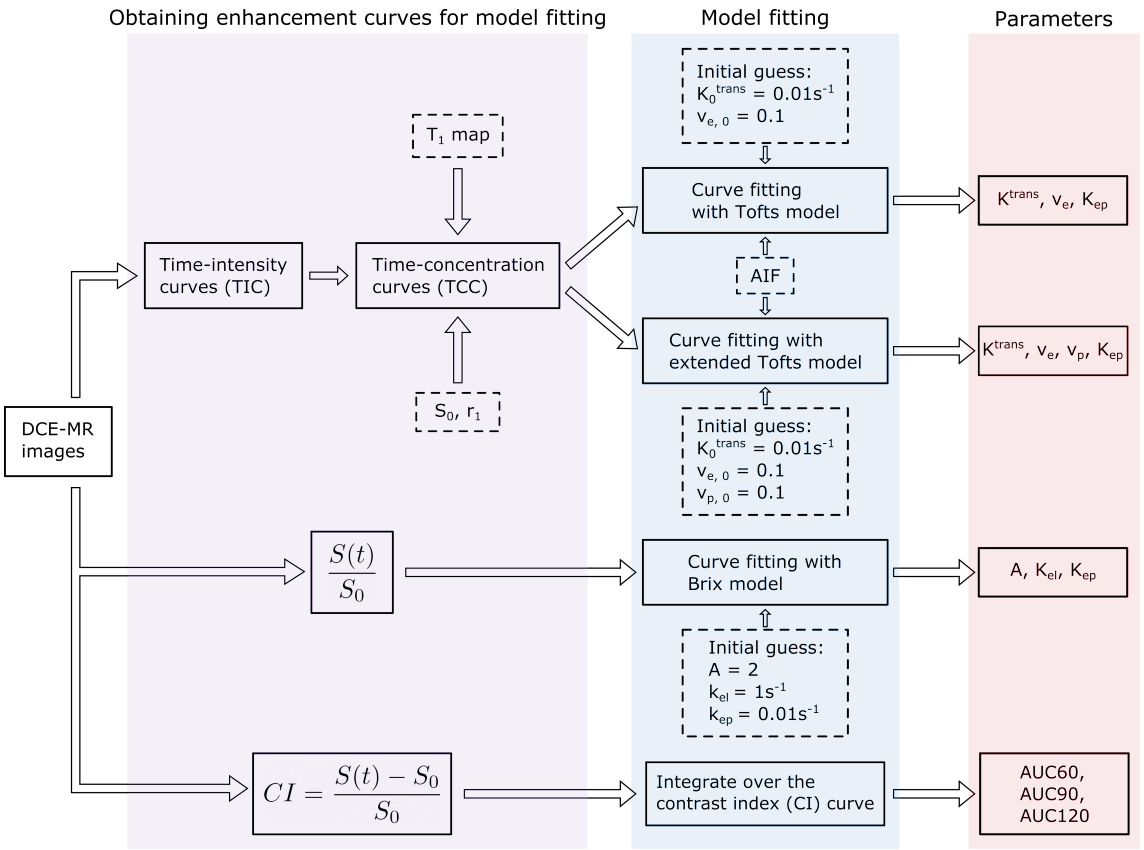

Figure 23: Flowchart of how the pharmacokinetic parameters and the areas under the curve (AUCs) were calculated. The enhancement curves, represented by time-concentration curves (Tofts or extended Tofts model), signal ratios (Brix model) or contrast index (AUC calculations), were obtained for each voxel in the delineated lymph node in the DCE-MR images. Model fitting of the TCCs using the Tofts or extended Tofts model resulted in the parameters K^{trans} and v_e or K^{trans}, v_e and v_p, respectively. The parameters A, K_{el} and K_{ep} were obtained from the model fitting of the signal ratio curves with the Brix model. The areas under the curve were calculated by integrating over the contrast index (CI) curve. For each of the parameters, a 3D parametric map of the lymph node was created. In addition, a mean region of interest (ROI) analysis calculated the mean enhancement curves over the voxels in the lymph node. The model fitting or AUC calculations were performed on the mean ROI enhancement curves, resulting in a single set of parameters for the lymph node.

The Tofts model and the extended Tofts model were applied to calculate the pharmacokinetic parameters for each patient. Model fitting was first performed on a voxel-by-voxel basis within the lymph node volume for each patient. The TICs for each voxel in the lymph node were converted to TCCs using Equation (22) with a specific relaxivity of 3.1 $(\text{s mM})^{-1}$. The T_{10} value in Equation (22) was determined by the T_1 map and S_0 was defined as the average over the first four time frames. By applying the Levenberg-Marquardt least-squares minimization method with the *curve_fit* function from the *scipy.optimization* package in Python, curves were fitted to the TCC using Equation (15) and (16) to obtain the pharmacokinetic parameters expressed by the Tofts and extended Tofts model, respectively. Both the Tofts and extended Tofts model extract the parameters K^{trans} and v_e, but the extended Tofts model additionally extracts v_p. K_{ep} was then calculated us-

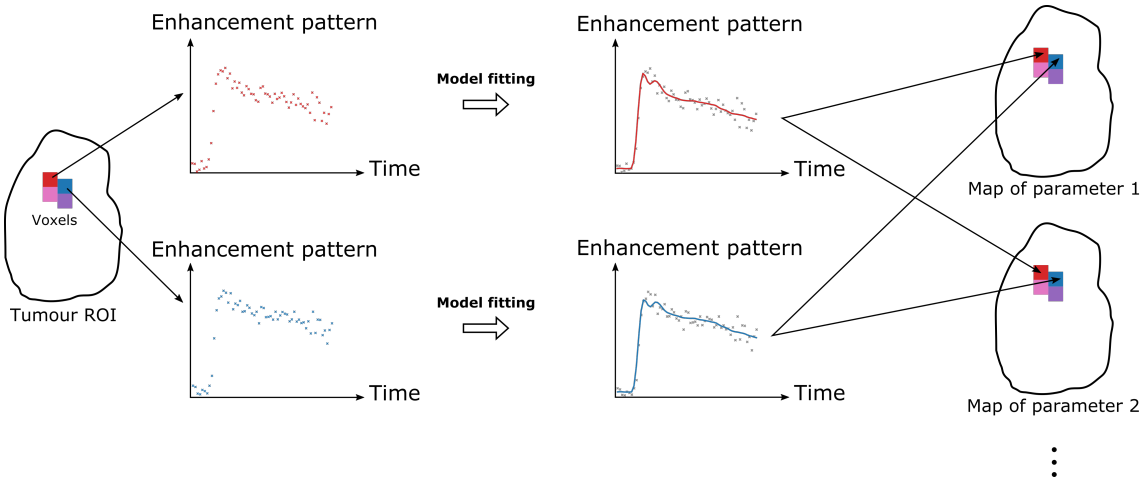

(a) Voxel analysis

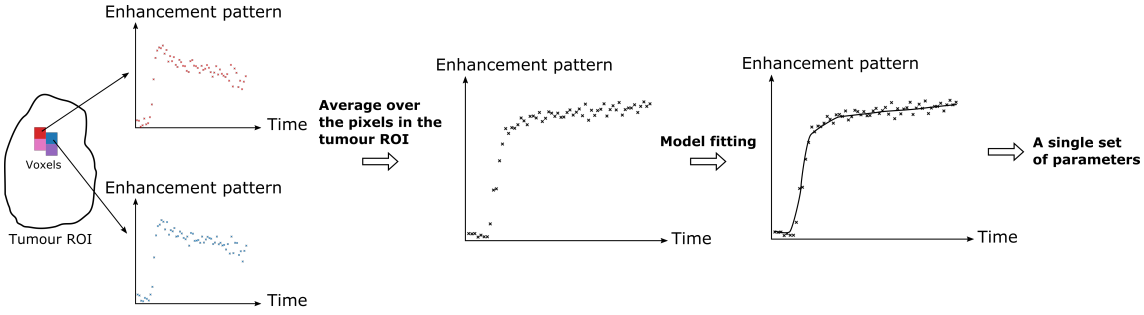

(b) Mean ROI analysis

Figure 24: Illustration of a) the voxel analysis and b) the mean region of interest (ROI) analysis. In a voxel analysis, the enhancement pattern is calculated for each voxel in the lymph node region of interest and then model fitting is performed for each voxel. This results in a parametric map of the lymph node for each parameter. In contrast, the mean ROI analysis average over the enhancement patterns of the voxels in the lymph node ROI. This results in a mean ROI enhancement pattern which the model fitting is performed for and a single set of parameters is obtained for the lymph node.

ing the relation $K_{ep} = K^{trans}/v_e$. The individual AIF was used as the C_p in Equation (15) and (16). The integrals in Equation (15) and (16) were calculated numerically with the Python function *simps* from the *scipy.integrate* package which applies the composite Simpson's rule. The initial guesses for the parameters were $K^{trans} = 0.01s^{-1}$, $v_e = 0.1$ and $v_p = 0.1$. The values were chosen to have the same order of magnitude as found in the literature. Small variations of the initial guess did not have any effect on the fit. Although some of the parameter values were unphysical, the curve fitting was applied without any constraints to the numeric values of the pharmacokinetic parameters to avoid dictating the results. Thus, the unphysical values could be used to observe regions where the models failed.

The enhancement of the signals from the lymph nodes did not occur immediately after the injection as can be observed in Figure 25a. The curve fitting was done on the curve with and without the baseline present for one of the patients to see if the removal of the baseline improved the goodness of the fit. Figure 25 shows the mean TCC for the whole lymph node with and without the baseline and the corresponding fitted curves. The R^2 value for the fitted curves with and without the baseline was 0.91 and 0.74, respectively. Thus, the baseline was included in the TCC because it gave a higher R^2 value.

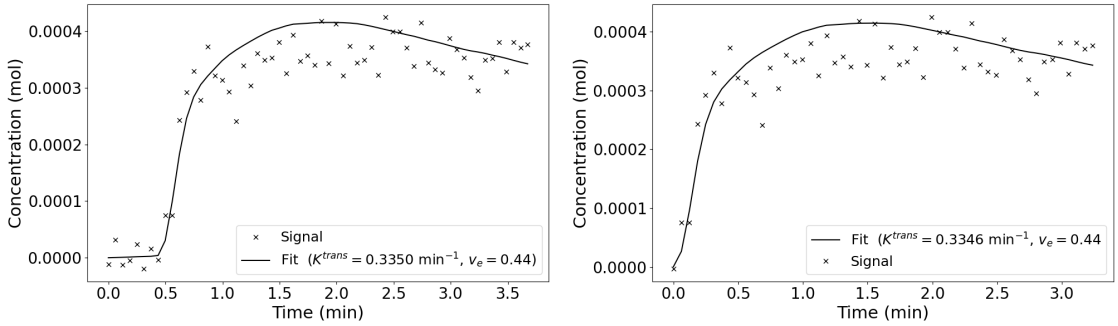

(a) (b)

Figure 25: Plots of the mean time-concentration curve for a single lymph node and the corresponding curve fit which was found using the Tofts model. The curve fit was done a) with and b) without the baseline and had the R^2 value of 0.91 and 0.74, respectively.

Similar to model fitting with the Tofts and extended Tofts model, the model fitting with the Brix model was performed on a voxel-by-voxel basis. The signal ratio S(t)/S(0) was calculated for each voxel with S(0) defined as the average over the first four time frames. The curve defined by Equation (20) was fitted to the signal ratio using the *curve_fit* function from Python to obtain the pharmacokinetic parameters: A, K_{ep} and K_{el}. The initial guess for the parameters was $A = 2$, $K_{ep} = 1\text{s}^{-1}$ and $K_{el} = 0.01\text{s}^{-1}$ which had the right order of magnitude to achieve a fit. The curve fitting was performed on the curve with and without the baseline present for one of the patients to determine if the baseline should be removed. Plots of the mean relative signal intensity for the whole tumour as a function of time are shown in Figure 26, together with the corresponding fitted curves. By removing the baseline, the R^2 value improved from 0.85 to 0.98 and the increased goodness of fit can also be observed in Figure 26. Hence, model fitting with the Brix model was performed on the signal ratio curves without the baseline present.

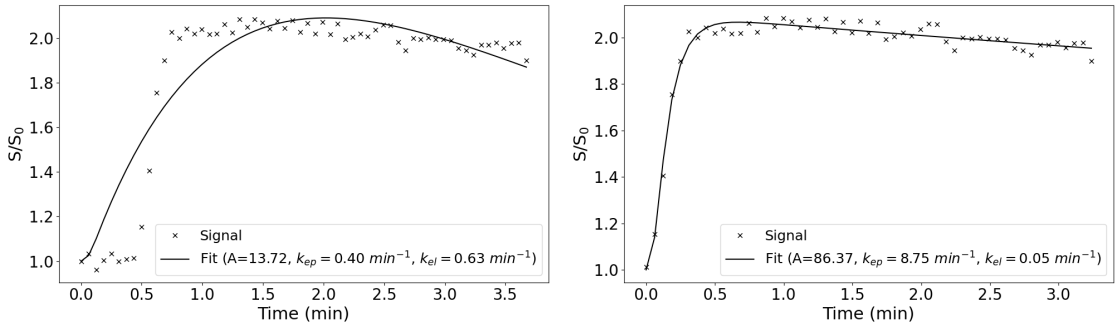

(a) (b)

Figure 26: Plots of the mean relative signal ratio for a single lymph node as a function of time and the corresponding curve fit which was found using the Brix model. The curve fit was done for the mean relative signal ratio curve a) with and b) without the baseline present and had the R^2 value of 0.85 and 0.98, respectively.

In addition to the voxel-by-voxel analysis, a mean ROI analysis was performed for each patient as mentioned previously. For each lymph node, the mean TCC and mean S(t)/S_0 of all voxels were calculated. Then, the Tofts and extended Tofts model were fitted to the mean TCC of the lymph node ROI using the AIF_{ind} of the patient. The Tofts model was also fitted using the six different population AIFs given by their functional forms. When the population AIFs that contained no baseline were used, the baseline was removed from

the mean TCC before curve fitting was performed. In addition, the Brix model was fitted to the mean $S(t)/S_0$ of the lymph node ROI. This resulted in a set of pharmacokinetic parameters, denoted with the prefix mean ROI, for each lymph node.

5.3.3 AUC calculations

Common semi-quantitative parameters are the AUC60, AUC90 and AUC120, which are the area under the contrast index (CI) curve for the first 60, 90 and 120 s after the time of contrast arrival to the lymph node, respectively. In accordance with Matsuzaki *et. al.* [35], the CI:

$$CI = \frac{S - S_0}{S_0} \tag{26}$$

was calculated. Here, S and S_0 are the signal intensity and the baseline, i.e. the mean signal intensity of the first four time frames, respectively. The AUC60, AUC90 and AUC120 were calculated using the Python function *simpson* from the *scipy.integrate* package which uses the composite Simpson's rule to integrate over the CI curve. The AUC calculations were also performed on both a voxel-by-voxel basis and a mean ROI basis. The voxel-by-voxel analysis calculated the AUCs for each voxel in the lymph node ROI, resulting in parametric maps of the lymph node for each AUC. The mean ROI analysis calculated the mean CI of the voxels in the ROI and then calculated the AUCs of the mean CI, resulting in a single set of AUCs for each lymph node.

5.4 Statistical analysis

After the semi-quantitative and quantitative analysis was performed, a statistical analysis was conducted to investigate the different AIFs and compare the different pharmacokinetic parameters, as well as the AUCs.

5.4.1 Comparison between the different AIFs

The mean ROI analysis with the Tofts model produced K^{trans} and v_e for each of the AIFs: AIF_{ind}, $AIF_{pop,\ bl}$, AIF_{pop}, $AIF_{pop,\ pa,\ bl}$, $AIF_{pop,\ pa}$, $AIF_{pop,\ wia}$, $AIF_{pop,\ wia,\ bl}$.

The correlation between the parameters, K^{trans} and v_e, obtained with the population AIFs and the corresponding parameters obtained with the individual AIF was studied to better understand which population AIF we should use in further analysis. The linear relationship between the parameters from calculations with the population AIFs and the corresponding parameters calculated with individual AIF was determined by performing linear regression with Python's function *linregress* from the *scipy.stats* library which produced slopes and intercepts. The individual- and population AIFs can also be compared quantitatively through the concordance correlation coefficient (CCC). The CCC between the two variables x and y was defined by Lawrence Lin [36]:

$$CCC = \frac{2\sigma_{x,y}}{\sigma_x^2 + \sigma_y^2 + (\mu_x - \mu_y)^2}. \tag{27}$$

Here, σ_{xy} is the covariance, μ_x and μ_y are the means for the variables x and y, respectively, and σ_x^2 and σ_y^2 are the corresponding variances. The CCC quantify the degree to which

the pair of two variables (x and y) fall on the line which goes through the origin and produce a 45° angle with the x-axis. The CCC between the parameters calculated with the individual AIF and the corresponding parameters calculated using the population AIF was obtained for all the population AIFs.

5.4.2 Correlation between pharmacokinetic parameters

The Pearson product-moment correlation test was used to study the linear correlation between both the pharmacokinetic parameters and the AUCs. The median $K^{trans}_{IndAIF,\ TM}$, $v_{e,\ IndAIF,\ TM}$, $K_{ep,\ IndAIF,\ TM}$ $K^{trans}_{IndAIF,\ ETM}$, $v_{e,\ IndAIF,\ ETM}$, $v_{p,\ IndAIF,\ ETM}$, $K_{ep,\ IndAIF,\ ETM}$, $K_{ep,\ Brix}$, K_{el}, A, AUC60, AUC90 and AUC120 over all voxels in the lymph node ROI were calculated for each lymph node. Then, the Pearson correlation coefficients (CC) comparing these parameters were obtained with Python's function *pearsonr* from the *scipy.stats* library, together with the corresponding p-values. The pharmacokinetic parameters produced by fitting the models to the mean enhancement curves for each the lymph node were calculated as well and denoted as mean ROI values. Similar to the median values, the Pearson CCs comparing both the mean ROI pharmacokinetic parameters and mean ROI AUCs were calculated, together with the corresponding p-values.

6 Results

6.1 Arterial input function

The individual AIFs that contributed to the population AIFs were plotted as a function of time, as shown in Figure 27, together with one of the population AIFs, $AIF_{pop,\ bl}$. The individual AIFs that belonged to patients 31, 38, 41 and 42 deviated strongly from the population AIFs. Table 2 lists the baseline value, S_0, for each patient. Note that the individual AIFs that deviated most from the population AIFs belonged to the patients with the lowest S_0 values.

Table 2: The baseline value, S_0, that was used to convert the magnetic resonance signal to concentration is listed for each patient.

Patient	1	2	5	7	8	11	16	20	22	23	26	31	32	38	39	41	42	44	45	48
S_0	103	113	126	119	114	108	121	110	109	119	105	62	117	80	108	79	64	127	92	100

Six different population AIFs were obtained: $AIF_{pop,\ bl}$, AIF_{pop}, $AIF_{pop,\ pa,\ bl}$, $AIF_{pop,\ pa}$, $AIF_{pop,\ wia,\ bl}$ and $AIF_{pop,\ wia}$. The parameter values for the functional form, defined by Equation (21), of each population AIF are listed in Table 3, together with the population AIF presented by Parker *et. al.* [9]. The population AIFs as a function of time are presented in Figure 28. There were some small deviations between the different population AIFs. The AIFs obtained after aligning the arterial TICs using the peaks or the start of the wash-in had a higher maximum than the AIFs found without any alignment. The curve of $AIF_{pop,\ pa,\ bl}$ and $AIF_{pop,\ pa}$ also had a larger dip after the first-pass peak compared to the other population AIFs.

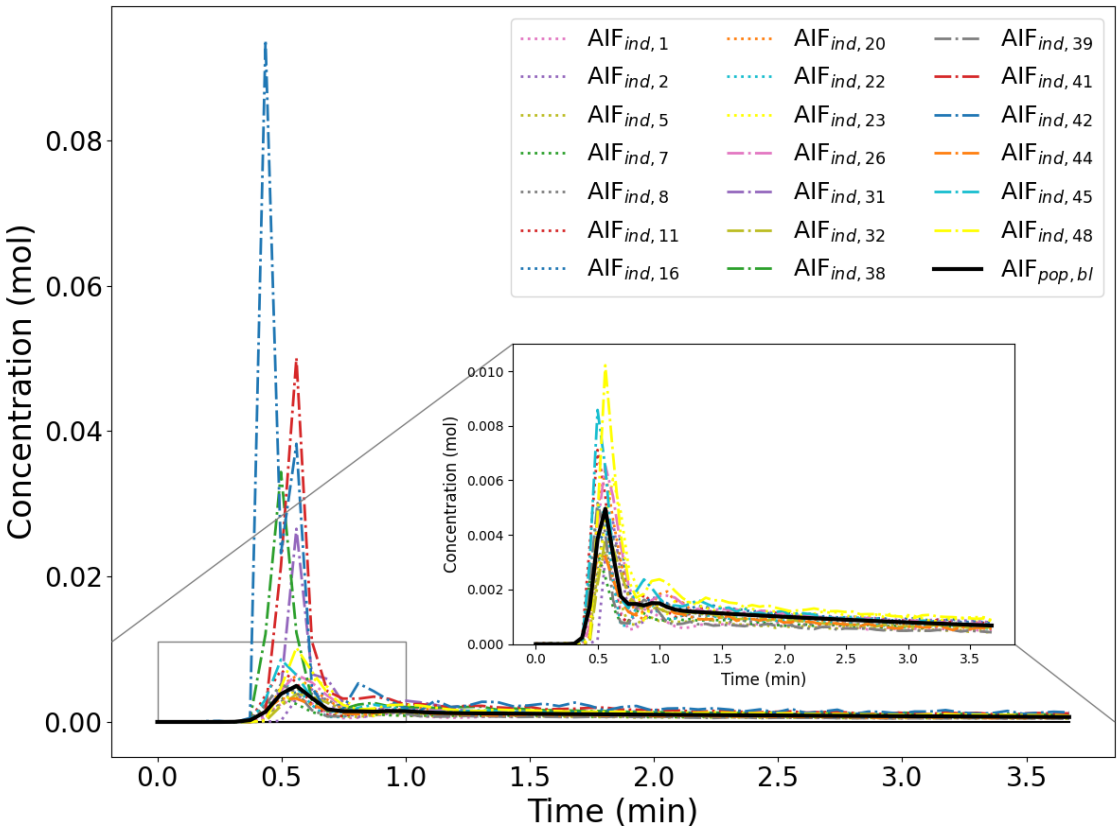

Figure 27: The individual arterial input functions (AIFs) that contributed to the population AIFs were plotted as a function of time. The AIF for patient n was denoted $\mathrm{AIF}_{\mathrm{ind,\,n}}$. One of the six population AIFs, $\mathrm{AIF}_{\mathrm{pop,\,bl}}$ was also plotted.

Table 3: Parameter values for the functional form of the population-based arterial input functions (AIFs): $\mathrm{AIF}_{\mathrm{pop,\,bl}}$, $\mathrm{AIF}_{\mathrm{popl}}$, $\mathrm{AIF}_{\mathrm{pop,\,pa,\,bl}}$, $\mathrm{AIF}_{\mathrm{pop,\,pa}}$, $\mathrm{AIF}_{\mathrm{pop,\,wia,\,bl}}$ and $\mathrm{AIF}_{\mathrm{pop,\,wia}}$ are listed, together with the corresponding standard deviations. The parameters were defined by Equation (21). In addition, the parameter values and their corresponding standard deviations that describe the population AIF obtained by Parker *et. al.*, AIF_{Parker} are included.

Model/Parameter		A_1	A_2	T_1	T_2	σ_1	σ_2	α	β	s	τ
$\mathrm{AIF}_{\mathrm{pop,\,bl}}$	Value	0.84	0.46	0.547	0.78	0.070	0.13	1.59	0.230	28	0.900
	Std	0.03	0.04	0.002	0.10	0.001	0.01	0.04	0.010	6	0.1
$\mathrm{AIF}_{\mathrm{popl}}$	Value	0.72	0.49	0.293	0.47	0.066	0.13	1.54	0.241	30	0.618
	Std	0.06	0.06	0.001	0.02	0.002	0.01	0.03	0.008	4	0.008
$\mathrm{AIF}_{\mathrm{pop,\,pa,\,bl}}$	Value	0.89	0.40	0.572	0.78	0.067	0.13	1.59	0.240	40	0.900
	Std	0.07	0.07	0.002	0.03	0.002	0.02	0.07	0.020	11	0.020
$\mathrm{AIF}_{\mathrm{pop,\,pa}}$	Value	0.70	0.50	0.315	0.45	0.061	0.11	1.59	0.260	124	0.620
	Std	0.10	0.10	0.002	0.03	0.003	0.02	0.05	0.020	1600	0.040
$\mathrm{AIF}_{\mathrm{pop,\,wia,\,bl}}$	Value	0.90	0.46	0.539	0.78	0.069	0.14	1.59	0.230	23	0.910
	Std	0.05	0.06	0.002	0.02	0.002	0.02	0.06	0.020	9	0.030
$\mathrm{AIF}_{\mathrm{pop,\,wia}}$	Value	0.79	0.45	0.284	0.45	0.064	0.12	1.57	0.250	38	0.590
	Std	0.08	0.08	0.002	0.03	0.002	0.02	0.03	0.010	6	0.010
$\mathrm{AIF}_{\mathrm{Parker}}$	Value	0.81	0.33	0.170	0.37	0.056	0.13	1.05	0.169	38	0.483
	Std	0.04	0.04	0.001	0.03	0.001	0.02	0.02	0.006	19	0.015
	Units	mmol.min	mmol.min	min	min	min	min	mmol	min^{-1}	min^{-1}	min

The Tofts model was applied to the mean ROI TCC for 16 lymph nodes to calculate the pharmacokinetic parameters: K^{trans} and v_e. The calculation was performed using each of the six population AIFs and the individual AIF. Figure 30 shows the mean ROI K^{trans} values calculated using each of the six different population AIFs plotted against the mean ROI K^{trans} value found using the individual AIF. The linear regression line is also presented in the plots. The slope, intercept and CCC range between 0.31-0.35, 0.33-0.36 and 0.41-0.43, respectively. It can also be observed that the plots for each population AIF are similar, suggesting that the different population AIFs produced similar pharmacokinetic parameters. Similar plots of v_e is presented by Figure 31. Here, the slope, intercept and CCC range between 0.37-0.38, 0.24-0.25 and 0.52-0.53, respectively. The plots of v_e for each population AIFs in Figure 31 are also similar.

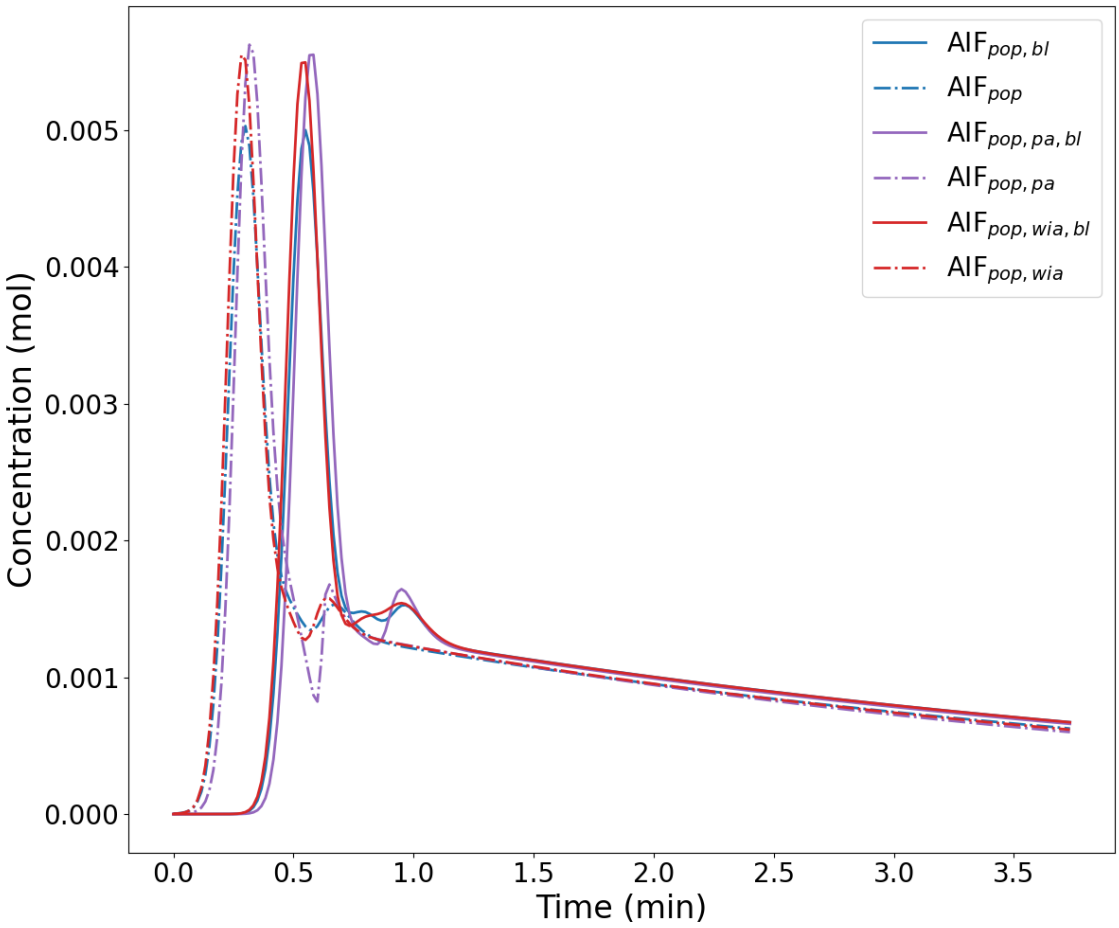

Figure 28: The population arterial input functions: $AIF_{pop,\,bl}$, AIF_{pop}, $AIF_{pop,\,pa,\,bl}$, $AIF_{pop,\,pa}$, $AIF_{pop,\,wia,\,bl}$ and $AIF_{pop,\,wia}$ as a function of time.

6.2 Comparison of Tofts and extended Tofts model

Both the Tofts model and extended Tofts model were applied to calculate K^{trans} and v_e voxel-by-voxel for 16 lymph nodes. The median K^{trans} and v_e over the voxels in the lymph node ROI were calculated for each lymph node. In Figure 29, the median $K^{trans}_{IndAIF,\ TM}$ and $v_{e,\ IndAIF,\ TM}$ for each lymph node were plotted against the corresponding median $K^{trans}_{IndAIF,\ ETM}$ and $v_{e,\ IndAIF,\ ETM}$ respectively. The linear regression lines were also included in the plots, and their slopes and intercepts were close to 1 and 0, respectively. Thus, pairs of the median $K^{trans}_{IndAIF,\ TM}$ and $K^{trans}_{IndAIF,\ ETM}$, and pairs of the median $v_{e,\ IndAIF,\ TM}$ and $v_{e,\ IndAIF,\ ETM}$ fell almost perfectly on the 45° line. This was also expressed by the CCC. The CCCs comparing median $K^{trans}_{IndAIF,\ TM}$ and median $K^{trans}_{IndAIF,\ ETM}$, and median $v_{e,\ IndAIF,\ TM}$ and median $v_{e,\ IndAIF,\ ETM}$ were 0.99 and 1.00, respectively.

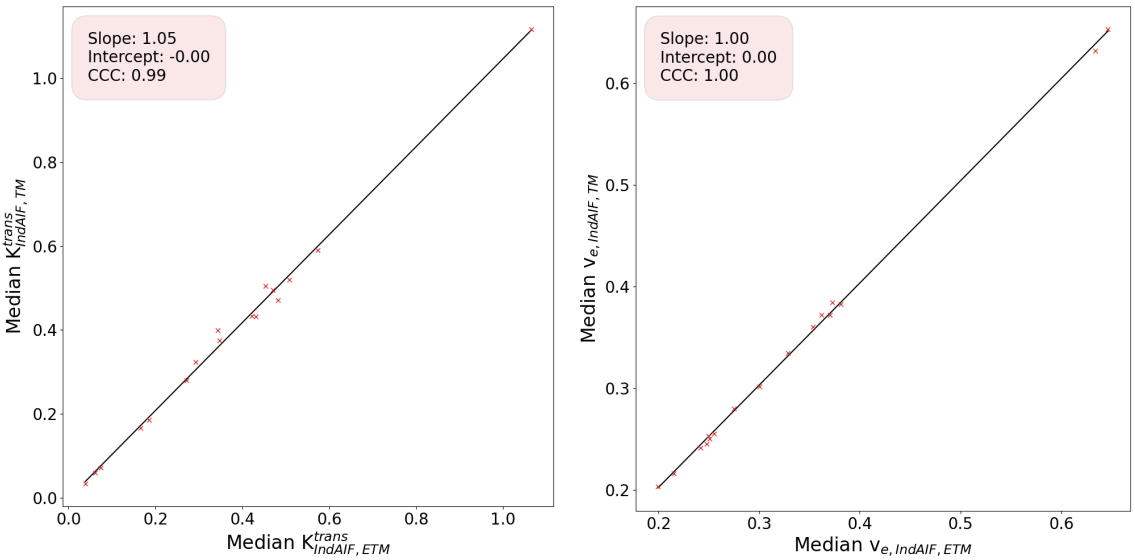

(a) (b)

Figure 29: a) The median $K^{trans}_{IndAIF,\ TM}$ were plotted against the median $K^{trans}_{IndAIF,\ ETM}$, together with the linear regression line. The slope and intercept of the regression lines are listed in the textbox, together with the CCC.

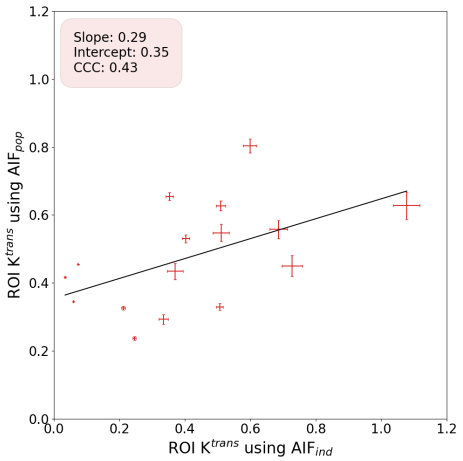

(a) AIF_{pop} vs AIF_{ind}

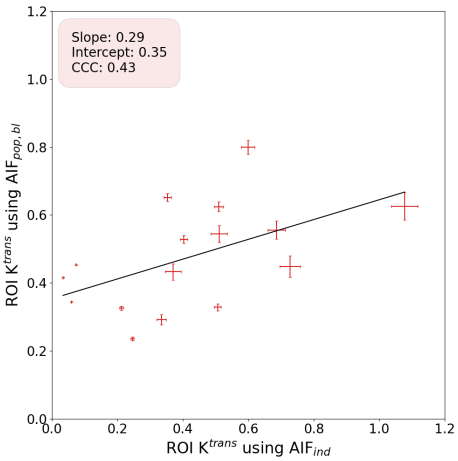

(b) $AIF_{pop,\ bl}$ vs AIF_{ind}

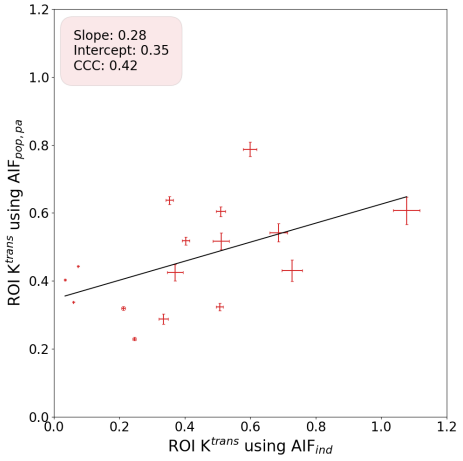

(c) $AIF_{pop,\ pa}$ vs AIF_{ind}

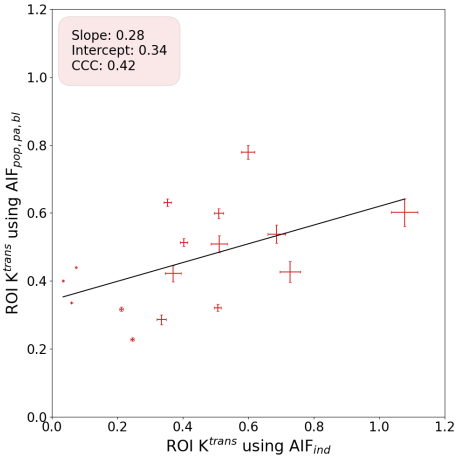

(d) $AIF_{pop,\ pa,\ bl}$ vs AIF_{ind}

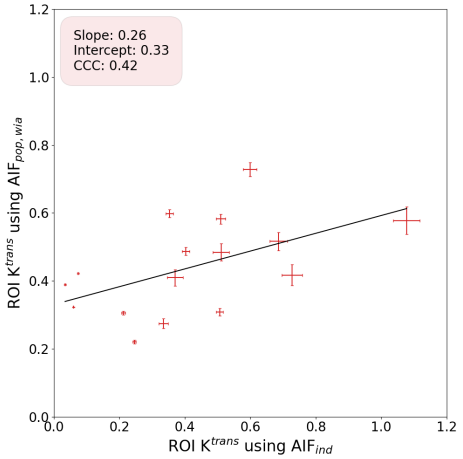

(e) $AIF_{pop,\ wia}$ vs AIF_{ind}

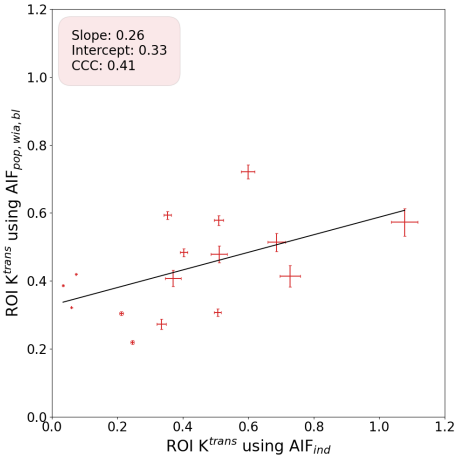

(f) $AIF_{pop,\ wia,\ bl}$ vs AIF_{ind}

Figure 30: The Tofts model was applied to the mean region of interest (ROI) time-concentration curve for each of the 16 cancerous lymph nodes using the individual arterial input function (AIF) and all six population AIFs. The resulting mean ROI K^{trans} from using a) $AIF_{pop,\ bl}$, b) AIF_{pop}, c) $AIF_{pop,\ pa,\ bl}$, d) $AIF_{pop,\ pa}$, e) $AIF_{pop,\ wia,\ bl}$ and f) $AIF_{pop,\ wia}$ were plotted with errorbars against the mean ROI K^{trans} calculated using AIF_{ind}. The linear regression line is also shown and its slope and intercept are listed in the textbox. In addition, the textbox includes the concordance correlation coefficient (CCC).

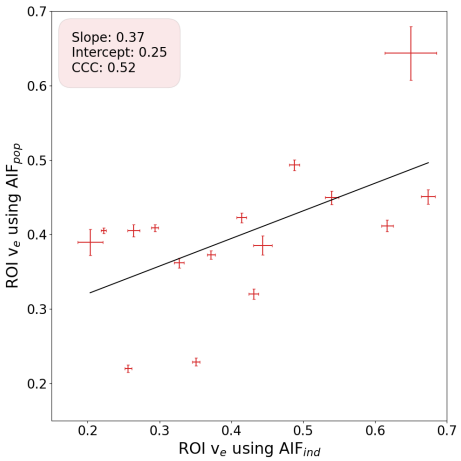

(a) AIF_{pop} vs AIF_{ind}

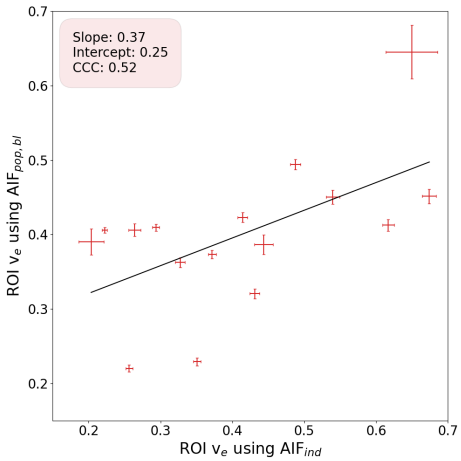

(b) $AIF_{pop,\ bl}$ vs AIF_{ind}

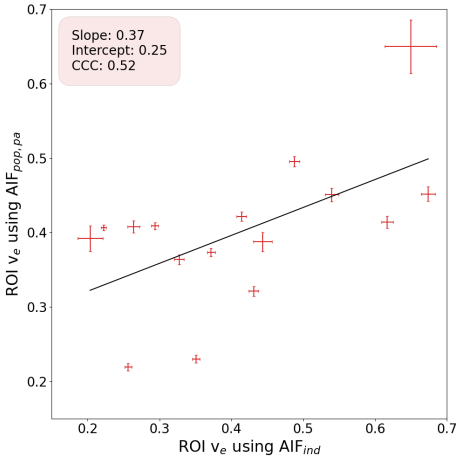

(c) $AIF_{pop,\ pa}$ vs AIF_{ind}

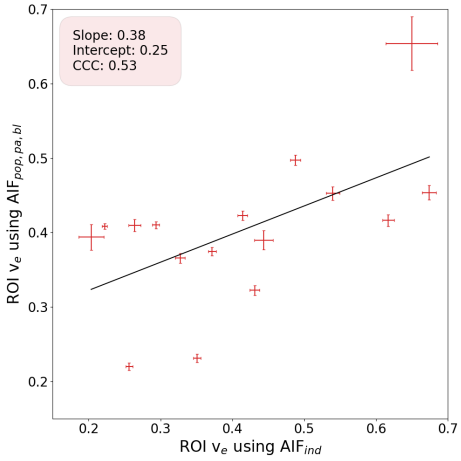

(d) $AIF_{pop,\ pa,\ bl}$ vs AIF_{ind}

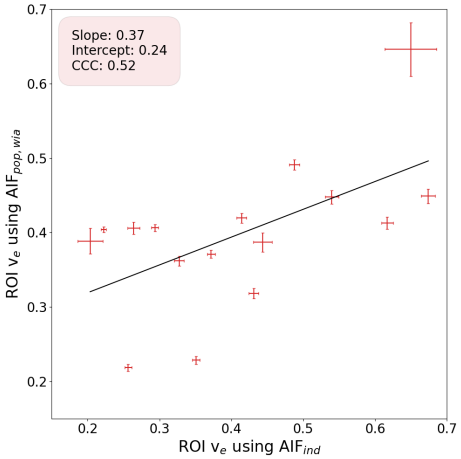

(e) $AIF_{pop,\ wia}$ vs AIF_{ind}

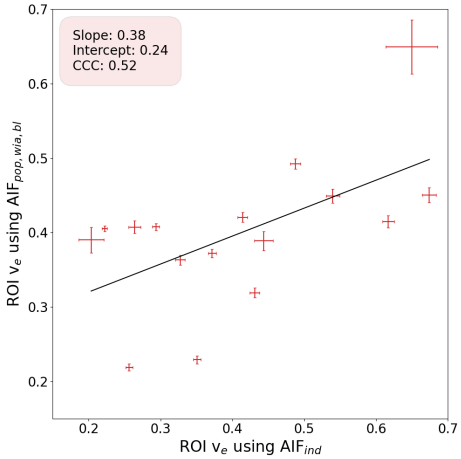

(f) $AIF_{pop,\ wia,\ bl}$ vs AIF_{ind}

Figure 31: The Tofts model was applied to the mean region of interest (ROI) time-concentration curve for each of the 16 cancerous lymph nodes using the individual arterial input function (AIF) and all six population AIFs. The resulting mean ROI v_e from using a) $AIF_{pop,\ bl}$, b) AIF_{pop}, c) $AIF_{pop,\ pa,\ bl}$, d) $AIF_{pop,\ pa}$, e) $AIF_{pop,\ wia,\ bl}$ and f) $AIF_{pop,\ wia}$ were plotted with errorbars against the mean ROI v_e calculated using AIF_{ind}. The linear regression line is also shown and its slope and intercept are listed in the textbox. In addition, the textbox includes the concordance correlation coefficient (CCC).

6.3 Correlation between pharmacokinetic parameter

Figure 32a shows a single time frame of a single slice through the lymph node of patient 1. The red region is the delineated lymph node volume. Parametric images of $K^{trans}_{IndAIF,\ TM}$, $v_{e,\ IndAIF,\ TM}$, $K^{trans}_{IndAIF,\ ETM}$, $v_{e,\ IndAIF,\ ETM}$, $K_{ep,\ IndAIF,\ TM}$, AUC60, $v_{p,\ IndAIF,\ ETM}$, $K_{ep,\ IndAIF,\ ETM}$, A, K_{el} and $K_{ep,\ Brix}$ for the lymph node volume marked in Figure 32a are presented in Figure 32b-l. Most of the parametric images had extreme values in the same regions of the lymph node.

The parametric images for all lesions were used to investigate the relationship between the different parameters from the Tofts models, extended Tofts models, Brix model and AUC calculations. Heat maps of the Pearson CCs and the corresponding p-values comparing both the median pharmacokinetic and median semi-quantitative parameters are shown in Figure 33. Similar heat maps are presented in Figure 34, though it is the pharmacokinetic and semiquantitative parameters from the model fitting to the mean TCC or mean $S(t)/S_0$, the mean ROI values, that are compared. Only the parameters from the Tofts models using AIF_{ind} were used in the comparison because the parameters from using the population AIFs deviated substantially from the parameters found using AIF_{ind}. The correlation coefficients comparing $K_{ep,\ IndAIF,\ TM}$ and K_{el}, $K_{ep,\ IndAIF,\ ETM}$ and K_{el}, $K_{ep,\ Brix}$ and A, $K^{trans}_{IndAIF,\ TM}$ and $v_{e,\ IndAIFT,\ TM}$ and $K^{trans}_{IndAIF,\ ETM}$ and $v_{e,\ IndAIFT,\ ETM}$ were high for both the ROI and median values, and the corresponding p-values were low. In contrast, none of the pharmacokinetic parameters correlated significantly with the AUCs, as shown by the heat maps in Figure 33 and 34. The heat maps also show that the AUC60, AUC90 and AUC120 correlate almost identically with the pharmacokinetic parameters.

In Figure 35, the mean ROI K_{el} and median K_{el} are plotted against the mean ROI $K_{ep,\ IndAIF,\ ETM}$ and median $K_{ep,\ IndAIF,\ ETM}$, respectively. It shows that K_{el} increases together with $K_{ep,\ IndAIF,\ ETM}$, which agrees well with the positive Pearson CC of 0.77 and 0.7 for the mean ROI and median values, respectively. The correlation comparing mean ROI $K_{ep,\ Brix}$ and median $K_{ep,\ Brix}$ with the corresponding A is 0.96 and 0.93, respectively, which agrees well with the plot of $K_{ep,\ Brix}$ against A in Figure 36.

The two parameters, K^{trans} and v_e, produced by the Tofts and extended Tofts model are also correlated. Figure 37 shows the ROI and median $K^{trans}_{IndAIF,\ TM}$ plotted against the ROI and median $v_{e,\ IndAIF,\ TM}$, respectively. The plots show that $v_{e,\ IndAIF,\ TM}$ increases with $K^{trans}_{IndAIF,\ TM}$, resulting in a positive correlation of 0.71 and 0.83 for the ROI and median values, respectively.

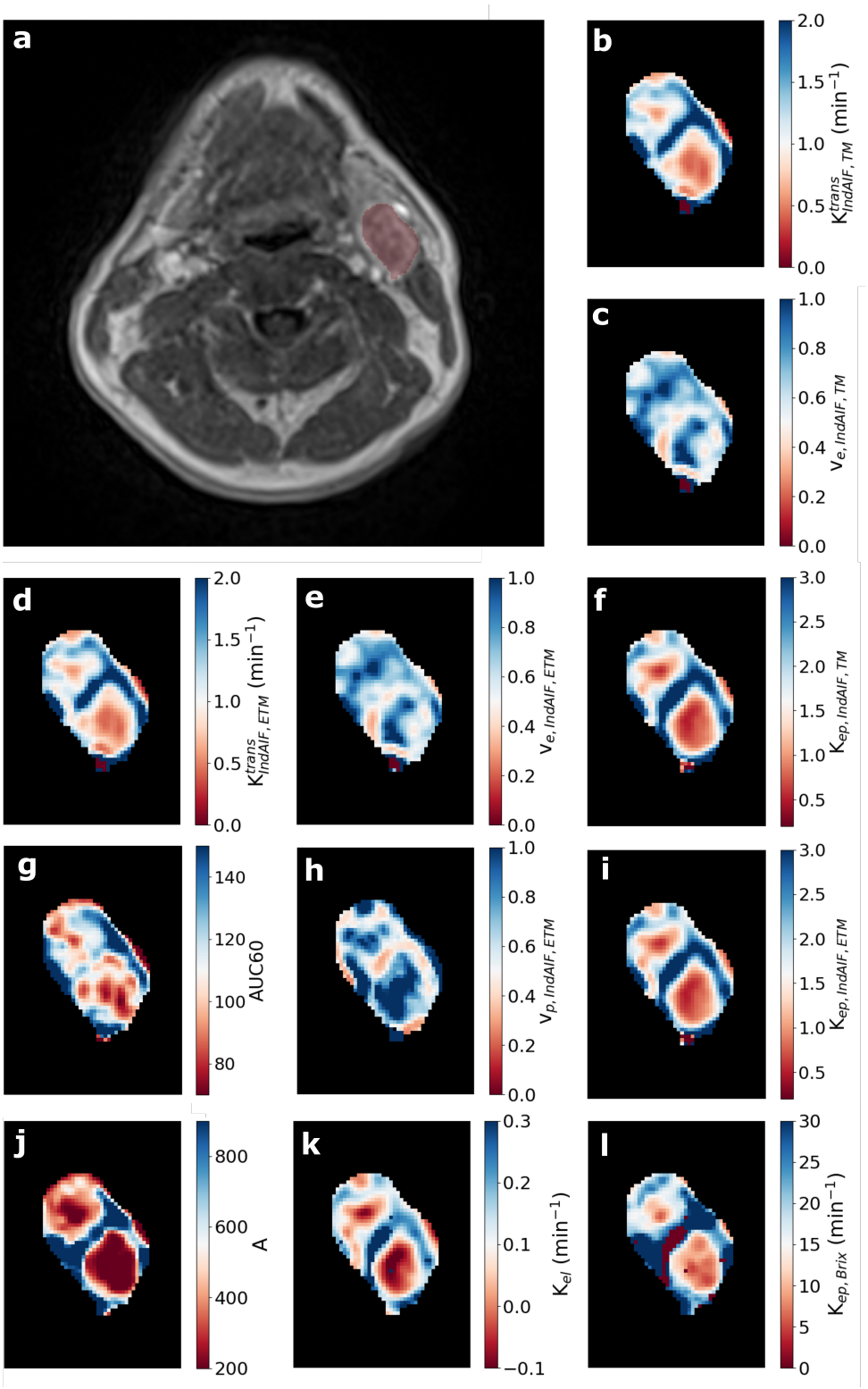

Figure 32: a) Dynamic contrast-enhanced magnetic resonance image for a single time frame and slice. The delineated malignant lymph node volume is represented by the red region. Parametric images of b) $K^{trans}_{IndAIF,\ TM}$, c) $v_{e,\ IndAIF,\ TM}$, d) $K^{trans}_{IndAIF,\ ETM}$, e) $v_{e,\ IndAIF,\ ETM}$, f) $K_{ep,\ IndAIF,\ TM}$, g) AUC60, h) $v_{p,\ IndAIF,\ ETM}$, i) $K_{ep,\ IndAIF,\ ETM}$, j) A, k) K_{el} and l) $K_{ep,\ Brix}$ for the lymph node volume are presented.

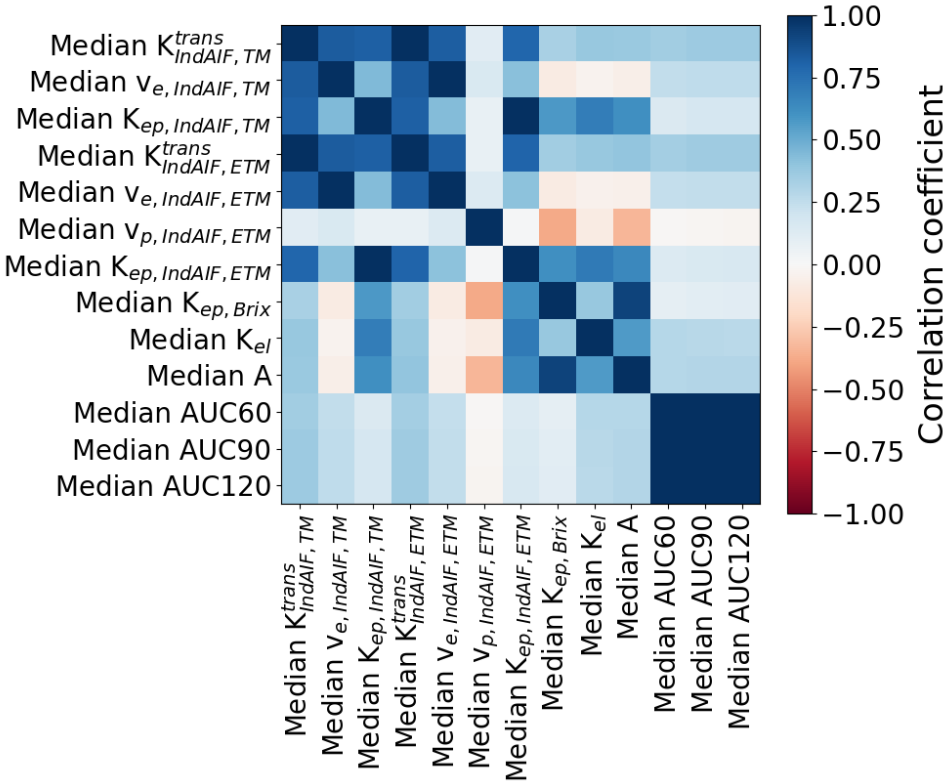

(a) Pearson correlation coefficients

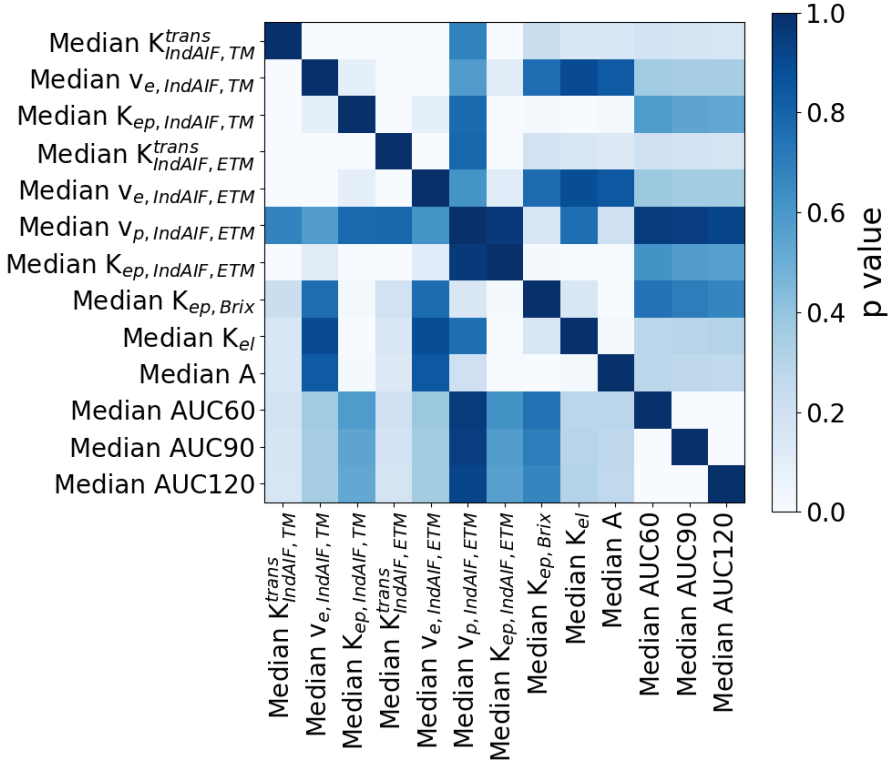

(b) P-values

Figure 33: Heat map of the a) correlation coefficients comparing both the median pharmacokinetic parameters and semiquantitative parameters over the voxels in the lymph nodes. The model fitting of the enhancement curves were done for each voxel in the lymph nodes before the median value for each lymph node was found. The corresponding b) p-values are also presented with a heat map.

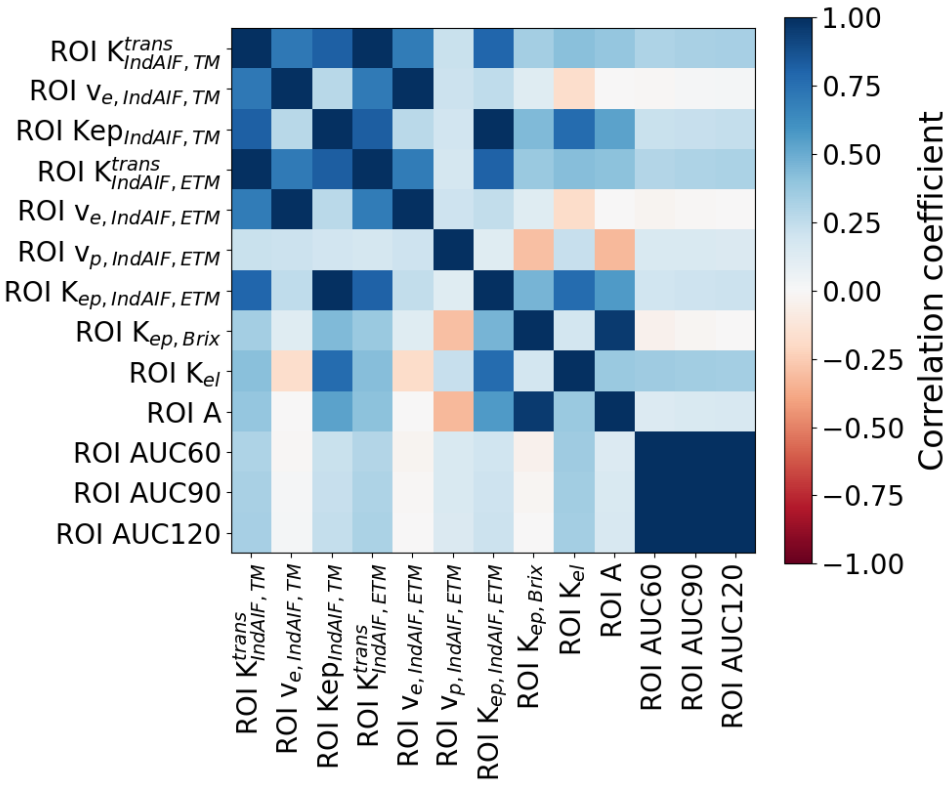

(a) Pearson correlation coefficients

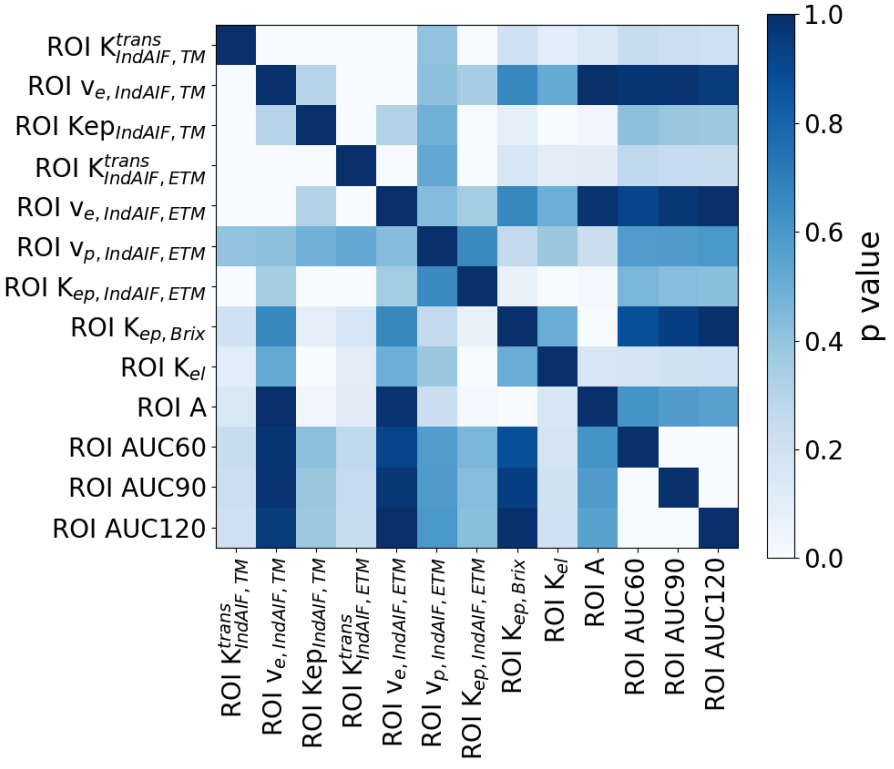

(b) P-values

Figure 34: Heat map of the a) correlation coefficients comparing both the pharmacokinetic parameters and semiquantitative parameters obtained from fitting the models to the mean region of interest (ROI) enhancement curves for the lymph nodes. The corresponding b) p-values are also presented with a heat map.

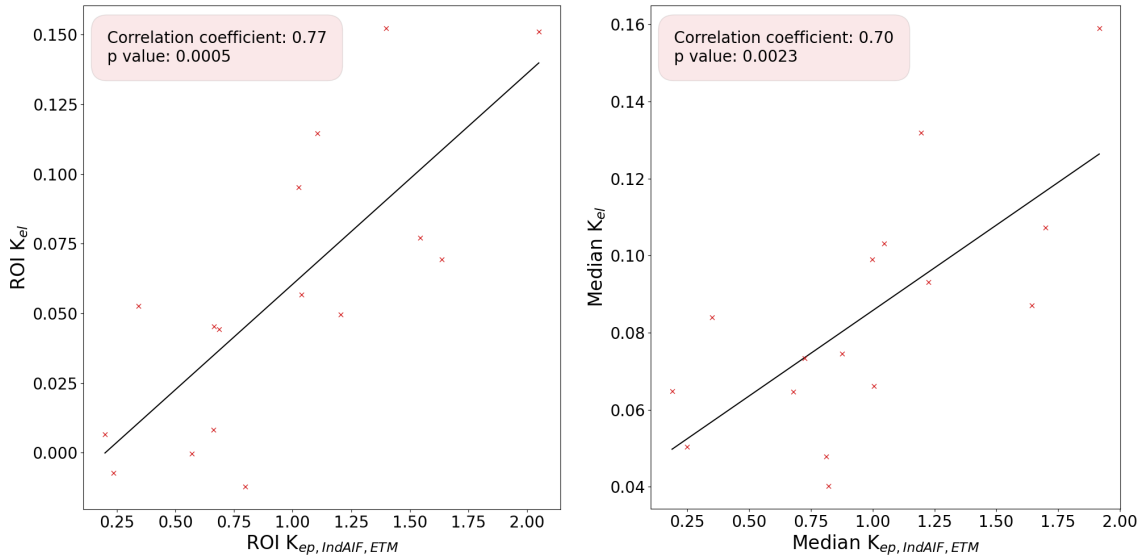

(a) (b)

Figure 35: a) The mean region of interest (ROI) and b) median K_{el} from the Brix model were plotted against the mean ROI and median $K_{ep,\ IndAIF,\ ETM}$ from the extended Tofts model, respectively. Linear regression was applied to the pairs of observations and the resulting regression lines were also plotted.

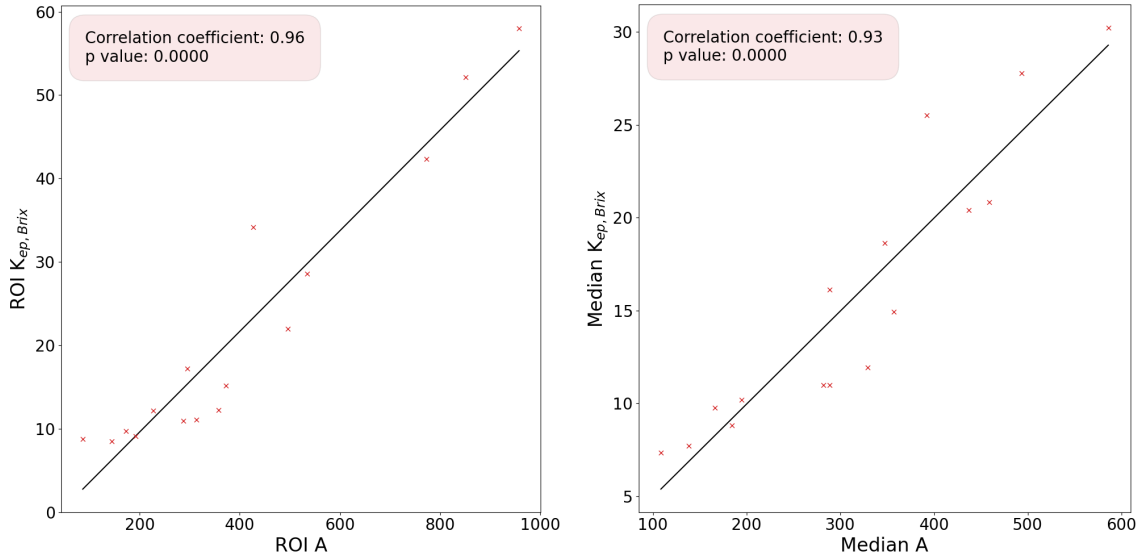

(a) (b)

Figure 36: a) The mean region of interest (ROI) and b) median $K_{ep,\ Brix}$ were plotted against the mean ROI and median A, respectively. Linear regression was applied to the pairs of observations and the resulting regression lines were also plotted.

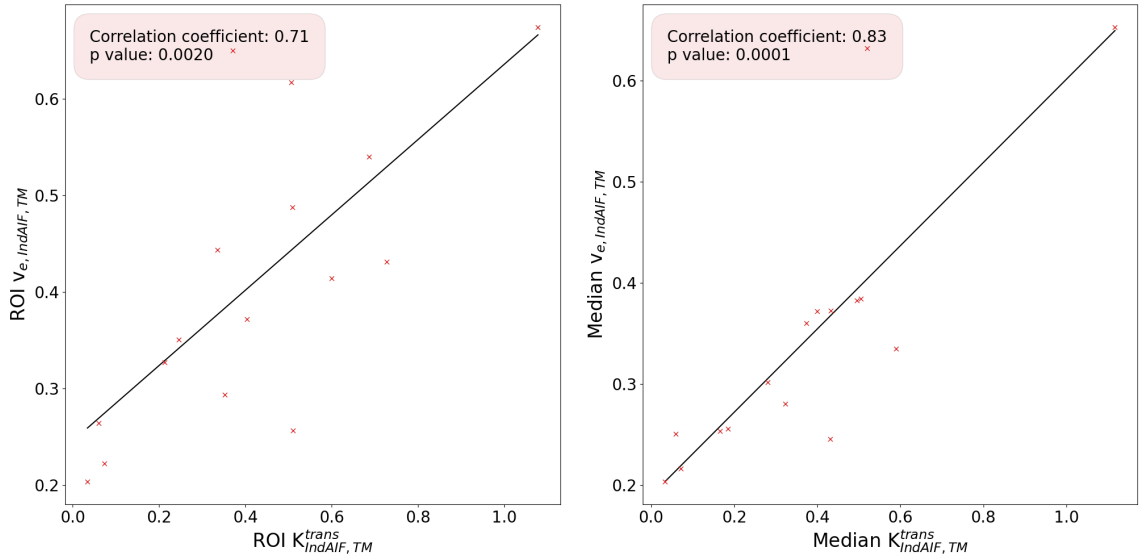

(a) (b)

Figure 37: a) The mean region of interest (ROI) and b) median $K_{ep,\,Brix}$ were plotted against the mean ROI and median A, respectively. Linear regression was applied to the pairs of observations and the resulting regression lines were also plotted.

7 Discussion

7.1 Population AIF

There are patient cases where it is difficult to obtain an AIF, either because there are no arteries in the field of view or there are artefacts from patient motion or blood flow present in the images [9]. Several studies have performed DCE-MRI analysis using a population AIF to investigate the potential of applying a population AIF instead of an individual AIF for the model fitting [9, 28, 37]. Another advantage of applying a population AIF is that it would not be essential to use a DCE-MRI acquisition method with a high temporal resolution. The CA kinetics of the tissue is much slower than blood CA kinetics, and thus the tumour signal enhancement curve can be obtained with a lower temporal resolution compared to the resolution required to obtain an accurate AIF [29]. Without the need to obtain an individual AIF, the temporal resolution can be lowered and the spatial resolution can be increased.

In this work, the population AIF was derived using different methods, resulting in six different population AIFs: AIF_{pop}, $AIF_{pop,\,bl}$, $AIF_{pop,\,pa}$, $AIF_{pop,\,pa,\,bl}$, $AIF_{pop,\,wia}$, $AIF_{pop,\,wia,\,bl}$. The parameters that describe the functional form of the population AIFs are listed in Table 3, together with the parameters for the population AIF proposed by Parker *et. al.* which is a commonly used population AIF [9]. The parameters for each of the population AIFs are of the same order of magnitude as the corresponding parameters that describe AIF_{Parker}, except the s-value for $AIF_{pop,\,pa}$. $AIF_{pop,\,pa}$ has a high s-value of 124 min^{-1} compared to $AIF_{pop,\,pa,\,bl}$ with an s-value of 40 min^{-1}. The s-value represents the width of the sigmoid. A large s-value result in a sigmoid curve with a sharp "S"-shaped curve and thus small width. Hence, the large s-value of $AIF_{pop,\,pa}$ may be the reason why the dip after the first-pass peak is larger compared to the dip of the $AIF_{pop,\,pa,\,bl}$, as seen in

Figure 28. Although all the parameters, except one, have the same order of magnitude, some parameters differ significantly between the population AIFs. The T_1 and T_2-values are largest for $AIF_{pop,\ bl}$, $AIF_{pop,\ pa,\ bl}$ and $AIF_{pop,\ wia,\ bl}$. This is expected because these population AIFs have the baseline included, and thus the centre of the Gaussians, which is represented by T_1 and T_2, occur at a later time. The same argument applies to the centre of the sigmoid which explains the high τ-value for $AIF_{pop,\ bl}$, $AIF_{pop,\ pa,\ bl}$ and $AIF_{pop,\ wia,\ bl}$.

7.1.1 Robustness of population AIF

Similar to Parker *et. al.* [9] and Li *et. al.* [29], $AIF_{pop,\ pa}$ and $AIF_{pop,\ pa,\ bl}$ were obtained by aligning the peaks of the patients' arterial time-intensity curves before taking the mean and converting the signal to CA concentration. This is the most common approach for calculating the population AIF. However, to investigate the robustness of the population AIF, the patient's arterial time-intensity curves were also not aligned and aligned using the start of wash-in as the alignment criteria. Further, two population AIFs were obtained for each alignment technique: one with and one without the baseline included. Figure 28 shows that there are some deviations between the population AIFs. $AIF_{pop,\ pa}$ and $AIF_{pop,\ pa,\ bl}$ have the highest peaks as expected because the peaks were aligned. The characteristics of the AIF, such as the peak, are believed to be essential for the DCE-MRI quantification to be reliable [38]. Thus, the alignment of the peaks may be the superior method for obtaining the population AIF.

Although there were some deviations between the population AIFs, Figure 30 and 31 show that the deviations were not large enough to have a significant effect on the K^{trans} and v_e that were found using the Tofts model on the mean ROI enhancement curves for the lymph nodes. This suggests that the choice of population AIF was not vital and thus the robustness of the population AIF was high. However, the population AIF does not take interpatient variability into account. Patient specifics such as the heart rate and kidney function lead to differences in the true AIF between patients, and hence the population AIF may not be representative for all patients. Figure 27 shows that individual AIFs for four of the patients were substantially different from the population AIFs. The same patients also exhibited low baseline values, presented in Table 2, that were used to convert the MR signal to CA concentration and thus may be the explanation behind the large deviations from the population AIF. The large deviations could also be due to errors in the MRI signal which would have been enhanced when the signal was converted to concentration [8], though this is unlikely since no abnormalities in the images were observed.

7.1.2 Comparison between population AIF and individual AIF

The pharmacokinetic parameters that were found using the population AIFs were compared to the corresponding values found using the patients' individual AIFs. Although the individual AIF for just four of the patients deviated largely from the population AIF, few of the pharmacokinetic parameters that were found using the population AIF agreed with the corresponding values obtained using the individual AIFs. This can be observed in Figure 30 and 31 where the regression lines do not follow the 45° line and the CCC is low for all the population AIFs. Thus, the population AIF should be avoided if possible. This is easier for some cancer types, such as head and neck cancer, compared to other cancer types because they are more likely to have an artery in the field of view. Since

the individual AIF is preferred over the population AIF, more research into increasing the robustness of the individual AIF extraction should be done. To minimize inter-observer variability and increase the repeatability of the AIF, semi-automatic and automatic AIF extraction have been proposed by several studies [37, 27]. An extensive study comparing different methods for extracting the individual AIF for head and neck cancer should be conducted to better understand which is the preferred method. This could also lead to an AIF extraction method that could become the gold standard in DCE-MRI analysis, making it easier to compare different studies.

Visual inspection of Figure 30 and 31 also indicate that v_e is closest to the 45° line and thus has the highest CCC. This agrees well with the study by Shukla-Dave *et. al.* which showed that the difference between ROI v_e values is larger than the difference between the mean ROI K^{trans} values found using the population AIF and the individual AIF [28]. In contrast, the results from Li *et. al.* showed that the mean ROI v_e deviates the most from the 45° line [29]. Both Li *et. al.* and Shukla-Dave *et. al.* also investigated the correlation between the pharmacokinetic parameters found using the population AIF and the corresponding parameters obtained with the individual AIF on a voxel-by-voxel-basis [29, 28]. This could be done for this study as well, as part of future work, to see if the correlation between the results from the population AIF and individual AIF changes compared to the mean ROI analysis.

7.2 Limitations of the Tofts and extended Tofts model

The Tofts models could not be fitted to the enhancement curves for all voxels, suggesting that the models were not valid in those regions. Several assumptions were made to construct the Tofts models. The models assume that the parameters that describe the compartments are constant during the acquisition time [6]. In most cases, this is a valid assumption. However, acute hypoxia is more frequently present in tumours than in normal tissues. Acute hypoxia can be due to sudden blockage of blood vessels and sometimes lasts only for a few minutes. Thus, the sudden change in the vasculature in tumours can make the model fitting difficult.

The models also assume that the CA distribution in the compartments is homogeneous, and thus CA diffusion within the compartments is neglected. This assumption makes it possible to calculate the tracer concentration by using the linear relationship between concentration and change in longitudinal relaxation which is expressed by Equation (22) [39]. This assumption is not valid for tumour tissues that are necrotic [40]. Schimpf *et. al.* investigated the validity of the extended Tofts model for partly necrotic tumours, and they found that the model overestimated the volume fraction of the extravascular extracellular space [40]. In a voxel-by-voxel analysis, the models will not be invalid for all voxels, just the voxels with necrosis. Thus, the models can still be used to calculate the pharmacokinetic parameters for the malignant lymph nodes and regions with invalid parameter values may suggest necrosis. For the mean ROI analysis, the signal is averaged across all the voxels in the lymph node. Lymph nodes with a high degree of necrosis may result in a mean enhancement curve that makes model fitting difficult and the parameters may not be valid. Thus, leading to inaccurate conclusions. As part of future work, the effect of necrosis on pharmacokinetic analysis should be investigated.

The two-compartment exchange model (2CXM) is a generalization of the Tofts models and can be applied to all tissue types. Sourbron and Buckley identified which tissue types the Tofts model and the extended Tofts model are valid for [25]. 2CXM produces the same

results as the Tofts and extended Tofts model in weakly vascularized tissues where $v_p = 0$. For intermediate or highly vascularized tissues, the extended Tofts model may be applied but only in tissues with high perfusion. Tumours are heterogeneous and thus contain regions with high vascularization and other regions with poor vascularization. The state of the tissue is usually not known *a priori*, making it difficult to say with certainty that the Tofts models are valid.

For some regimes, e.g. highly vascularized tissues, the Tofts models provide a fitted curve that closely matches the data, even though the models are not valid under these conditions. In these cases, it is often a problem of interpretation. Sourbron and Buckley provided an example for highly vascularized tissues where the K^{trans}-value found by the Tofts models was close to the flow of plasma into the capillary bed, F_p [25]. The expression for the K^{trans} also contains a parameter that represents the permeability of the blood vessel. Thus, the K^{trans}-value provided by the Tofts models for highly vascularized tissue was misinterpreted to include the permeability. The good fitness of the curves does not indicate that the results are misinterpreted. This is a significant limitation of the Tofts models.

Immunohistochemistry analysis of the tissue can provide information about the characteristics of the blood vessels. Such an analysis could have made it possible to determine if the models were valid and the parameters were interpreted correctly. Bakke *et. al.* performed an immunohistochemistry analysis to obtain data on microvessel density and blood vessel size, in addition to pharmacokinetic parameters from the DCE-MRI analysis [41]. They showed that the correlation between the pharmacokinetic parameters varied extensively between tumours with low and high blood flow. Thus, the correlation between the parameters could be used as an indicator of the state of the tissue to avoid immunohistochemistry analysis. The patients in the study had rectal cancer. It should be confirmed that the correlation applies to blood flow for head and neck cancer, as well, before it is used to indicate the state of the tissue.

7.3 Tofts vs extended Tofts model

The CCC comparing median $K^{trans}_{IndAIF,\ TM}$ and $K^{trans}_{IndAIF,\ ETM}$, and median $v_{e,\ IndAIF,\ TM}$ and $v_{e,\ IndAIF,\ ETM}$ were 0.99 and 1.00, respectively. This suggests that the Tofts model and extended Tofts model produce similar results, which can also be observed in Figure 29. Figure 32 also shows that the parametric maps of K^{trans} and v_e obtained using the Tofts and extended Tofts models are similar. If the tissue is weakly vascularised, then the extended Tofts model is reduced to the Tofts model, and it is expected that the two models produce the same K^{trans} and v_e values [25]. However, the v_p values found by the extended Tofts model are not close to zero, suggesting that the tissue is not weakly vascularised. If that is the case, there is a possibility that the parameters will be misinterpreted. Some of the v_p values did also take on unphysical values outside the range from zero to one. By adding more free parameters to the model, more data points are needed to estimate the parameters. Therefore, it is more likely that the parameters obtained by the extended Tofts model converge to unrealistic values due to the shortcomings of the nonlinear least-squares fitting algorithm, compared to the Tofts model. If the fitting algorithm is not able to correctly determine the v_p, the tissue may still be weakly vascularised.

7.4 Correlation between both AUCs and pharmacokinetic parameters

The heat maps of the correlation matrices comparing the different pharmacokinetic parameters, as well as the AUCs, are shown in Figure 34a and 33a. The Pearson CCs in Figure 34a have been found using the parameters calculated from the average enhancement curves of each lymph node, while the Pearson CCs in Figure 33a are based on the median values found for each lymph node. Both figures show similar Pearson CCs for all of the parameters. As already discussed, the K^{trans}, v_e and K_{ep} values obtained with the Tofts model are highly correlated with the corresponding values found by the extended Tofts model. This was expected because the two models are similar, and the parameters found by the Tofts model and the corresponding ones that are produced by the extended Tofts model are supposed to describe the same characteristics of the two-compartment model.

The K^{trans} is also highly correlated with the v_e which is shown more clearly in Figure 37. As K^{trans} increases, so does the v_e values. The K^{trans} represents the blood flow into the EES, and thus also reflects the oxygen supply to the tumour. Gaustad *et. al.* found that K^{trans} correlates with the hypoxic fraction of the tumour; low K^{trans} is associated with a high hypoxic fraction [42]. The hypoxic fraction refers to the fraction of cells with low oxygen concentration in the tumour. It has also been shown that tumours with a high fraction of hypoxic cells also have low v_e. This can be explained by noting that tumours with low v_e have a high cell density and oxygen consumption, which leads to low oxygen tension and a high hypoxic fraction [43]. Since both K^{trans} and v_e are inversely proportional to the hypoxic fraction, it is expected that the correlation of K^{trans} with v_e is positive. The correlation between K^{trans} and v_e could also be the result of the two variables being part of the same model and are thus related through Equation (10). For example, if the CA concentration curves for the plasma space and EES are approximately similar then an increase in K^{trans} would lead to an increase in v_e as seen in Figure 37.

The parameters K_{ep} and A from the Brix model are also correlated with a high positive Pearson CC of 0.96 and 0.93 for the mean ROI and median values, respectively. Again, this correlation could occur due to the parameters being related through Equation (20). However, it is not obvious from Equation (20) that an increase in A would lead to an increase in K_{ep}, even if the concentration curves stay constant. The K_{ep} represents the flux of CA into the plasma space from the EES and depends on different vascular properties, such as the blood perfusion, the permeability of the blood vessels and the vessel density [44]. A on the other hand is a scaling factor and does not have an intuitive physiological meaning. However, A is affected by several physiological properties, e.g. the size of the EES, the blood vessel permeability and blood perfusion [44]. Hence, both K_{ep} and A are dependent on some of the same vascular properties which could explain why they are correlated. To my knowledge, there are no studies that present the correlation between the Brix parameters.

The most interesting correlation was between K_{el} from the Brix model and K_{ep} from both Tofts models. Figure 35 shows that K_{el} increases with $K_{ep,\,\mathrm{IndAIF},\,\mathrm{ETM}}$, which is also true for $K_{ep,\,\mathrm{IndAIF},\,\mathrm{TM}}$. The flux of CA from the EES to the plasma space is represented by K_{ep}. The elimination rate, K_{el} represents the rate at which the CA is eliminated from the plasma space. An increase in K_{ep} would lead to a higher concentration of CA in the plasma space, and thus the CA can leave the plasma space at a higher rate. To my knowledge, no studies on the correlation comparing K_{el} from the Brix model and K_{ep} from the Tofts models have been conducted. Most studies perform correlation analysis

to compare pharmacokinetic parameters with prognostic factors instead of comparing the different models.

The Tofts models and Brix model have their advantages and disadvantages. The Brix model does not need an AIF or require the signal to be converted to concentration using T_1-maps, as opposed to the Tofts models. The accuracy of the AIF greatly affects the accuracy of the pharmacokinetic parameters obtained by the Tofts models. The AIF can also be obtained using several methods, e.g. population AIF or individual AIF. The Brix model could be more robust because it is less influenced by AIF variations and their accuracy [45]. Further, errors in the T_1 map leads to additional errors in the concentration calculations which again leads to errors in the pharmacokinetic parameters [46]. This is another reason why the Brix model may be more robust compared to the Tofts model. However, the Brix model does not calculate K^{trans} which is thought of as a significant limitation because K^{trans} has been shown to exhibit great prognostic value [10].

The p-values associated with the high Pearson CCs comparing K^{trans} with v_e, K_{ep} with A and K_{el} with K_{ep} from the Tofts models were low. The p-value is the probability that the current corresponding Pearson CC would have been found if the Pearson CC in reality was zero [47]. Thus, low p-values are desired because they tell us that the Pearson CCs are significant results.

An unexpected result was the low correlation between the pharmacokinetic parameters found by Tofts and the AUCs. Walker-Samuel *et. al.* studied the relationship between the AUC60 and the parameters K^{trans}, v_e and v_p by performing simulations of DCE-MRI data [48]. They showed that the AUC is dependent on all three parameters, but can be directly correlated to K^{trans} or v_e under certain conditions. For example, for large K^{trans} and small v_e AUC is proportional to v_e, while AUC is proportional to K^{trans} when K^{trans} is small and v_e is larger. This held for all types of AUC, though how large or small K^{trans} and v_e had to be depended on the type of AUC. Figure 34 and 33 show low correlation between the AUC and the parameters K^{trans} and v_e. One of the reasons there is a low correlation could be that the conditions for the K^{trans} and v_e were not fulfilled. Although, the study by Walker-Samuel *et. al.* were based on simulations and may not apply to *in vivo* DCE-MRI measurements, there is a study that shows a correlation between the AUC60 and K^{trans} for abdominal cancer and glioma tumours in the brain [49]. The correlation between K^{trans} and AUCs could be cancer-specific and may not exist for head and neck squamous cell carcinoma, which was used in our study, though it exists for other cancer types. Also, the AUC does not have a clear physiological meaning but is influenced by several physiological factors such as the blood flow, vessel permeability and interstitial space [38]. Hence, it is not obvious that AUC should have a linear correlation with the pharmacokinetic parameters.

The AUC60, AUC90 and AUC120 correlate almost identically with the pharmacokinetic parameters. The AUC60, AUC90 and AUC120 are almost perfectly correlated with a Pearson CC close to one, which can be observed in the heat maps in Figure 33 and 34. This means that they differ by a certain factor, meaning AUC90 or AUC120 can be obtained by multiplying AUC60 by a certain factor. The Pearson CC is unaffected by linear transformations, i.e. the CC does not change if the parameters are multiplied by a constant and/or a constant is added to the parameter. Thus, the almost perfect correlation between the AUC60, AUC90 and AUC120 could explain why they exhibit almost identical correlations with the pharmacokinetic parameters.

The difficulty of relating semi-quantitative parameters, e.g. AUC, directly to underlying

physiology is one of the main disadvantages of semi-quantitative analysis. The main advantage, on the other hand, is that it is less complicated and prone to errors [50]. Hence, the semi-quantitative parameters are often more robust compared to pharmacokinetic parameters. A semi-quantitative analysis is also less time-consuming because fewer and simpler numerical calculations are required [50]. Therefore, it would be beneficial to use semi-quantitative parameters if possible. There are studies where semi-quantitative parameters have been used to identify cancer and differentiate between benign and malignant cancer [50]. In addition, semi-quantitative parameters can also be used as a prognostic factor [51, 52]. However, the pharmacokinetic parameters describe the vasculature of the tumour better, e.g. hypoxia, and thus could be better suited to be biomarkers used to individualise treatment.

The models were fitted to the TCC for each voxel in the lesions and then the median values of the resulting pharmacokinetic parameters were calculated for each lesion. The median values of the pharmacokinetic parameters were then used to calculate the Pearson CCs comparing the different parameters. In addition, the mean TCC for each lymph node ROI was found and then the models were fitted to the mean TCC for each lymph node. The Pearson CCs were also calculated using these mean ROI values. The Pearson CCs obtained using the median and mean ROI values were similar. This is expected because both the median and mean ROI values represent the vasculature of the whole tumour. A drawback with such an analysis is that it does not capture the heterogeneity of the lymph nodes and valuable information could be lost [53]. A voxel-by-voxel analysis, on the other hand, can capture the heterogeneity of the lymph node. The parameters most likely correlate on the voxel level as well because several of the parametric maps in Figure 32 show the same pattern. The Pearson correlation between parameters obtained with a voxel-by-voxel analysis should be calculated as part of further work to see if the correlations still hold. It is possible that the correlation will be different for different patients and could give further information about each individual.

7.5 Clinical aspects

As discussed previously, the Tofts models are not valid for necrotic tumour tissues. The presence of necrosis is associated with poorer overall survival and recurrence-free survival for cancer patients which was supported by the study conducted by Ling *et. al.* [54]. The fraction of voxels with invalid parameters, e.g. volume fractions less than zero and larger than one, may be used as a measure of necrosis. This should be investigated. In future work, the correlation between patient outcome and the fraction of invalid voxel parameters should also be investigated to see if the fraction of voxels with invalid parameters can be used as a prognostic factor. Thus, turning the weakness of the model into a strength.

Many studies evaluate the prognostic value of the pharmacokinetic parameters that are obtained with DCE-MRI analysis. Tumours are biologically heterogeneous and imaging the vascular heterogeneity using DCE-MRI can be a useful tool to predict patient outcomes [55, 56]. The heterogeneity may be better represented by the distribution of pharmacokinetic parameters than by the corresponding mean and median values [57]. Shukla-Dave *et. al.* showed that the skewness of K^{trans} correlated with both the progression-free survival and overall survival and thus may play an important role in deciding the patient's prognosis [57]. Therefore, as part of future work, the correlation between the distribution of the pharmacokinetic parameters and the patient outcome should be investigated to study the prognostic value of the parameters for head and neck cancer.

Pharmacokinetic parameters can also have a predictive value and be used as an imaging biomarker for tumour treatment response [39]. As an example, K^{trans} from the Tofts models correlates with angiogenic activity and tumour aggressiveness, and hence K^{trans} has been shown to predict response to neo-adjuvant treatments, e.g. chemotherapy [58]. Another example is from the study by Halle *et. al.* which showed that the parameter, A, from the Brix model is associated with tumour aggressiveness [59]. Tumours with low A values appeared to be more aggressive. In radiotherapy, hypoxic tumours are difficult to treat because they are more resistant to radiation. Pharmacokinetic parameters describe the vasculature of the tumour and can potentially provide information about the hypoxic state of the tumour. This was confirmed by Gaustad *et. al.* who found that K^{trans} reflected hypoxia in tumours [42]. Therefore, the pharmacokinetic parameters, especially K^{trans}, have the potential of being used as predictive biomarkers in radiotherapy. Predictive biomarkers can both be used as a tool for deciding which treatment modality is the better choice, e.g. tumours with poor perfusion and hypoxia are generally radioresistant and should thus be surgically removed instead. It is also possible to use the predictive biomarkers to determine the individual dose used in radiotherapy [60].

Tumours are heterogeneous with regions of low and high radiosensitivity. A high dose should be delivered to regions with low radiosensitivity, e.g. hypoxic regions, in tumours to ensure cell killing. Today's technology in radiotherapy facilitates heterogeneous dose distribution, also called dose-painting. Thus, it is possible to deliver a dose distribution that complements the heterogeneity of the tumour if the heterogeneity is quantified. Predictive imaging biomarkers can be used to quantify tumour heterogeneity. As an example, K^{trans} is thought to reflect hypoxia and can create a map of hypoxic regions which can then be used to determine the dose distribution. However, there are several challenges associated with studying the application of biomarkers to dose-painting, as described by Gurney-Champion *et. al.* [60]. First, it is challenging to know which voxels did or did not respond to radiation and thus relate the parameters associated with the voxels to the outcome. Secondly, some regions in the tumour may get a lower dose which makes it difficult to draw conclusions from the dose-response relations. Therefore, the trial design needs to be planned carefully.

O'Connor *et. al.* suggest two translational gaps that need to be closed before imaging biomarkers can be used in the clinics [61]. The biomarkers must first show value in both experimental models and patients. Currently, most biomarkers have only been evaluated by single-centre studies with a limited number of patients and thus the first gap is still not completely closed for most biomarkers. Single-centre studies make it difficult for the parameters to demonstrate sufficient performance [60]. Further, they tend to tweak the analysis method, e.g. tweaking the post-processing method and the definition of the region of interest, in such studies which results in overestimation of the performance of the parameters. The second gap is closed when the biomarkers are fully implemented in the treatment of patients. Multi-centre studies with large statistical power are required before integrating biomarkers in patient care. Such studies are extensive and time-consuming, and thus the parameter of interest should be carefully selected. The O'Connor *et. al.* also described three types of studies that need to be performed while closing both translational gaps: technical validation, biological and clinical validation and cost-effectiveness [61]. Technical validation refers to studying whether the biomarker can be measured precisely and accurately, while biological and clinical validation refers to whether the biomarker can measure a useful biological feature or predict an outcome. It is also important to study the cost-effectiveness to show that the use of an imaging biomarker is beneficial in terms of health economics.

8 Conclusion

The results presented in this thesis show that although the population AIF is robust, it should not be used instead of individual AIF because the parameters calculated using the Tofts models with the population AIF differ substantially from the corresponding values calculated using the individual AIF. The models could not be fitted to the enhancement curves for all voxels due to the models' limitations. The Tofts models may not be valid if the tumour is necrotic and thus failed fitting could be a measure of necrosis. Further, the Tofts models are both valid for weakly vascularized tissue, though the extended Tofts model is also valid for tissues with high perfusion. The state of the tissue is usually not known *a priori* and thus it can be difficult to know with certainty that the Tofts models are valid and lead to misinterpretation of the parameters. The Tofts and extended Tofts model give similar values for K^{trans} and v_e. The v_p from the extended Tofts model are not close to zero, suggesting that the tissue is not weakly vascularized. Therefore, the parameters from the Tofts model may be misinterpreted. It could also be that the nonlinear least-squares fitting algorithm is not able to correctly determine the v_p because the model has too many free variables. Immunohistochemistry analysis of resected tumour samples could shed some light on tissue biology and help determine if the tissue is weakly vascularised.

The Pearson CCs comparing K^{trans} with v_e from the Tofts model or extended Tofts model, A with K_{ep} from the Brix model and K_{ep} from the Tofts models with K_{el} from the Brix model were high. In contrast, the correlations between the pharmacokinetic parameters found with the Tofts models and the AUCs were low for all pharmacokinetic parameters which were not supported by other studies. However, it is not obvious that the AUCs are supposed to linearly correlate with the pharmacokinetic parameters because the AUCs do not have a clear physiological meaning. The Pearson CCs were based on the mean ROI values or the median values over the voxels in the lymph nodes. The same correlation analysis should later be performed voxel-by-voxel to investigate if the correlations still hold.

Further work should also consist of investigating the correlation between necrosis and invalid pharmacokinetic parameters. In addition, the prognostic value of the pharmacokinetic parameters should be studied when the long-term patient outcome is available. Though it requires a more extensive study, the predictive values of the pharmacokinetic parameters should also be investigated. The predictive biomarkers could be used for stratification and more advanced dose escalation which would individualise treatment and may lead to better survival for head and neck cancer patients.

References

[1] Global Burden of Disease 2019 Cancer Collaboration. "Cancer Incidence, Mortality, Years of Life Lost, Years Lived With Disability, and Disability-Adjusted Life Years for 29 Cancer Groups From 2010 to 2019: A Systematic Analysis for the Global Burden of Disease Study 2019". In: *JAMA oncology* 8.3 (2022), pp. 420–444. DOI: 10.1001/jamaoncol.2021.6987.

[2] Hesham Elhalawani et al. "Dynamic contrast-enhanced magnetic resonance imaging for head and neck cancers". In: *Scientific Data* 5.1 (2018), p. 180008. DOI: 10.1038/sdata.2018.8.

[3] Yaron Gordon et al. "Dynamic contrast-enhanced magnetic resonance imaging: fundamentals and application to the evaluation of the peripheral perfusion". In: *Cardiovascular diagnosis and therapy* 4.2 (2014), pp. 147–164. DOI: 10.3978/j.issn.2223-3652.2014.03.01.

[4] Douglas Hanahan and Robert A. Weinberg. "Hallmarks of Cancer: The Next Generation". In: *Cell* 144.5 (2011), pp. 646–674. DOI: 10.1016/j.cell.2011.02.013.

[5] Richard A. Popple, Roger Ove, and Sui Shen. "Tumor control probability for selective boosting of hypoxic subvolumes, including the effect of reoxygenation". In: *International Journal of Radiation Oncology - Biology - Physics* 54.3 (2002), pp. 921–927. DOI: 10.1016/S0360-3016(02)03007-9.

[6] Paul S. Tofts. *Modeling Tracer Kinetics in Dynamic GdlDTPA MR Imaging*. 1997. DOI: 10.1002/jmri.1880070113.

[7] Gunnar Brix G et al. "Pharmacokinetic parameters in CNS Gd-DTPA enhanced MR imaging". In: *Journal of computed assisted tomography* 15.4 (1991), pp. 621–628. DOI: 10.1097/00004728-199107000-00018.

[8] Harrison Kim. "Modification of population based arterial input function to incorporate individual variation". In: *Magnetic resonance imaging* 45 (2018), pp. 44–71. DOI: 10.1016/j.mri.2017.09.010.

[9] Geoff J.M. Parker et al. "Experimentally-derived functional form for a population-averaged high-temporal-resolution arterial input function for dynamic contrast-enhanced MRI". In: *Magnetic Resonance in Medicine* 56 (5 2006), pp. 993–1000. DOI: 10.1002/mrm.21066.

[10] Toru Chikui et al. "The Principal of Dynamic Contrast Enhanced MRI, the Method of Pharmacokinetic Analysis, and Its Application in the Head and Neck Region". In: *International Journal of Dentistry* (2012). DOI: 10.1155/2012/480659.

[11] Tanja Gaa et al. "Comparison of perfusion models for quantitative T1 weighted DCE-MRI of rectal cancer". In: *Scientific Reports* 7.1 (2017), p. 12036. DOI: 10.1038/s41598-017-12194-w.

[12] Alexander R. Haug et al. "A Comparative Study of Two-Compartment Exchange Models for Dynamic Contrast-Enhanced MRI in Characterizing Uterine Cervical Carcinoma". In: *Contrast Media & Molecular Imaging* 2019 (2019), p. 3168416. DOI: 10.1155/2019/3168416.

[13] Geoffrey M Cooper. "Cancer". In: *The Cell: A Molecular Approach*. Sinauer Associated, 2000. Chap. 15.

[14] Freddie Bray et al. "Global cancer statistics 2018: GLOBOCAN estimates of incidence and mortality worldwide for 36 cancers in 185 countries". In: *CA: A Cancer Journal for Clinicians* 68.6 (2018), pp. 394–424. DOI: 10.3322/caac.21492.

[15] Laura Q.M. Chow. "Head and Neck Cancer". In: *New England Journal of Medicine* 382.1 (2020), pp. 60–72. DOI: 10.1056/NEJMra1715715.

[16] K. Kian Ang et al. "Human Papillomavirus and Survival of Patients with Oropharyngeal Cancer". In: *New England Journal of Medicine* 363.1 (2010), pp. 24–35. DOI: 10.1056/NEJMoa0912217.

[17] Carole Fakhry et al. "Improved Survival of Patients With Human Papillomavirus–Positive Head and Neck Squamous Cell Carcinoma in a Prospective Clinical Trial". In: *Journal of the National Cancer Institute* 100.4 (2008), 261–269. DOI: 10.1093/jnci/djn011.

[18] Dietmar W. Siemann. "The unique characteristics of tumor vasculature and preclinical evidence for its selective disruption by Tumor-Vascular Disrupting Agents". In: *Cancer Treatment Reviews* 37.1 (2011), pp. 63–74. DOI: 10.1016/j.ctrv.2010.05.001.

[19] August Krogh. "The supply of oxygen to the tissues and the regulation of the capillary circulation". In: *The Journal of Physiology* 52.6 (1919), pp. 457–474. DOI: 10.1113/jphysiol.1919.sp001844.

[20] Kaitlin Graham and Evan Unger. "Overcoming tumor hypoxia as a barrier to radiotherapy, chemotherapy and immunotherapy in cancer treatment". In: *International journal of nanomedicine* 13 (2018), pp. 6049–6058. DOI: 10.2147/IJN.S140462.

[21] Baris Türkbey et al. "The role of dynamic contrast-enhanced MRI in cancer diagnosis and treatment". In: *Diagnostic and interventional radiology* 16.3 (), pp. 186–192. DOI: 10.4261/1305-3825.DIR.2537-08.1.

[22] Westbrook Catherine and Talbot John. *MRI in Practice.* Vol. Fifth edition. Wiley-Blackwell, 2019. ISBN: 9781119391968. URL: https://search.ebscohost.com/login.aspx?direct=true&db=nlebk&AN=1863403&site=ehost-live.

[23] Yu-Dong Xiao et al. "MRI contrast agents: Classification and application". In: *International Journal of Molecular Medicine* 38.5 (2016), pp. 1319–1326. DOI: 10.3892/ijmm.2016.2744.

[24] Doenja M.J. Lambregts et al. "Magnetic Resonance Imaging and Other Imaging Modalities in Diagnostic and Tumor Response Evaluation". In: *Seminars in Radiation Oncology* 26.3 (2016), pp. 193–198. DOI: 10.1016/j.semradonc.2016.02.001.

[25] Steven P. Sourbron and David L. Buckley. "On the scope and interpretation of the Tofts models for DCE-MRI". In: *Magnetic Resonance in Medicine* 66.3 (2011), pp. 735–745. DOI: 10.1002/mrm.22861.

[26] Wen Li, Mark Griswold, and Xin Yu. "Rapid T1 mapping of mouse myocardium with saturation recovery look-locker method". In: *Magnetic Resonance in Medicine* 64.5 (2010), pp. 1296–1303. DOI: 10.1002/mrm.22544.

[27] Jeremy Chen, Jianhua Yao, and David Thomasson. "Automatic determination of arterial input function for dynamic contrast enhanced MRI in tumor assessment". In: *Medical Image Computing and Computer-Assisted Intervention* 11.Pt 1 (2008), pp. 594–601. DOI: 10.1007/978-3-540-85988-8_71.

[28] Amita Shukla-Dave et al. "Average arterial input function for quantitative dynamic contrast enhanced magnetic resonance imaging of neck nodal metastases". In: *BMC medical physics* 9 (May 2009), p. 4. DOI: 10.1186/1756-6649-9-4.

[29] Xia Li et al. "A novel AIF tracking method and comparison of DCE-MRI parameters using individual and population-based AIFs in human breast cancer". In: *Physics in Medicine and Biology* 56 (17 Sept. 2011), pp. 5753–5769. DOI: 10.1088/0031-9155/56/17/018.

[30] Edward Ashton, Teresa McShane, and Jeffrey Evelhoch. "Inter-operator variability in perfusion assessment of tumors in MRI using automated AIF detection". In: *Medical Image Computing and Computer-Assisted Intervention* 8.Pt 1 (2005), pp. 451–458. DOI: 10.1007/11566465_56.PMID:16685877.

[31] Jakub Nalepa et al. "Fully-automated deep learning-powered system for DCE-MRI analysis of brain tumors". In: *Artificial Intelligence in Medicine* 102 (2020), p. 101769. ISSN: 0933-3657. DOI: 10.1016/j.artmed.2019.101769.

[32] Thomas Fritz-Hansen et al. "Measurement of the arterial concentration of Gd-DTPA using MRI: a step toward quantitative perfusion imaging". In: *Magnetic resonance in medicine* 36.2 (1996), pp. 225–231. DOI: 10.1002/mrm.1910360209.

[33] MR Technology Information Portal. *Clariscan*. URL: https://www.mr-tip.com/serv1.php?type=db1\&dbs=Clariscan\%26trade\%3B.

[34] Robert L. Greenman et al. "Double inversion black-blood fast spin-echo imaging of the human heart: A comparison between 1.5T and 3.0T". In: *Journal of Magnetic Resonance Imaging* 17.6 (2003), pp. 648–655. DOI: 10.1002/jmri.10316.

[35] Hidenobu Matsuzaki et al. "Diagnostic value of dynamic contrast-enhanced MRI for submucosal palatal tumors". In: *European Journal of Radiology* 81.11 (2012), pp. 3306–3312. DOI: 10.1016/j.ejrad.2012.04.009.

[36] Lawrence I-Kuei Lin. "A concordance correlation coefficient to evaluate reproducibility". In: *International Biometric Society* 45.1 (1989), pp. 255–268. DOI: 10.2307/2532051.

[37] Thomas Koopman et al. "Repeatability of arterial input functions and kinetic parameters in muscle obtained by dynamic contrast enhanced MR imaging of the head and neck". In: *Magnetic Resonance Imaging* 68 (2020), pp. 1–8. DOI: 10.1016/j.mri.2020.01.010.

[38] Jeffrey L. Evelhoch. "Key factors in the acquisition of contrast kinetic data for oncology". In: *Journal of Magnetic Resonance Imaging* 10.3 (1999), pp. 254–259. DOI: 10.1002/(SICI)1522-2586(199909)10:3<254::AID-JMRI5>3.0.CO;2-9.

[39] Chun-Hao Wang et al. "Review of treatment assessment using DCE-MRI in breast cancer radiation therapy". In: *World journal of methodology* 4.2 (2014), pp. 46–58. DOI: 10.5662/wjm.v4.i2.46.

[40] Olga Schimpf, Stefan Hindel, and Lutz Lüdemann. "Assessment of micronecrotic tumor tissue using dynamic contrast-enhanced magnetic resonance imaging". In: *Physica medica: PM : an international journal devoted to the applications of physics to medicine and biology : official journal of the Italian Association of Biomedical Physics (AIFB)* 34 (2017), pp. 38–47. DOI: 10.1016/j.ejmp.2017.01.010.

[41] Kine Mari Bakke et al. "Comparison of Intravoxel incoherent motion imaging and multiecho dynamic contrast-based MRI in rectal cancer". In: *Journal of Magnetic Resonance Imaging* 50.4 (2019), pp. 1114–1124. DOI: 10.1002/jmri.26740.

[42] Jon-Vidar Gaustad et al. "DCE-MRI of Tumor Hypoxia and Hypoxia-Associated Aggressiveness". In: *Cancers* 12.7 (2020), p. 1979. DOI: 10.3390/cancers12071979.

[43] Ilana C. Benjaminsen et al. "Assessment of extravascular extracellular space fraction in human melanoma xenografts by DCE-MRI and kinetic modeling". In: *Magnetic Resonance Imaging* 26.2 (2008), pp. 160–170. DOI: 10.1016/j.mri.2007.06.003.

[44] Kjersti V. Lund et al. "Pharmacokinetic analysis of DCE-MRI data of locally advanced cervical carcinoma with the Brix model". In: *Acta Oncologica* 58.6 (2019), pp. 828–837. DOI: 10.1080/0284186X.2019.1580386.

[45] Stefan Zwick et al. “Simulation-based comparison of two approaches frequently used for dynamic contrast-enhanced MRI”. In: *European Radiology* 2 (2010), pp. 432–442. DOI: 10.1007/s00330-009-1556-6.

[46] Robert V. Bergen, Lawrence Ryner, and Marco Essig. “Comparison of DCE-MRI parametric mapping using MP2RAGE and variable flip angle T1 mapping”. In: *Magnetic Resonance Imaging* (2020). DOI: 10.1016/j.mri.2020.01.001.

[47] Chittaranjan Andrade. “The P Value and Statistical Significance: Misunderstandings, Explanations, Challenges, and Alternatives”. In: *Indian journal of psychological medicine* 41.3 (2019), 210–215. DOI: 10.4103/IJPSYM.IJPSYM_193_19.

[48] S Walker-Samuel, M O Leach, and D J Collins. “Evaluation of response to treatment using DCE-MRI: the relationship between initial area under the gadolinium curve (IAUGC) and quantitative pharmacokinetic analysis”. In: *Physics in Medicine and Biology* 51.14 (2006), pp. 3593–3602. DOI: 10.1088/0031-9155/51/14/021.

[49] Caleb Roberts et al. “Comparative study into the robustness of compartmental modeling and model-free analysis in DCE-MRI studies”. In: *Journal of Magnetic Resonance Imaging* 23.4 (2006), pp. 554–563. DOI: 10.1002/jmri.20529.

[50] Fahmi Khalifa et al. “Models and methods for analyzing DCE-MRI: A review”. In: *Medical Physics* 41.12 (2014), p. 124301. DOI: 10.1118/1.4898202.

[51] Nermin Tuncbilek et al. “Prognostic value DCE-MRI parameters in predicting factor disease free survival and overall survival for breast cancer patients”. In: *European Journal of Radiology* 81.5 (2012), pp. 863–867. DOI: 10.1016/j.ejrad.2011.02.021.

[52] Francis Kar ho Lee et al. “Dynamic contrast enhancement magnetic resonance imaging (DCE-MRI) for differential diagnosis in head and neck cancers”. In: *European Journal of Radiology* 81.4 (2012), pp. 784–788. DOI: 10.1016/j.ejrad.2011.01.089.

[53] Giulio Aniello Santoro. *Rectal Cancer: A Multidisciplinary Approach to Management*. IntechOpen, 2011. DOI: 10.5772/1293.

[54] Yi-hong Ling et al. “Tumor necrosis as a poor prognostic predictor on postoperative survival of patients with solitary small hepatocellular carcinoma”. In: *BMC Cancer* 20.1 (2020), p. 607. DOI: 10.1186/s12885-020-07097-5.

[55] Alan Jackson et al. “Imaging Tumor Vascular Heterogeneity and Angiogenesis using Dynamic Contrast-Enhanced Magnetic Resonance Imaging”. In: *Clin Cancer Res* 13.12 (2007), 3449–3459. DOI: 10.1158/1078-0432.CCR-07-0238.

[56] S. J. Mills et al. “Do Cerebral Blood Volume and Contrast Transfer Coefficient Predict Prognosis in Human Glioma?” In: *American Journal of Neuroradiology* 27.4 (2006), pp. 853–858. ISSN: 0195-6108. URL: http://www.ajnr.org/content/27/4/853.

[57] Amita Shukla-Dave et al. “Dynamic contrast-enhanced magnetic resonance imaging as a predictor of outcome in head-and-neck squamous cell carcinoma patients with nodal metastases”. In: *Int J Radiat Oncol Biol Phys* 82.5 (2012), pp. 1837–1844. DOI: 10.1016/j.ijrobp.2011.03.006.

[58] Rebecca A.P. Dijkhoff et al. “Value of DCE-MRI for staging and response evaluation in rectal cancer: A systematic review”. In: *European Journal of Radiology* 95 (2017), pp. 155–168. DOI: 10.1016/j.ejrad.2017.08.009.

[59] Cathinka Halle et al. “Hypoxia-Induced Gene Expression in Chemoradioresistant Cervical Cancer Revealed by Dynamic Contrast-Enhanced MRI”. In: *Cancer Research* 72.20 (2012), 5285–5295. DOI: 10.1158/0008-5472.CAN-12-1085.

[60] Oliver J. Gurney-Champion et al. “Quantitative imaging for radiotherapy purposes”. In: *Radiotherapy and oncology : journal of the European Society for Therapeutic Radiology and Oncology* 146 (2020), pp. 66–75. DOI: 10.1016/j.radonc.2020.01.026.

[61] James P. B. O’Connor et al. “Imaging biomarker roadmap for cancer studies”. In: *Nature Reviews Clinical Oncology* 3 (2017), pp. 169–186. DOI: 10.1038/nrclinonc.2016.162.

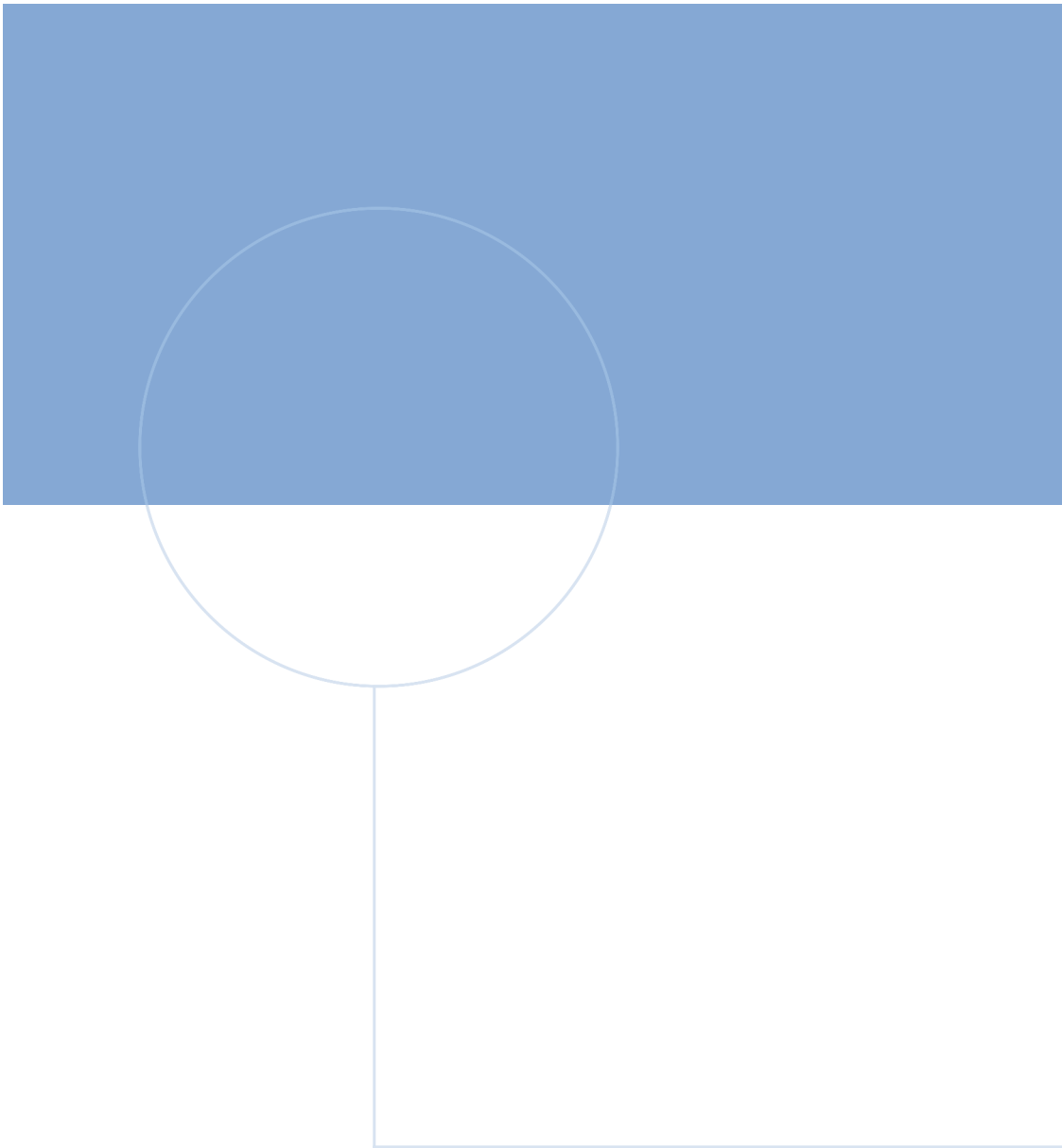

NTNU

Norwegian University of
Science and Technology